ACOUSTIC METAMATERIALS FOR ENHANCED WAVE CONTROL

A Dissertation
Presented to
The Academic Faculty

by

Steven R. Craig

In Partial Fulfillment
of the Requirements for the Degree
Doctor of Philosophy in the
George W. Woodruff School of Engineering
Department of Mechanical Engineering

Georgia Institute of Technology
December 2022

COPYRIGHT © 2022 BY STEVEN CRAIG

ACOUSTIC METAMATERIALS FOR ENHANCED WAVE CONTROL

Approved by:

Dr. Chengzhi Shi, Advisor
School of Mechanical Engineering
Georgia Institute of Technology

Dr. Yuhang Hu
School of Mechanical Engineering
Georgia Institute of Technology

Dr. Karim Sabra
School of Mechanical Engineering
Georgia Institute of Technology

Dr. Roshan Joseph
School of Industrial and Systems Engineering
Georgia Institute of Technology

Dr. Julien Meaud
School of Mechanical Engineering
Georgia Institute of Technology

Dr. Michael Leamy
School of Mechanical Engineering
Georgia Institute of Technology

Date Approved: December 2, 2022

TABLE OF CONTENTS

LIST OF FIGURES **vi**

SUMMARY **xxiv**

CHAPTER 1. Introduction **1**
1.1 Acoustic metamaterials **1**
1.2 Thesis overview **5**

CHAPTER 2. Non-Hermitian complementary acoustic metamaterials **8**
2.1 Introduction **8**
2.2 Idealized fluid simulation **10**
  2.2.1 One-dimensional simulations 13
  2.2.2 Imaging with the NHCMM 15
  2.2.3 High intensity focused ultrasound with the NHCMM 17
2.3 Poroelastic simulations **19**
  2.3.1 Imaging through a poroelastic skull with a NHCMM 21
  2.3.2 Focusing through a poroelastic skull with a NHCMM 23
2.4 Imaging through an imperfect skull **25**
  2.4.1 Imaging through a sloped skull 28
  2.4.2 Imaging through a curved skull 34
  2.4.3 Imaging through a skull with blood vessels 37
  2.4.4 Imaging through a skull with multiple irregularities 40
  2.4.5 Further discussion 41
2.5 Design of the circuit elements **45**

CHAPTER 3. Willis coupling **50**
3.1 Bianisotropic gratings **50**
  3.1.1 Introduction 50
  3.1.2 Asymmetric Transmission 54
  3.1.3 Asymmetric Reflection 56
  3.1.4 Full-wave simulations 59
  3.1.5 Determining the scatterer geometries 62
  3.1.6 Bianisotropic gratings for 35-degree incidence 63
  3.1.7 Bianisotropic gratings for 70-degree incidence 67
3.2 Willis coupling enabling extreme effective material parameters **71**
  3.2.1 Introduction 71
  3.2.2 Modeling 73
  3.2.3 Results 77
  3.2.4 Metamaterial circuit design 86
  3.2.5 Quality factor of the metamaterial 89

CHAPTER 4. Transformation acoustics **91**
4.1 Introduction **91**

4.2 Correcting focused acoustic waves 93
4.3 Correcting self-bending acoustic beams 98
4.4 Focused and self-bending beam derivations 99
  4.4.1 Focused waves 99
  4.4.2 Self-bending beam 101
4.5 High anisotropy, grating dispersion, and full-wave simulations 106
  4.5.1 High anisotropy 106
  4.5.2 Grating dispersion 108
  4.5.3 Full-wave simulations with and without viscothermal loss 110

CHAPTER 5. Conclusions 114
5.1 Non-Hermitian complementary acoustic metamaterials 114
5.2 Willis coupling 116
5.3 Transformation acoustics 117

REFERENCES 118

LIST OF FIGURES

1.1 Acoustic propagation in natural media and metamaterials. For all natural materials, both density and bulk modulus are positive with a positive phase velocity and refractive index. Metamaterials realize negative effective densities or bulk moduli near dipolar or monopolar resonance, respectively. Single negative materials have a purely imaginary phase velocity and a frequency bandgap where acoustic waves cannot propagate. The acoustic wave front propagates in the opposite direction of the energy flow when the density and bulk modulus are simultaneously negative. Complex material properties represent acoustic amplification or attenuation as a function of propagation distance and are represented by the axes directed into and out of the paper. 2

2.1 NHCMM for noninvasive ultrasonic brain imaging. (a) Schematics of the application of NHCMM for ultrasonic brain imaging through an intact skull. (b) Simplified model of acoustic wave propagation through the combined NHCMM and skull layer with an incident wave outside of the top part of the patient's head submerged in water. The acoustic properties of the brain are similar to those of water and are simulated as water. 11

2.2 Acoustic wave propagation through the skull when compensated by (a) and (b) NHCMM and (c) and (d) CMM. The skull thickness is between 0 and 1 cm, and the complementary layer is between 1 and 0 cm for (a) and (c). The skull is between 1 and 0 cm and the complementary layer is in between 0 and 1 cm for (b) and (d). (e) Acoustic wave propagation through the skull layer. For all cases, the red curve represents the acoustic amplitude, and the blue curve represents the acoustic field. 14

2.3 Ultrasonic imaging of a brain tumor. (a) Imaging through the skull complemented by the NHCMM. (b) Direct imaging without the skull. (c) Imaging through the skull complemented by the CMM. (d) Imaging directly through skull. For (a) and (c), the amplitude of the reflected wave in the dashed rectangle (20 mm by 60 mm) with the right boundary 10 mm away from the outer boundary of the bilayer is shown. For (b), the brain tumor is shifted 20 mm to the left compared with the other cases. For (d), the right boundary of the dashed space is 20 mm away from the outer boundary of the skull. The reflected pressure amplitudes along the red line at the middle of the dashed space for all cases are plotted. 16

2.4 Focused ultrasound generated by a curved transducer. (a) Focusing through the skull complemented by the NHCMM. (b) Focusing without the skull. (c) Focusing through the skull complemented by the CMM. (d) Focusing directly through the skull. The pressure amplitude in the square (60 mm by 60 mm) is shown. The left boundary of the square is 20 mm away from the inner boundary of the skull for (a), (c), and (d). The square is shifted 20 mm to the left for (b) compared with the other cases. 18

2.5 Acoustic wave propagation through a porous skull simulated with a poroelastic layer using Biot's model when compensated by (a, b) NHCMM and (c, d) CMM. The skull thickness is between 0 and 1 cm, and the complementary layer is in between -1 to 0 cm for (a) and (c). The skull is in between -1 to 0 cm and the complementary layer is in between 0 to 1 cm for (b) and (d). (e) Acoustic wave propagation through the porous skull layer. For all cases, the red curve represents the acoustic amplitude, and the blue curve represents the acoustic field. 20

2.6 Ultrasonic imaging of a brain tumor through a porous skull simulated with a poroelastic layer using Biot's model. (a) Imaging through the skull complemented by the NHCMM. (b) Imaging through the skull complemented by the CMM. (c) Imaging directly through skull. For (a) and (b), the amplitude of the reflected wave in the dashed rectangle (20 mm by 60 mm) with the right boundary 10 mm away from the outer boundary of the bilayer are shown. For (c), the right boundary of the dashed space is 20 mm away from the outer boundary of the skull. The reflected pressure amplitudes along the red line at the middle of the dashed space for all cases are plotted. 22

2.7 Focused ultrasound generated by a curved transducer. (a) Focusing through the poroelastic skull complemented by the NHCMM. (b) Focusing through the skull complemented by the CMM. (c) Focusing directly through the poroelastic skull. The pressure amplitude in the square (60 mm by 60 mm) are shown. The left boundary of the square is 20 mm away from the inner boundary of the poroelastic skull. 24

2.8 Method to retrieve tumor scattering from the total pressure field. (a) Diagram of tumor-skull-NHCMM with incident pressure (green arrows). (b) Incident and reflected acoustic pressure field of an imaging plane wave incident on a concentric NHCMM-skull bilayer with a skull radius of 100 mm. (c) Incident and reflected acoustic pressure field of the same geometry in (b) but with a brain tumor. (d) The subtraction of the measured pressure fields in (b) and (c). (e) Filtering the results in (d) using a two-dimensional Fourier transform to isolate the backscattering from just the tumor. The color bar represents the normalized pressure amplitude. 27

2.9 Effects of skull sloping on ultrasound imaging with NHCMM. (a) Illustration of the skull sloping model used in full wave simulations. Plane wave incidence from the top of the subfigure. Reflected pressure fields are taken in the black dashed rectangles with the pressure amplitude recorded on the red dashed line. (b) Scattered pressure field from imaging through a skull with an internal slope of 1.67% compensated by a flat metamaterial. (c) Scattered pressure field from imaging through a skull with a larger internal slope of 3.33% compensated by a flat metamaterial. (d) Scattered pressure field from imaging through a skull with a 1.67% slope compensated by a metamaterial with the mirrored skull geometry. (e) Scattered pressure field from imaging through a skull with a 3.33% slope compensated by a metamaterial with the mirrored skull geometry. The color bars represent pressure amplitudes in Pa. 29

2.10 Additional skull sloping cases. (a), (b), and (c) are scattered pressure fields from skull thicknesses increasing by 0.5 mm, 0.75 mm, and 1.5 mm, respectively, with a 10 mm uniform NHCMM. (d), (e), and (f) are corresponding .83% (0.5 mm rise), 1.25% (0.75 mm rise), and 2.5% (1.5 mm rise) sloped cases with tuned NHCMM layers to match the skull thickness. The color bars represent pressure amplitudes in Pa. 32

2.11 Multi-slope condition. (a) Diagram of the skull/NHCMM condition with the skull slope changing by ± 6.67%, peaking in thickness at the center of the imaging region, coupled with a uniform 10 mm thick NHCMM. (b) Scattered pressure field from the multi-slope skull coupled with a 10 mm thick NHCMM. (c) Scattered pressure field from the multi-slope skull with a NHCMM layer that matches the changes in thickness of the skull. The color bars represent pressure amplitude in Pa. 34

2.12 Effects of skull curvature on ultrasound imaging with NHCMM. (a) Illustration of the curved NHCMM-skull setup with a plane wave incident from the top of the subfigure. Reflected pressure fields are taken in the black dashed rectangles with the pressure amplitude recorded on the red dashed line. (b) Backscattered pressure field and pressure amplitude from a tumor without either NHCMM or skull layers. (c) Backscattered pressure field amplitude resulted from imaging through a flat NHCMM-skull bilayer. (d) Filtered pressure field amplitude resulted from imaging through a curved, concentric NHCMM-skull bilayer with an outer skull radius of 100 mm. (e) Filtered pressure field amplitude resulted from imaging through a curved, concentric NHCMM-skull bilayer with an outer skull radius of 50 mm. (f) Filtered pressure field amplitude resulted from imaging through a curved NHCMM-skull bilayer modeled by shifted circular arcs having radii of 100 mm. (g) Filtered pressure field amplitude resulted from imaging through a curved NHCMM-skull bilayer modeled by shifted circular arcs having radii of 50 mm. The color bars represent pressure amplitudes in Pa. 36

2.13 Effects of blood vessel induced indentation on ultrasound imaging with NHCMM. (a) Illustration of the NHCMM-skull bilayer with a blood vessel imprinting on the interior side of the skull. Reflected pressure fields are taken in the black dashed rectangles with the pressure amplitude recorded on the red dashed line. (b) Scattered pressure field from imaging through a skull having a small blood vessel vertically aligned with the tumor and compensated by NHCMM. (c) Scattered pressure field from imaging through a skull having a larger blood vessel vertically aligned with the tumor and compensated by NHCMM. (d) Scattered pressure field from imaging through a skull having a small blood shifted 10 mm to the right from its location in (b) compensated by NHCMM. (e) Scattered pressure field from imaging through a skull having a medium blood vessel shifted 10 mm to the right from its location in (c) compensated by NHCMM. (f) Scattered pressure field from imaging through a skull having a small blood vessel shifted 20 mm to the right from its location in (b) compensated by NHCMM. (g) Scattered pressure field from imaging through a skull having a medium blood vessel shifted 20 mm to the right from its location in (c) compensated by NHCMM. The color bars represent pressure amplitude in Pa. 39

2.14 Effects of multiple skull inhomogeneities on ultrasound imaging with NHCMM. (a) Diagram of the skull, NHCMM, blood vessel, and tumor arrangement. The skull was modeled to be curved and increased in thickness towards the right end of the imaging window. The tumor in the diagram is the shape of the pear-shaped irregular tumor. A large blood vessel is located above the tumor which creates a hemispherical indent in the skull. (b) The scattered pressure field of the inhomogeneous skull with a uniform tumor and precisely tuned NHCMM. (c) The scattered pressure field of the inhomogeneous skull and irregular tumor with a precisely tuned NHCMM to match the skull geometry. The color bars represent pressure amplitudes in Pa. 41

2.15 Schematic of the NHCMM with a tunable feedback loop circuit (a) Phase shifting circuit for high frequency signals employing a LM7171 operational amplifier. The phase is tuned by modulating R2and C1 to achieve a desired phase from 0 to -180 degrees. (b) Active gain circuit using a Non-Inverting Op-amp to change the gain by changing the resistance values of R3 and R4. (c) Phase shifting circuit for high frequency signals employing a LM7171 operational amplifier. The phase is tuned by modulating R5 and C2 to achieve a desired phase. (d) One-dimensional waveguide employing water as the background medium to send incident signals and record the resulting reflection and transmission coefficients as a potential experimental set up. 47

2.16 Retrieved material parameters that enable ultrasound transmission through the skull (a) Plot of the real effective density values normalized by the desired real density over a frequency range of 1-2MHz. (b) Plotting the imaginary effective density values normalized by the desired imaginary density over a frequency range of 1-2MHz. (c) Plot of the real effective bulk modulus normalized by the desired real bulk modulus over a frequency range of 1-2MHz. (d) Plot of the imaginary effective bulk modulus normalized by the desired imaginary bulk modulus over a frequency range of 1-2MHz. 48

3.1 The polarizability tensor and its desired scattering outcome (a) The elements of the polarizability tensor of a bianisotropic particle that allows both forward and backward scattering as functions of frequency. (b) Asymmetric wave scattering for different incidences from the bianisotropic particle in (a). (c) The elements of the polarizability tensor of a bianisotropic particle with only backward scattering. (d) Asymmetric wave scattering for different incidences from the bianisotropic particle in (c). For both (b) and (d), the blue arrows represent incident and red arrows represent scattered waves, respectively. 53

3.2 Wavevector analysis for the transmission wave-grating interaction with experiment results (a) Wave-grating interaction for the transmission case for -45-degree incidence in the reciprocal space. (b) Wave-grating interaction for +45-degree incidence as well as the time reversed case represented by the dashed lines. For both (a) and (b), the incident, scattered, and Bloch wavevectors are represented by $\vec{k}_i$, $\vec{k}_s$ and Δk, respectively. (c) Bianisotropic grating structure with asymmetric wave scattering in (a) and (b) determined by inverse Fourier analysis of the Bloch wavevectors. (d) Two-dimensional spatial Fourier transform of the grating geometry with the expected scattering wavevectors having the highest intensity. (e) Experimental set up for the bianisotropic transmission grating. The zoom out shows the detailed structure of the grating. The outlined rectangles with red dashed lines represent the scanned areas. (f) Measured pressure field of acoustic waves propagating with positive k_x component for -45-degree incidence. (g) Measured pressure field with negative k_x component for -45-degree. (h) Measured pressure field of acoustic waves propagating with positive k_x component for +45-degree incidence. (i) Measured pressure field with negative k_x component for +45-degree incidence. All the pressure fields in (f), (g), (h), and (i) are normalized by their corresponding maximum amplitude in each measurement. 55

3.3 Wavevector analysis for the reflection wave-grating interaction with experiment results (a) Wave-grating interaction for the reflection case for 45-degree incidence in the reciprocal space. (b) Wave-grating interaction for normal incidence as well as the time reversed case represented by the dashed lines. For both (a) and (b), the incident, scattered, and Bloch wavevectors are represented by $\vec{k}_i$, $\vec{k}_s$ and Δk, respectively. (c) Bianisotropic grating structure with asymmetric wave scattering in (a) and (b) determined by inverse Fourier analysis of the Bloch wavevectors. (d) Two-dimensional spatial Fourier transform of the grating geometry with the expected scattering wavevectors having the highest intensity to the left of the inversion symmetry about the y-axis (e) Experimental set up for the bianisotropic reflection grating. The zoomed in image shows the detailed structure of the grating. The outlined rectangle with red dashed lines represents the scanned areas. (f) Measured pressure field of acoustic waves propagating with a positive k_x component for normal incidence. (g) Measured pressure field with negative k_x component for normal incidence. (h) Measured pressure field of acoustic waves propagating with positive k_x component for +45-degree incidence. (i) Measured pressure field with negative k_x component for +45-degree incidence. (j) Measured pressure field of acoustic waves propagating with positive k_x component for -45-degree incidence. (k) Measured pressure field with negative k_x component for -45-degree incidence. All the pressure fields in (f), (g), (h), (i), (j), and (k) are normalized by their corresponding maximum amplitude in each measurement. 58

3.4 Fourier analysis of the wave-grating interaction for the 45-degree transmission experiment and full-wave simulation results (a) Measured pressure field for the transmission grating having -45-degree incidence and reflection directed back towards the source. (b) Two-dimensional Fourier transform of (a) with the expected wavevectors having the highest intensities. (c) Simulated pressure field for -45-degree incidence case. (d) Two-dimensional Fourier transform of (c) with wavevectors having peak intensities matching (b). (e) Measured pressure field for 45-degree incidence and -45-degree transmission. (f) Fourier transform of the measured pressure field in (e) illustrating expected wavevector locations in reciprocal space. (g) Simulated pressure field for 45-degree incidence. (h) Two-dimensional Fourier transform of (g) with wavevectors having peak intensities matching (f). 60

3.5 Fourier analysis of the wave-grating interaction for the 45-degree reflection experiment and full-wave simulation results (a) Measured pressure field for the reflection grating having a -45-degree incidence and normal reflection. (b) Two-dimensional Fourier transform of (a) with the expected wavevectors having the highest intensity values. (c) Simulated pressure field for -45-degree incidence. (d) Two-dimensional Fourier transform of (c) with wavevectors having peak intensities matching (b). (e) Measured pressure field for 45-degree incidence with reflection directed back towards the source. (f) Fourier transform of the measured pressure field in (e) having peak intensities matching the expected wavevectors. (g) Simulated pressure field for 45-degree incidence. (h) Two-dimensional Fourier transform of (g) with wavevectors having peak intensities matching (f). (i) Measured pressure field for normal incidence with a 135-degree reflection. (j) Two-dimensional Fourier transform of (i) having peak intensities at expected wavevector locations. (k) Simulation of normal incidence case. (l) Two-dimensional Fourier transform of (k) having wavevectors matching (j). 61

3.6 Wavevector analysis for the 35-degree transmission grating and full-wave simulation results (a) Wave-grating interaction for the transmission grating having -35-degree incidence and 145-degree reflection in reciprocal space, allowing for the determination of the required grating Bloch wavevector. (b) Wave-grating interaction for 35-degree incidence as well as the time reversed case represented by the dashed lines. For both (a) and (b), the incident, scattered, and Bloch wavevectors are represented by $\vec{k}_i$, $\vec{k}_s$ and Δk, respectively. (c) Bianisotropic grating structure with asymmetric wave scattering in (a) and (b) determined by inverse Fourier analysis of the incident and scattered wavevectors. (d) Real component of the two-dimensional spatial Fourier transform of the grating geometry with the expected Bloch wavevectors having the highest intensity. (e) Imaginary component of the two-dimensional spatial Fourier transform of the grating geometry having a zero vector. (f) Simulated pressure field of a -35-degree incident signal interacting with the bianisotropic transmission grating. (g) Two-dimensional Fourier transform of (f) with wavevectors having peak intensities matching the desired scattering in (a). (h) Simulated pressure field of a 35-degree incident signal interacting with the bianisotropic transmission grating. (i) Two-dimensional Fourier transform of (h) with wavevectors having peak intensities matching the desired scattering in (b). 64

3.7 Wavevector analysis for the 35-degree reflection grating and full-wave simulation results (a) Wave-grating interaction for the reflection case for 35-degree incidence in reciprocal space and corresponding grating Bloch wavevector. (b) Wave-grating interaction for normal incidence as well as the time reversed case represented by the dashed lines. For both (a) and (b), the incident, scattered, and Bloch wavevectors are represented by $\vec{k}_i$, $\vec{k}_s$ and Δk, respectively. (c) Bianisotropic grating structure with asymmetric wave scattering in (a) and (b) determined by a finite element program to maximize the grating efficiency. (d) Real component of a two-dimensional spatial Fourier transform of the grating geometry with the expected scattering wavevectors having the highest intensity to the left of the inversion symmetry about the y-axis (e) Imaginary component of the two-dimensional spatial Fourier transform of the grating geometry having a zero vector. (f) Simulated pressure field of a 35-degree incident signal interacting with the bianisotropic reflection grating (g) Two-dimensional Fourier transform of (f) with wavevectors having peak intensities matching the desired scattering in (a). (h) Simulated pressure field of a normally incident signal interacting with the bianisotropic transmission grating. (i) Two-dimensional Fourier transform of (h) with wavevectors having peak intensities matching the desired scattering in (b). (j) Pressure field of a -35-degree incident signal and normal reflection after interacting with the grating. (k) Two-dimensional Fourier transform of (j) with wavevectors having peak intensities matching the desired scattering in the time reversal incidence in (b). 66

3.8 Wavevector analysis for the 70-degree transmission grating and full-wave simulation results (a) Wave-grating interaction for the reflection case for -70-degree incidence in reciprocal space and corresponding grating Bloch wavevector. (b) Wave-grating interaction for 70-degree incidence as well as the time reversed case represented by the dashed lines. For both (a) and (b), the incident, scattered, and Bloch wavevectors are represented by $\vec{k}_i$, $\vec{k}_s$ and Δk, respectively. (c) Bianisotropic grating structure with asymmetric wave scattering in (a) and (b) determined by inverse Fourier analysis of the incident and scattered wavevectors. (d) Two-dimensional spatial Fourier transform of the grating geometry with the expected Bloch wavevectors having the highest intensity. (e) Imaginary component of the two-dimensional spatial Fourier transform of the grating geometry having a zero vector. (f) Simulated pressure field of a -70-degree incident signal interacting with the bianisotropic transmission grating (g) Two-dimensional Fourier transform of (f) with wavevectors having peak intensities matching the desired scattering in (a). (h) Simulated pressure field of a 70-degree incident signal interacting with the bianisotropic transmission grating. (i) Two-dimensional Fourier transform of (h) with wavevectors having peak intensities matching the desired scattering in (b). 68

3.9 Wavevector analysis for the 70-degree reflection grating and full-wave simulation results (a) Wave-grating interaction for the reflection case with 70-degree incidence in reciprocal space and corresponding grating Bloch wavevector. (b) Wave-grating interaction for normal incidence as well as the time reversed case represented by the dashed lines. For both (a) and (b), the incident, scattered, and Bloch wavevectors are represented by $\vec{k}_i$, $\vec{k}_s$ and Δk, respectively. (c) Bianisotropic grating structure with asymmetric wave scattering in (a) and (b) determined by a finite element program to maximize the grating efficiency. (d) Real component of a two-dimensional spatial Fourier transform of the grating geometry with the expected scattering wavevectors having the highest intensity to the left of the inversion symmetry about the y-axis (e) Imaginary component of the two-dimensional spatial Fourier transform of the grating geometry having a zero vector. (f) Simulated pressure field of a 70-degree incident signal interacting with the bianisotropic reflection grating (g) Two-dimensional Fourier transform of (f) with wavevectors having peak intensities matching the desired scattering in (a). (h) Simulated pressure field of a normally incident signal interacting with the bianisotropic transmission grating. (i) Two-dimensional Fourier transform of (h) with wavevectors having peak intensities matching the desired scattering in (b). (j) Pressure field of a -70-degree incident signal and normal reflection after interacting with the grating. (k) Two-dimensional Fourier transform of (j) with wavevectors having peak intensities matching the desired scattering in the time reversal incidence in (b). 69

3.10 Imaginary Fourier component of the 45-degree bianisotropic grating (a) Imaginary component of a two-dimensional spatial Fourier transform of the transmission grating geometries indicating no interaction with incident signal. (b) Imaginary component of a two-dimensional spatial Fourier transform of the reflection grating geometries. 71

3.11 Designed unit cell with active feedback control with Willis coupling when $G_1 \neq G_2$. (a) One-dimensional representation of the metamaterial confined in a waveguide with the active sensor-transducer pairs connected to the feedback control circuits (b) Active circuitry comprising each gain function for independent control of the phase and amplitude of G_1 and G_2. (1, 2) in the subscripts of the circuit components denote the resistance or capacitance values for G_1 and G_2, respectively. 74

3.12 Effects of Willis coupling on effective material parameters. (a) The arithmetic mean of the imaginary part of the asymmetry coefficient as a function of the amplitude and phase of G_2 near 2.50 kHz. The three marked points correspond to (b), (c), and (d), respectively. (b) The complex effective density and bulk modulus normalized to air without Willis coupling when $G_1 = G_2 = 2e^{i(0.87)}$. (c) The complex effective density and bulk modulus normalized to air with Willis coupling when $G_1 = 2e^{i(0.87)}$ and $G_2 = 0.6e^{i(2.79)}$. (d) The complex effective density and bulk modulus normalized to air with Willis coupling when $G_1 = 2e^{i(0.87)}$ and $G_2 = 0.15e^{i(4.10)}$. In (b) and (c), the blue diamond and blue square lines plot the real and imaginary bulk modulus, respectively and the red x and red star lines plot the real and imaginary density, respectively. The subplots in (c) and (d) display the corresponding asymmetry coefficient of the Willis coupled metamaterial from 2.00-3.00 kHz. 78

3.13 Full effective parameter map of the complex density and bulk modulus for the active Willis coupled and non-Willis metamaterials. (a) Parameter map of the real part of the effective density and bulk modulus for the active metamaterial with and without Willis coupling. The real part of the effective density and bulk modulus are plotted on the horizontal and vertical axes, respectively. Additionally, the colored points and black points represent effective material parameters for Willis and non-Willis metamaterials, respectively. The color map quantifies the logarithm of the ratio of the imaginary part to the real part of the asymmetry coefficient, $\eta = \log_{10}(Abs(Im\{W\}/\, Re\{W\}))$. (b) Magnified window of (a) displaying a normalized density range of [-1000, 1000] and a normalized bulk modulus range of [-500, 500]. (c) Parameter map of the imaginary part of the effective density and bulk modulus for the active metamaterial with and without Willis coupling. The imaginary part of the effective density and bulk modulus are plotted on the horizontal and vertical axes, respectively. This subfigure has the same color scheme as (a). (d) Magnified window of (c) displaying a normalized density range of [-1000, 1000] and a normalized bulk modulus range of [-500, 500]. 80

3.14 Full parameter map of the complex effective refractive index and acoustic impedance normalized to air for the active Willis coupled and non-Willis metamaterials. (a) The real part of the effective refractive index and acoustic impedance for the active metamaterial with and without Willis coupling. The real part of the effective refractive index and acoustic impedance are plotted on the horizontal and vertical axes, respectively. Additionally, the colored points and black points represent effective material parameters for Willis and non-Willis metamaterials, respectively. The color map quantifies the logarithm of the ratio of the imaginary part to the real part of the asymmetry coefficient, $\eta = \log_{10}(Abs(Im\{W\}/ Re\{W\}))$. (b) Magnified window of (a) displaying an acoustic impedance range of [-100, 100] (c) The imaginary part of the effective refractive index and acoustic impedance for the active metamaterial with and without Willis coupling. The imaginary part of the effective refractive index and acoustic impedance are plotted on the horizontal and vertical axes, respectively. This subfigure has the same color scheme as (a). (d) Magnified window of (c) displaying an acoustic impedance range of [-100, 100]. 84

3.15 Effective material parameter plots for a non-Willis and Willis unit cell (a) Effective parameter map of the real part of the density and bulk modulus for the active metamaterial with Willis coupling. The real part of the effective density and bulk modulus are plotted on the horizontal and vertical axes, respectively. The color map quantifies the quality factor based on the conventional definition for acoustic resonators. (b) Effective parameter map of the real part of the density and bulk modulus for the active metamaterial without Willis coupling. The axes and color map in this subfigure are identical to (a). (c) Parameter map of the imaginary part of the effective density and bulk modulus for the active metamaterial with Willis coupling. The imaginary part of the effective density and bulk modulus are plotted on the horizontal and vertical axes, respectively. This subfigure has the same color scheme as (a). (d) Effective parameter map of the imaginary part of the density and bulk modulus for the active metamaterial without Willis coupling. The axes and color map in this subfigure are identical to (c). 90

4.1 Anisotropic distortion of beamformed acoustic waves with the experiment setup. (a) Discretized transducer array with a phase gradient as a function of the x axis such that the desired acoustic focusing is achieved in an isotropic medium. (b) Identical transducer array with the same phase gradient in an anisotropic medium resulting in a focal point shifted from the desired location. (c) Same transducer array with a corrected phase gradient that restores the focal point to its original location. (d) Experimental setup in which two-dimensional SSAWs propagate across effective isotropic and anisotropic gratings. (e) Close up of the isotropic grating design. (f) Close up of the anisotropic grating design. 92

4.2 Simulation and experiment results for arbitrarily focused acoustic beams. (a) Simulation results of a focused acoustic beam in a two-dimensional isotropic medium that focuses 70 mm to the right and 150 mm above the center of the speaker array. (b) Simulation results of a focused acoustic beam in an effective two-dimensional anisotropic medium with the same phase profile as (a). Here, the resulted focal point shifts from the desired location. (c) Simulation results of a focused acoustic beam in an effective two-dimensional anisotropic medium with a corrected phase profile with a focal point matching (a). (d) Experimental replication of the simulation in (a) with a matching focal point. (e) Experimental replication of the simulation in (b) with a matching focal point. (f) Experimental replication of the simulation in (c) with a matching focal point. 95

4.3 Simulation and experiment results for arbitrarily focused beams with a tilted source. (a) Simulation results of a focused acoustic beam in a two-dimensional isotropic medium that achieves the desired focal point with a ten-degree tilt. (b) Simulation results of a focused acoustic beam with the same phase profile in an effective two-dimensional anisotropic medium. Here, the focal point shifts from the focal point of the isotropic case. (c) Simulation results of a focused acoustic beam in an effective two-dimensional anisotropic medium with a corrected phase profile resulting in focusing at the desired focal point (d) Experimental replication of (a) with a matching focal point. (e) Experimental replication of (b) with a matching focal point. (f) Experimental replication of (c) with a matching focal point. 96

4.4 Simulation and experiment results for self-bending acoustic beams. (a) Simulation results of a self-bending acoustic beam in a two-dimensional isotropic medium that matches the desired beam pattern. (b) Simulation results of a self-bending acoustic beam in an effective two-dimensional anisotropic medium with the same phase profile. Here, the intensity profile shifts from the desired interference pattern. (c) Simulation results of a self-bending acoustic beam in an effective two-dimensional anisotropic medium with a corrected phase profile. Here, the resulted curved interference pattern matches the desired intensity profile in the isotropic case. (d) Experimental replication of the simulation in (a) with a matching curved interference pattern. (e) Experimental replication of (b) with a matching interference pattern. (f) Experimental replication of (c) with a matching interference pattern. 99

4.5 Derivation of the self-bending beam correction technique. (a) Geometric interpretation of a transducer array outputting a convex, curved acoustic beam represented by the red semicircle. The acoustic ray paths, represented by blue lines, are outputs from the transducer array along the x axis forming the desired curve with some determined phase gradient along the x axis. (b) Close up of the general relationship that defines the direction of an acoustic ray outputting from a transducer to its phase change along the x axis. (c) Transducers with transformed coordinate locations and the same phase output produce acoustic ray trajectories at different angles when compared to their untransformed counterparts. 102

4.6 Correcting self-bending beams that propagate in highly anisotropic media. (a) Simulation results of a self-bending acoustic beam in a two-dimensional isotropic medium that matches the desired beam pattern. (b) Simulation results of a self-bending acoustic beam in a medium with an effective density two times greater in the x axis than the y axis. Here, we use the same phase profile as the previous isotropic case with a beam path shifted drastically from the desired interference pattern. (c) Simulation results of a self-bending acoustic beam in an effective two-dimensional anisotropic medium with a corrected phase profile. Here, the beam interference pattern matches the desired curve in the isotropic case. (d) Simulation results of a self-bending acoustic beam in a two-dimensional isotropic medium that follows the desired beam path. (e) Simulation results of a self-bending acoustic beam in a medium with an effective density four times greater in the x axis than the y axis. Here, we use the same phase profile as the previous isotropic case with a beam path shifted drastically from the desired interference pattern. (f) Simulation results of a self-bending acoustic beam in an effective two-dimensional anisotropic medium with a corrected phase profile. Here, the beam interference pattern matches the desired curve in the isotropic case. 107

4.7 Selected grating dispersion with experimental validation. (a) Dispersion curves of SSAWs propagating across grating structures with a 4 mm fin height (blue) and 6.2 mm fin height (red) compared to the dispersion relation of air at audible frequencies (black). (b) Measured pressure field of an acoustic point source positioned directly on top of an effective two-dimensional anisotropic surface. 109

4.8 Simulations that consider viscothermal loss. (a) Full-wave simulation considering viscothermal loss results of a focused acoustic beam in a two-dimensional isotropic medium that focuses 100 mm to the right of the center of the transducer array. (b) Full-wave simulation of a of a focused acoustic beam across a lossless two-dimensional isotropic grating focusing 100 mm to the right of the center of the transducer array. 110

4.9 Simulation of an arbitrarily focused acoustic beam. (a) Full-wave simulation results of a focused acoustic beam in a two-dimensional isotropic medium that focuses 70 mm to the right and 150 mm above the center of the transducer array. (b) Full-wave simulation results of a focused acoustic beam in an effective two-dimensional anisotropic medium with the same phase profile as (a). Here, the resulted focal point shifts from the desired location due to the anisotropic effects of the medium. (c) Full-wave simulation results of a focused acoustic beam in an effective two-dimensional anisotropic medium with a corrected phase profile. Here, the focal point matches the desired focal point in (a). 111

4.10 Simulation of an arbitrarily focused acoustic beam with a tilted source. (a) Full-wave simulation results of a focused acoustic beam in a two-dimensional isotropic medium that achieves the desired focal point with a ten-degree tilt. (b) Full-wave simulation results of a focused acoustic beam in an effective two-dimensional anisotropic medium with the same phase profile and tilt as the previous isotropic case. Here, the focal point of the phase profile shifts from the desired location that the isotropic case achieves. (c) Full-wave simulation results of a focused acoustic beam in an effective two-dimensional anisotropic medium with a corrected phase profile. Here, the focal point matches the desired focal point in the isotropic case. 112

4.11 Simulation of a self-bending acoustic beam. (a) Full-wave simulation results of a self-bending acoustic beam in a two-dimensional isotropic medium that matches the desired beam pattern. (b) Full-wave simulation results of a self-bending acoustic beam in an effective two-dimensional anisotropic medium with the same phase profile as the previous isotropic case. Here, the interference pattern resulted from the phase profile shifts from the desired curve. (c) Simulation results of a self-bending acoustic beam in an effective two-dimensional anisotropic medium with a corrected phase profile. Here, the beam interference pattern matches the desired curve in the isotropic case. 113

SUMMARY

Acoustic metamaterials have redefined the limits of acoustic wave control with composite structures that realize effective material properties that go beyond those of natural materials. These extraordinary material properties enable imaging beyond the diffraction limit, negative effective sound speeds, and acoustic cloaking. Metamaterials continue to be a hot topic in the scientific community, as these resonant structures push the boundaries of acoustic wave control with unprecedented functionality. The primary goal of this work is to advance the prevalence, practicality, and scope of acoustic metamaterial research with novel materials that uniquely tailor wave fields for a variety of acoustic-based applications. Each chapter uses foundational metamaterial physics to advance our understanding of acoustic wave control with composite structures. The first section develops the theory and performs simulations for a non-Hermitian complementary metamaterial (NHCMM) with tunable active feedback loop circuits that improve the acoustic transmission through an intact human skull. This lays the foundation for ultrasonic brain imaging and neural therapies that require high frequency acoustic waves to penetrate deep within the brain. With a similarly designed metamaterial, we compare the accessible range of the effective density and bulk modulus for unit cells with symmetric and asymmetric feedback loop circuits. The asymmetric circuits result in a Willis coupled response that dramatically broadens the metamaterial's attainable parameter range. We also demonstrate asymmetric wave transmission at high efficiency with passive Willis coupled metagratings for acoustic beam steering at extreme angles. Lastly, we use transformation acoustics to correct focused and self-bending acoustic beams that become distorted in anisotropic media. These

developments advance acoustic-based technologies for biomedical imaging, noise control, underwater communication, and structural acoustic applications.

CHAPTER 1

INTRODUCTION

1.1 Acoustic metamaterials

Acoustic metamaterials exploit the resonant responses of man-made structures to achieve extraordinary effective densities and bulk moduli that go beyond those of natural materials [1-3]. These effective material properties govern wave propagation in fluid and solid media, motivating researchers to design composite structures that directly manipulate these parameters. Figure 1.1 illustrates the achievable effective parameter space for natural materials and metamaterials with the bulk modulus (κ) on the vertical axis and the density (ρ) on the horizontal axis. For natural media, the effective density and bulk modulus are strictly positive (first quadrant of Fig. 1.1). Metamaterials realize negative effective properties when an acoustic wave excites the structure at a frequency near its monopolar or dipolar resonance [1-3]. The first experimental realization of an acoustic metamaterial occurred in 2000, where a spherical unit cell comprised of a compressible silicon exterior and a dense lead interior demonstrated a negative effective density when excited by an acoustic wave near its dipolar resonance [4]. The phenomenon of negative effective density arises when the soft, compressible exterior adds a phase delay to the force acting on an interior mass. Near the dipolar resonance of the metamaterial, this phase delay causes the acceleration of the interior mass to be completely out of phase with the exterior force. Since this interior mass dominates the total response of the unit cell, Newton's second law implies that the metamaterial has a negative effective dynamic mass when the force and acceleration are in opposite directions. A diagram illustrates this phenomenon in the second

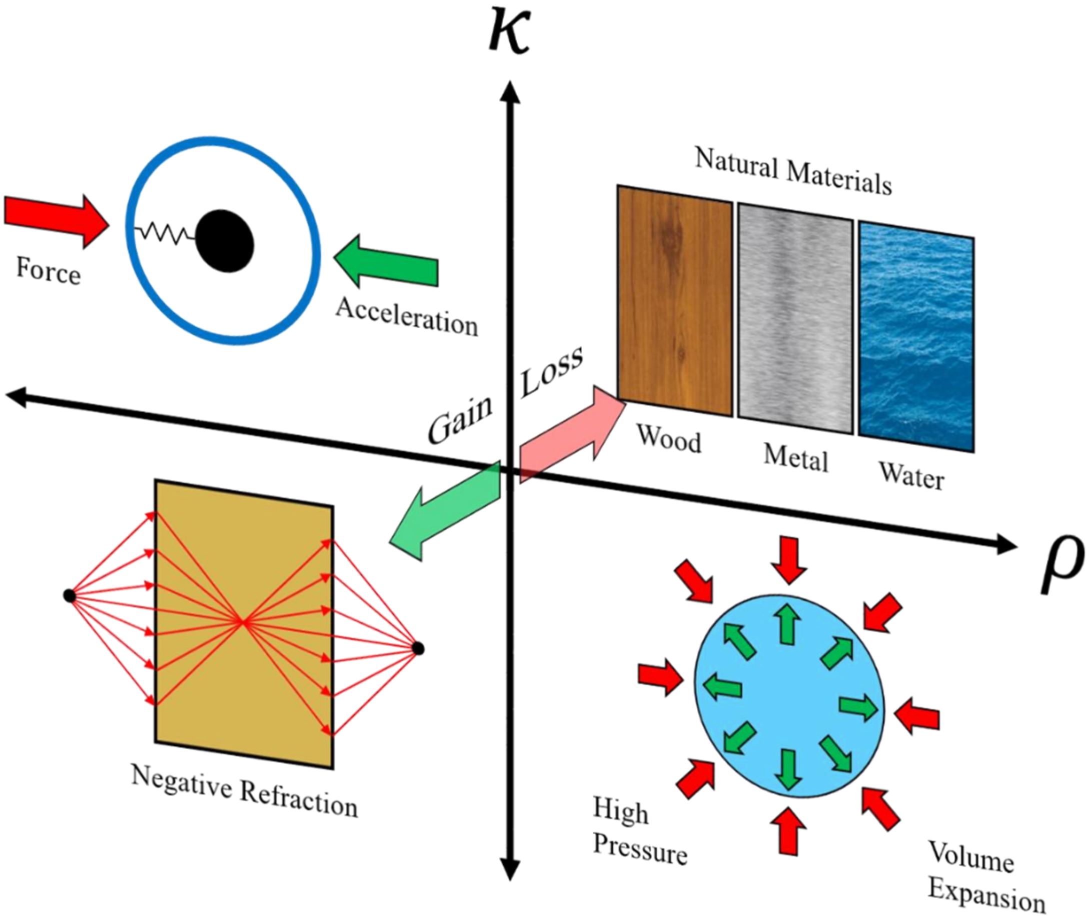

Figure 1.1: Acoustic propagation in natural media and metamaterials. For all natural materials, both density and bulk modulus are positive with a positive phase velocity and refractive index. Metamaterials realize negative effective densities or bulk moduli near dipolar or monopolar resonance, respectively. Single negative materials have a purely imaginary phase velocity and a frequency bandgap where acoustic waves cannot propagate. The acoustic wave front propagates in the opposite direction of the energy flow when the density and bulk modulus are simultaneously negative. Complex material properties represent acoustic amplification or attenuation as a function of propagation distance and are represented by the axes directed into and out of the paper.

quadrant of Figure 1.1. Using a similar working principle, a metamaterial comprised of an array of Helmholtz resonators realized a negative effective bulk modulus when excited by an acoustic wave at a frequency near its monopolar resonance [5]. The resonators were aligned in series within a square aluminum tube serving as an acoustic waveguide. Here, the acoustic pressure and volume contraction were out of phase, which is illustrated in the fourth quadrant of Figure 1.1. The introduction of acoustic metamaterials demonstrated a unique versatility not present in natural materials, as metamaterials were structures with similar resonance characteristics. By tuning the physical dimensions of these composites, the effective material properties of these media are precisely controlled at a given frequency.

The acoustic phase velocity is calculated by the square root of the bulk modulus divided by the density. Given this relation, it was questioned whether having a negative effective bulk modulus or a negative effective density would alter the acoustic phase velocity. Mathematically, a negative bulk modulus or a negative density results in a purely imaginary phase velocity. The imaginary part of the sound speed manifests as a wave that decays exponentially as a function of propagation distance. In other words, metamaterials with a negative effective density or a negative effective bulk modulus exhibit a frequency band gap that prevents acoustic wave propagation. However, questions surrounding the feasibility of metamaterials with negative phase velocity remained. To achieve this goal, we refer to the formulation of the phase velocity, $\mathrm{c}^2 = \kappa\rho^{-1}$, where κ is the bulk modulus, ρ^{-1} is the inverse of the mass density, and c is the phase speed of the medium. Without loss of generality, we express the bulk modulus and inverse density as complex variables $\kappa = \kappa_0 \mathrm{e}^{\mathrm{i}\theta_\kappa}$ and $\rho^{-1} = \rho_0^{-1}\mathrm{e}^{i\theta_{\rho^{-1}}}$ with κ_0, ρ_0^{-1}, θ_κ, and $\theta_{\rho^{-1}}$ being the magnitude and phase of the corresponding quantities, respectively. When $\kappa < 0$ and $\rho < 0$ we have $\theta_\kappa = \pi$, and $\theta_{\rho^{-1}} = \pi$, yielding,

$$\mathrm{c}^2 = \kappa\rho^{-1} = \kappa_0\rho_0^{-1}\mathrm{e}^{i2\pi} \tag{1.1}$$

$$\mathrm{c} = \mathrm{c}_0\mathrm{e}^{\mathrm{i}\pi} = \sqrt{\kappa_0\rho_0^{-1}}e^{i\pi} \tag{1.2}$$

By superimposing unit cells with negative effective densities or bulk moduli into a single structure with overlapping monopolar and dipolar resonances, “double negative” metamaterials with simultaneously negative effective densities and bulk moduli are realized [6]. These combined properties result in a negative phase velocity and a negative refractive index (third quadrant of Fig. 1.1). Double negative metamaterials with a negative refractive index enable imaging beyond the diffraction limit with superlenses [7,8] and hyperlenses [9]. In 2010, soft silicon microbeads suspended in a water-based gel realized a simultaneous negative effective density and bulk modulus to demonstrate a negative phase velocity and refractive index [10]. Microscopic pores in the silicon microbeads allowed for highly compressible unit cells with strong monopolar and dipolar resonant responses. For this structure, the phase velocity becomes negative as derived in Equation 1.2. This implies that the phase of the wave front travels in the opposite direction of the energy propagation.

Although metamaterials realize these exotic effective material properties with passive structures, their reliance on resonance produces undesired lossy behavior, narrow bandwidth, and a lack of tunability. Active metamaterials compensate for these disadvantages by modulating the additional energy inputs with electrical circuits [11,12]. These circuits are highly tunable and can be adjusted in real time because of the swift processing speeds in electrical circuits compared to acoustic wave speeds, allowing the development of active metasurfaces for reconfigurable focusing and beam steering [13]. The tunability of active metamaterials was used to modulate the effective density through simple alterations of their active circuitry [14]. Elastic metamaterials with active piezoelectric elements enable the control of different wave characteristics without changing material or structural parameters for transformation-based cloaking [15], elastic black holes [16], and topological immunity on elastic surfaces [17]. Additionally, active metamaterials can achieve negative effective material parameters by manipulating the monopole and dipole resonant responses of the unit cells [18,19]. Active metamaterials also introduce complex-valued material properties that characterize wave amplification or attenuation as a function of propagation distance. The imaginary parts of the effective density, bulk modulus, and phase speed quantify this energy gain or loss and represent an additional dimension in the effective parameter space shown in Figure 1.1. These foundational works establish the core principles of acoustic metamaterial physics. Scientists and engineers now aim to develop metamaterial-based applications that improve acoustic and phononic control with these sophisticated materials.

1.2 Thesis overview

An organization of this thesis is as follows: Chapter 2 develops the theory and conducts finite element simulations for a non-Hermitian complementary metamaterial (NHCMM) that enhances acoustic transmission through a skull for biomedical imaging and therapies. Full-wave simulations show near-perfect transmission from either side of the skull while preserving imaging information and enhancing focused acoustic energy for ultrasound therapies. Additional simulations evaluate the effectiveness of NHCMMs for realistic skull geometries with curvature and imperfections. The proposed NHCMM design consists of two sensor-transducer pairs on both sides of the metamaterial that detects incident waves and superimposes an active acoustic signal on an otherwise passive unit cell. By facilitating two-way acoustic transmission through the skull with NHCMMs, we lay the foundation for noninvasive brain imaging and treatment for neural disorders.

Chapter 3 uses Willis coupling to overcome some of the inherent limitations of resonance-based metamaterials and realize unit cells with extreme effective material parameters and wave steering at extreme angles for active and passive designs, respectively. Willis coupled materials couple pressure and local particle velocity fields to simultaneously excite monopole and dipole scattering, which results in asymmetric wave transmission and reflection of airborne sound. In the first part of this chapter, we systematically realize an arbitrarily given Willis coupling between the pressure and velocity fields for asymmetric wave propagation by an acoustic grating with inversion symmetry breaking. This acoustic bianisotropic grating is designed by optimizing the unit cells with a finite element method to achieve the desired scattering wavevectors determined by the bianisotropic induced asymmetric wave propagation. The symmetry and Bloch wavevectors in the reciprocal space resulted from the grating are analyzed, which match with the desired scattering wavevectors. The designed structures are fabricated for the experimental demonstration of the bianisotropic properties. The measured results match with the desired asymmetric wave scattering fields.

For the active metamaterial, we repurpose the tunable feedback loop circuits from chapter two and implement Willis coupling to drastically extend the tunability of the effective density and bulk modulus. The accessible parameter range is enlarged by at least two orders of magnitude compared to that of a non-Willis metamaterial. Traditional active metamaterial designs are based on local resonances without considering the Willis coupling that limit their accessible effective material parameter range. The Willis coupling results from feedback control circuits with unequal gains. These asymmetric feedback control circuits use Willis coupling to expand the accessible range of the effective density and bulk modulus of the metamaterial. The extreme effective material parameters realizable by the metamaterials will remarkably broaden their applications in biomedical imaging, noise control, and transformation acoustics-based cloaking.

Chapter 4 uses transformation acoustics to correct beamformed waves that propagate in anisotropic media. Transformation acoustics correlates complex material properties in physical space to distorted wave manipulations in virtual space, such that wave propagation patterns can be determined by mathematical coordinate transformations. These transformations allow for accurate modeling of acoustic propagation in complex materials. Such models are relevant to both biomedical ultrasound therapies and integrated on-chip systems, where muscle fibers and piezoelectric substrates behave as effective anisotropic media respectively. Without considering the anisotropic density of these sophisticated media, attempts to beamform acoustic patterns by phase engineering results in a heavily distorted signal. This distortion is detrimental to the performance of high intensity focused ultrasound (HIFU) acoustic tweezers for noninvasive surgeries, cell trapping, and cell sorting. We demonstrate that the distortion effects can be corrected by transformation acoustics in which the phased array profile is adjusted to account for the corresponding anisotropy. We perform experiments to verify this transformation acoustic correction for arbitrary focused and self-bending beams with two-dimensional anisotropic spoof surface acoustic waves (SSAW). The benefit of transformation acoustics in suppressing undesired anisotropic effects on beamformed waves improves the precision and efficacy of medical treatments that facilitate noninvasive ultrasound therapies and integrated on-chip applications.

CHAPTER 2

NON-HERMITIAN COMPLEMENTARY ACOUSTIC METAMATERIALS

This thesis chapter contains material that has been published in Applied Physics Letters [20] and Frontiers in Mechanical Engineering [21].

2.1 Introduction

Ultrasound is considered one of the most biocompatible imaging modalities as it requires no ionizing radiation, penetrates deep into biological tissue, and offers superior resolution compared to other imaging techniques [22]. As a result, high frequency ultrasound has been applied safely for non-invasive imaging and medical diagnosis for decades [23]. This unique biocompatibility inspires researchers to explore alternative ultrasound applications that go beyond imaging. For example, high intensity focused ultrasound (HIFU) concentrates acoustic energy to a focal point within the body to ablate tumors [24-29], pulverize kidney stones [30,31], and open the blood brain barrier for direct drug delivery to the brain [32]. Further ultrasound based, non-invasive therapies clear aortic plaque [33,34], accelerate bone fracture healing [35-37], and assist in gene therapies [38,39]. In addition to direct therapeutic applications, high frequency ultrasound is commonly used to image organs and tissue for diagnostic purposes [40-44]. With the help of microbubble and nanodroplet contrast agents, ultrasound serves as a high resolution, deep tissue imaging modality used to track blood flow and detect locations of arterial plaque build-up throughout the body [45]. Ultrasonic therapies have even been proposed to treat neurological disorders, with some researchers already implementing these therapies. After short, low-intensity pulses of ultrasound targeted the thalamus of a patient suffering from a disorder of consciousness due to a severe traumatic brain injury, near immediate improvement of their condition was exhibited with continued improvement over a several-day time span [46].

Although high frequency ultrasound increases the precision and spatial resolution of the aforementioned biomedical applications, major challenges exist to adapt these techniques for brain imaging and brain therapies. The primary problem is the presence of the skull that acts as a highly mismatched impedance barrier with strong attenuative effects. This lossy acoustic barrier causes a strong reflection at the boundary of these two biomaterials [47] and limits the transmission of ultrasound energy into the brain. This drastically reduces the effectiveness of HIFU and prevents diagnostic brain imaging [48]. To mitigate the scattering and loss caused by the skull, acoustic metamaterials use transformation acoustics to enable bidirectional acoustic transmission into the brain, paving the way to non-invasive diagnostic brain imaging and non-invasive brain therapies. Complementary metamaterials (CMM) are designed with the negative real effective properties of an acoustic barrier to effectively counteract any impedance mismatch effects and transmit acoustic waves through lossless impedance barriers [49]. While this is effective for enhancing the transmission through an energy conservative barrier, the intrinsic loss induced by the highly porous skull makes this method impractical [47]. This loss is characterized by the imaginary parts of the material parameters and significantly affects the total acoustic impedance. The purely real-valued sound speed and density of the CMM will not fully characterize the complex skull impedance and cause an impedance mismatch between the metamaterial and skull. In addition, the intrinsic loss dampens a significant amount of acoustic energy that results in low wave transmission through the barrier that is infeasible for use in ultrasonic brain imaging.

In this work, we apply a non-Hermitian complementary acoustic metamaterial (NHCMM) with energy gain to counteract the strong impedance mismatch and intrinsic loss of the skull simultaneously for the realization of noninvasive ultrasonic brain imaging through an intact skull in full-wave simulations (Fig. 2.1a). We obtain the desired values of the NHCMM material parameters that enable near perfect transmission and wavefront restoration when high frequency ultrasound propagates through the combined layers of NHCMM and skull. Full-wave simulations show near-perfect transmission from either side of the skull while preserving imaging information and enhancing focused acoustic energy for ultrasound therapies. Additional simulations evaluate the effectiveness of NHCMMs for realistic skull geometries with curvature and imperfections.

2.2 Idealized fluid simulation

To achieve our objective, we begin with a simplified model of the system that consists of the NHCMM and skull layers adjacent to each other (Fig. 2.1b). The top part of the patient’s head is assumed to be submerged in water; therefore, the background medium outside the human body is modeled as water as well as the brain due to its similar mechanical properties. Only the longitudinal waves supported by water are considered in this section of this chapter. The effect of the shear wave propagation in the skull is investigated in Section 2.3. By applying continuity boundary conditions at each of the boundaries in Fig. 2.1b, we observed that a solution given by $\rho_1 = -\rho_2$ and $c_1 = -c_2$ gives

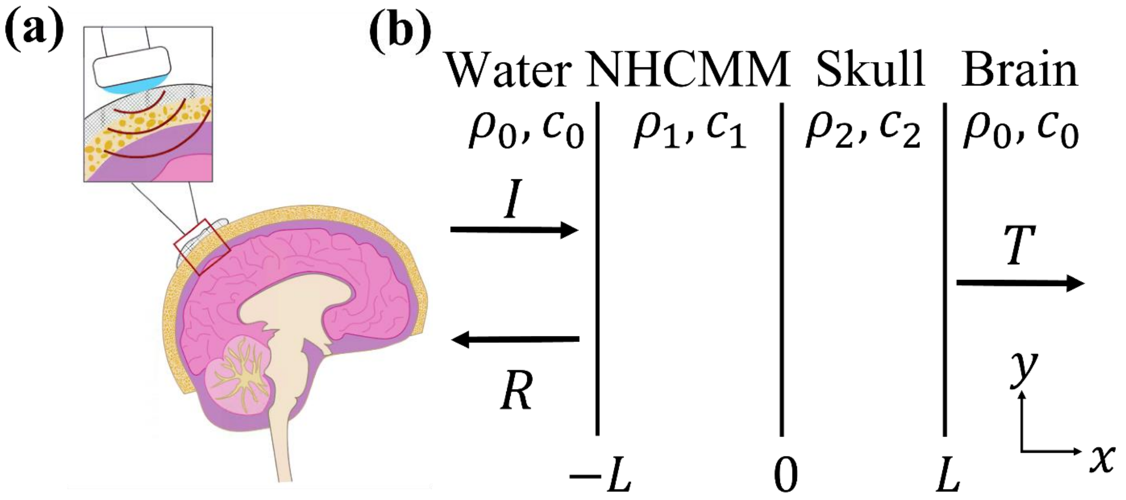

Figure 2.1: NHCMM for noninvasive ultrasonic brain imaging. (a) Schematics of the application of NHCMM for ultrasonic brain imaging through an intact skull. (b) Simplified model of acoustic wave propagation through the combined NHCMM and skull layer with an incident wave outside of the top part of the patient's head submerged in water. The acoustic properties of the brain are similar to those of water and are simulated as water.

a total transmission ($T = 1$) and no reflection ($R = 0$). Variables ρ and c are the density and sound speed of longitudinal waves and the subscripts 1 and 2 denote the NHCMM and skull, respectively. We note that ρ_2 and c_2 are complex-valued because of the intrinsic loss properties of the skull. Therefore, ρ_1 and c_1 are the direct opposite complex-valued material parameters of skull.

Physically, this opposite density and sound speed results in an identical acoustic impedance and an opposite refractive index of the NHCMM when compared with the skull. These material parameters suppress the impedance mismatch of the barrier [49] while the opposite imaginary parts indicate that the NHCMM contains active gain materials that compensate the wave attenuation through the lossy skull layer. The negative real parts of the NHCMM material parameters can be realized by resonating structures [4-6], while the imaginary parts are contributed by active gain elements, achievable by adding piezoelectric materials connected with amplification circuits used in the realization of parity-time (PT) symmetric acoustics [50], nonreciprocal propagation [51], and time reversal signal processing [13]. Designing the circuit parameters to realize double negative complex material parameters operating in the desired frequency range is discussed in Section 2.5. While total transmission can be realized at the exceptional points of PT symmetric acoustics where active gain units were used [11], the physics of NHCMM and PT symmetric acoustics are completely different. PT symmetry requires the material parameters to satisfy $\rho_1 = \rho_2{}^*$ and $c_1 = c_2{}^*$ [52-55], where the superscript * denotes the complex conjugate of the corresponding parameter, which does not hold for the NHCMM. In physics, the total transmission and zero reflection is true for waves incident from both sides of the bilayer structure, making the whole system energy conservative.

Because the goal of this section focuses on obtaining the material parameters of the NHCMM for noninvasive ultrasonic brain imaging where high frequency acoustic waves are used, we conducted our calculations at 1.5MHz. At this frequency, the measured effective density and sound speed of longitudinal acoustic waves are 1900 kg/m^3 and 2835 m/s with an acoustic attenuation of 25 dB through a 4 mm thick human skull sample [47]. These acoustic properties are closely equivalent to complex-valued material parameters $\rho_2 = (1900 + 50i)$ kg/m^3 and $c_2 = (2835 + 80i)$ m/s in numerical calculations. These values are obtained based on the loss characterization and parameter retrieval used in Refs. [51,56], where i is the imaginary unit. These complexed-valued parameters are therefore used in our studies. From our analytical derivation listed above, the density and sound speed of the NHCMM are chosen to be $\rho_1 = -0.9999(1900 + 50i)$ kg/m^3 and $c_1 = -0.9999(2835 + 80i)$ m/s to avoid a singularity in the calculations. The density and sound speed of water and brain ($\rho_0 = 1000$ kg/m^3 and $c_0 = 1500$ m/s) are used in our finite element simulations. The averaged thickness of human skull is $L = 10$ mm, which is used in this work.

2.2.1 One-dimensional simulations

To analyze the transmission and reflection properties of the combined NHCMM and skull layer, we calculate an acoustic plane wave propagating through the bilayer structure from both incident sides (Figs. 2.2a and 2.2b). The origin of the coordinate is set at the boundary between the NHCMM and skull, which are both 10 mm thick. For both cases, the transmission is 100% with no reflection, demonstrating the suppression of the lossy skull barrier induced by the NHCMM. The sound speeds through the NHCMM and skull are of equal magnitude but opposite sign resulting an effective zero refractive index, and hence no phase accumulation through the structure [57,58]. The interference patterns in the bilayer indicate multiple reflections in between the boundaries. Thus, the energy damped by the lossy skull barrier is balanced by the gain of the NHCMM. For both incident cases, the highest acoustic amplitude occurs at the boundary between the NHCMM and skull. For steady state, the peak acoustic amplitude reaches its highest value when the wave is incident from the water side due to the gain NHCMM amplifying the signal to a higher energy level before being damped by the lossy skull layer. In the opposite case, the wave is damped to a lower energy level in the skull layer before entering the gain medium incident from the brain side. Therefore, the energy needed to compensate for the skull loss from the active gain element of the NHCMM is smaller when the wave is scattered back from the brain.

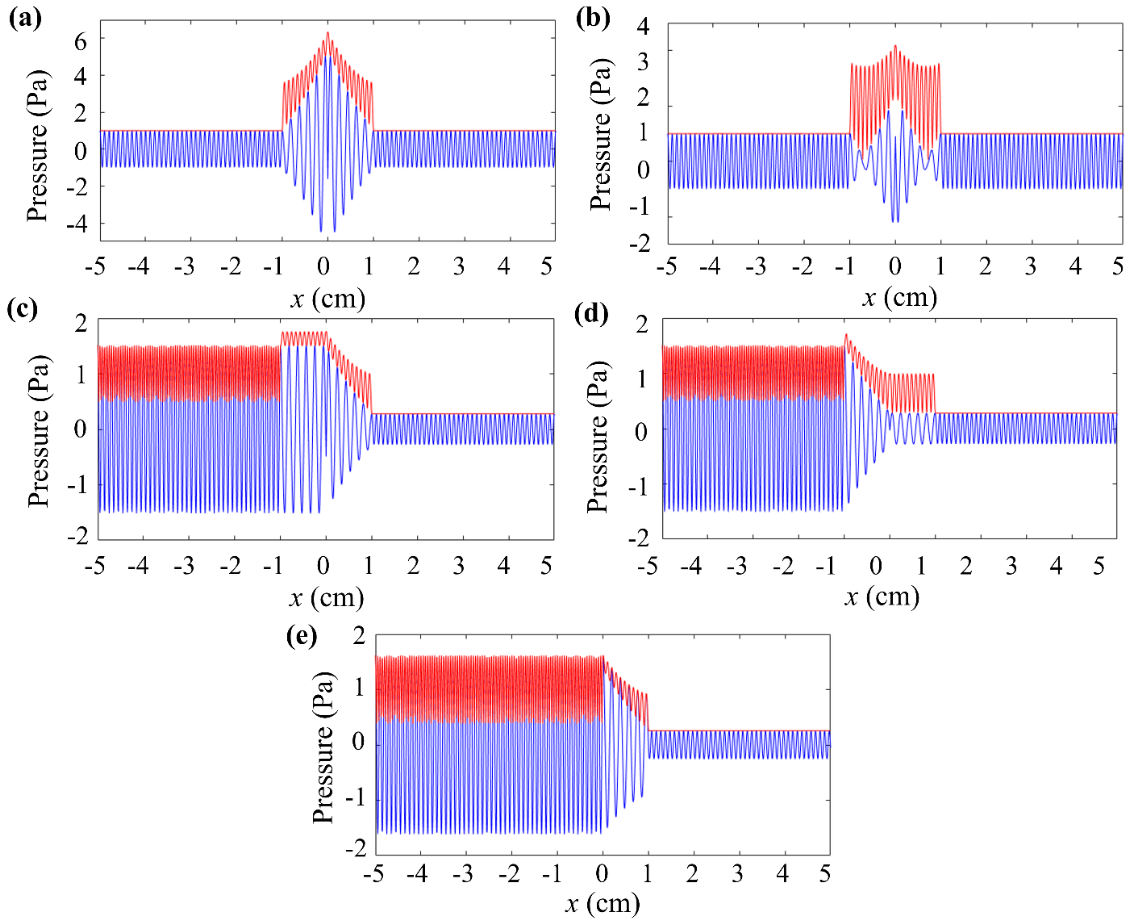

Figure 2.2: Acoustic wave propagation through the skull when compensated by (a) and (b) NHCMM and (c) and (d) CMM. The skull thickness is between 0 and 1 cm, and the complementary layer is between 1 and 0 cm for (a) and (c). The skull is between 1 and 0 cm and the complementary layer is in between 0 and 1 cm for (b) and (d). (e) Acoustic wave propagation through the skull layer. For all cases, the red curve represents the acoustic amplitude, and the blue curve represents the acoustic field.

For comparison, the acoustic transmission and reflection from the skull compensated by a CMM are also calculated (Figs. 2.2c and 2.2d) with the transmitted acoustic energy reducing to 35% of the incident (12% in terms of energy), and a strong reflection is observed for incidence from either side. It is evident that the real part of the skull impedance is affected by the imaginary parts of the material parameters. The mismatched impedance induces an acoustic reflection boundary and acoustic energy loss make the CMM ineffective, and insignificantly beneficial compared to the energy transmission direction through the skull (Fig. 2.2e).

2.2.2 Imaging with the NHCMM

The ultrasonic imaging performance is characterized by calculating the scattered acoustic field from a brain tumor through the skull complemented by the NHCMM (Fig. 2.3a). The brain tumor is modeled by a circle with a 20 mm diameter located 20 mm away from the inner boundary of the skull. The density and sound speed of the brain tumor are set to be $\rho_t = 1500$ kg/m^3 and $c_t = 2000$ m/s. For comparison, the scattered field from the same brain tumor without transmitting through the bilayer structure is calculated (Fig. 2.3b). In this case, the field we look at is 20 mm closer to the tumor than the case where the skull is compensated by the NHCMM due to the lack of phase accumulation across the bilayer (Figs. 2.2a and 2.2b). In both cases, the shadow lines of the brain tumor are observed in the reflected pressure amplitude fields. The pressure amplitude of the reflected wave along a line 20 mm away from the outer boundary of the NHCMM for both cases are plotted. The shadows are located at $y = \pm 18$ mm for both cases, indicating the existence of the circular brain tumor. These shadows demonstrate the effectiveness of the NHCMM. On the other hand, when the real part based CMM is used, most of the acoustic energy is reflected back from the bilayer and no shadow of the brain tumor is found (Fig. 2.3c), similar to directly imaging through the lossy skull layer (Fig. 2.3d). Thus, the brain tumor cannot be detected by ultrasound through the skull complemented by the CMM.

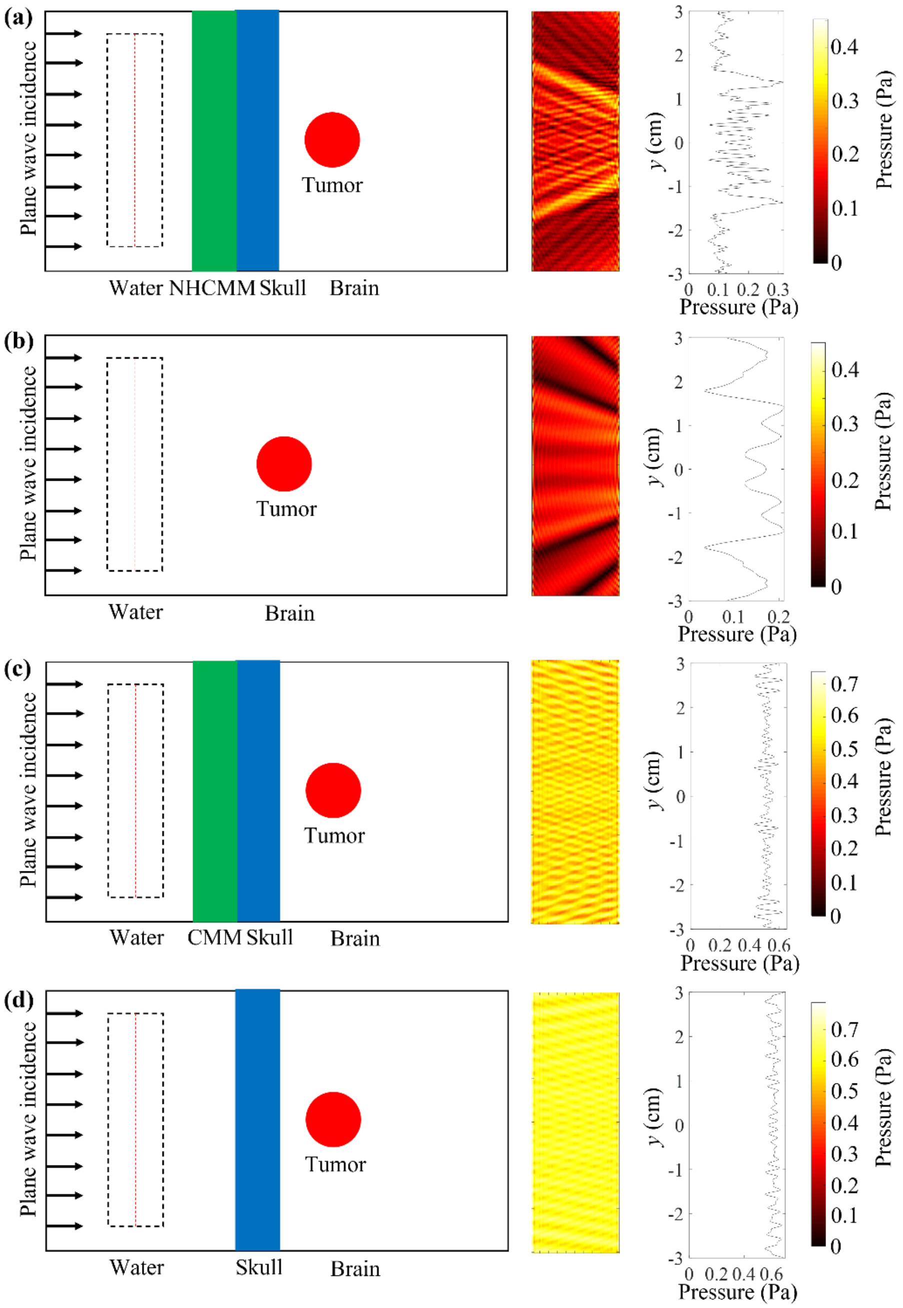

Figure 2.3: Ultrasonic imaging of a brain tumor. (a) Imaging through the skull complemented by the NHCMM. (b) Direct imaging without the skull. (c) Imaging through the skull complemented by the CMM. (d) Imaging directly through skull. For (a) and (c), the amplitude of the reflected wave in the dashed rectangle (20 mm by 60 mm) with the right boundary 10 mm away from the outer boundary of the bilayer is shown. For (b), the brain tumor is shifted 20 mm to the left compared with the other cases. For (d), the right boundary of the dashed space is 20 mm away from the outer boundary of the skull. The reflected pressure amplitudes along the red line at the middle of the dashed space for all cases are plotted.

2.2.3 High intensity focused ultrasound with the NHCMM

Another widely used type of acoustic wave in biomedical applications like neuron stimulations, ablation, thalamotomy, and drug delivery [26,31,59,60] is focused ultrasound. The propagation of waves generated by a curved focused ultrasound transducer through the skull complemented by the NHCMM compared with the focused wave without the skull are also calculated (Figs. 2.4a and 2.4b). The two cases have a similar focusing effect with almost the same amount of energy concentrated at the focal point. When the skull is compensated by the CMM, the acoustic energy has the same focal point, but at a much lower energy level (Fig. 2.4c). This is because the refractive index of a medium is determined by the real part of the sound speed. With the same real part of the sound speed, the refractive index of the CMM is identical to that of the NHCMM, resulting in the same wave refraction and focusing effect. However, the CMM does not compensate the lossy skull, resulting in a much lower focal energy. For the case without any complementary layer, the ultrasound through the skull directly focuses at a point approximately 30 mm to the left compared with the other cases (Fig. 2.4d). This is because the skull has a different refractive index compared with the water and brain, and the resulted wave refraction changes the location of the focal point. The focused acoustic energy is also low because most of the acoustic waves are reflected or damped by the skull.

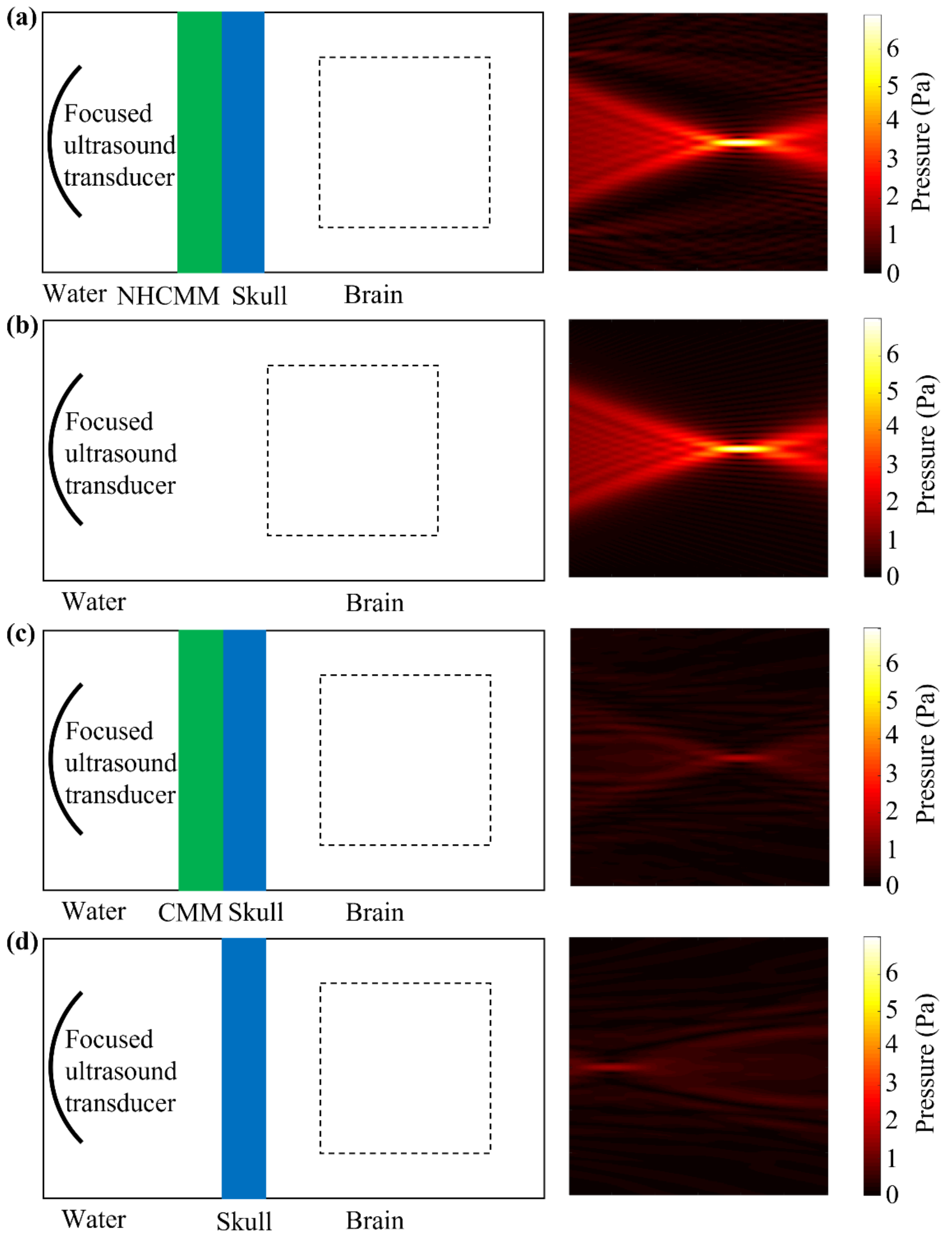

Figure 2.4: Focused ultrasound generated by a curved transducer. (a) Focusing through the skull complemented by the NHCMM. (b) Focusing without the skull. (c) Focusing through the skull complemented by the CMM. (d) Focusing directly through the skull. The pressure amplitude in the square (60 mm by 60 mm) is shown. The left boundary of the square is 20 mm away from the inner boundary of the skull for (a), (c), and (d). The square is shifted 20 mm to the left for (b) compared with the other cases.

2.3 Poroelastic simulations

Porosity is the primary contributor to acoustic attenuation through the skull and drastically reduces acoustic energy transmission into the brain. The porous loss and elastic effects of the skull are considered and studied in finite element simulations with Biot's model. In doing so, we compare the results of NHCMMs coupled to a poroelastic medium with the previously simulated fluid effective medium model. In order to obtain an equivalent poroelastic model, we match the acoustic reflection and transmission of a plane wave though a 10 mm thick layer of skull (Fig. 2.5e).

The material parameters used in Biot's model reflected the real values of the complex density and sound speed used in the fluid model determined by measured values, while the porous loss is based on poroelastic parameters of cortical and cancellous bones [61,62]. Equating the transmission and reflection amplitudes of the poroelastic and fluid models relies on slightly tuning the Biot parameters influencing the energy dissipation caused by the skull. The porosity, permeability, and characteristic pore size of the poroelastic model are the primary influences of loss through isotropic structures and found to match the fluid model with values of $6x10^{-13}$ m^2, 0.47, and 110 µm, respectively. With the proper parameter values, further analysis of the effects of NHCMM can be determined. Using an identical geometric set up as the fluid effective medium simulation in one dimension, the reflection and transmission through a porous skull coupled to a NHCMM is calculated and exhibits total transmission when a plane wave is incident on the metamaterial side (Fig. 2.5a), similar to the fluid effective medium model. Thus, the energy damped by the porous skull layer is compensated by the gain in the NHCMM, maintaining energy conservation. Flipping the geometry such that the plane wave is first incident with the porous skull shows near total

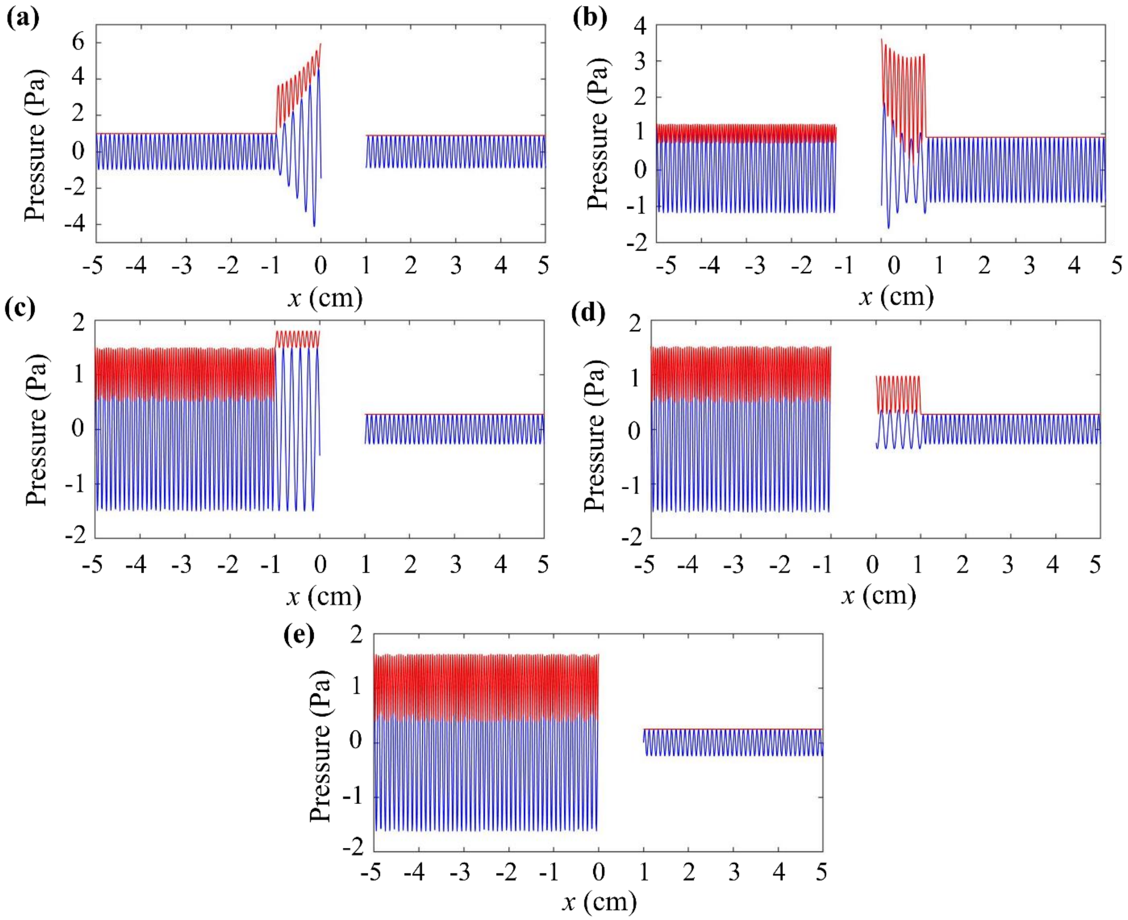

Figure 2.5: Acoustic wave propagation through a porous skull simulated with a poroelastic layer using Biot's model when compensated by (a, b) NHCMM and (c, d) CMM. The skull thickness is between 0 and 1 cm, and the complementary layer is in between -1 to 0 cm for (a) and (c). The skull is in between -1 to 0 cm and the complementary layer is in between 0 to 1 cm for (b) and (d). (e) Acoustic wave propagation through the porous skull layer. For all cases, the red curve represents the acoustic amplitude, and the blue curve represents the acoustic field

transmission with a small reflection (Fig. 2.5b). From reciprocity, we expect the transmission to be 100% with zero reflection. The observed near total transmission with a small reflection could be a result of the numerical effect of COMSOL Multiphysics when coupling poroelastic media with non-Hermitian physics. Comparing the results of the skull compensated by a CMM design based only on the real parts of the material parameters shows a significant transmission loss and reflection from the bilayer system (Figs. 2.5c and 2.5d).

The transmission amplitude is reduced to 35% of the incident wave along with a strong reflection from either incident side, matching what was observed in the fluid model. The real parameter mismatch is the cause of the strong reflection and reduced transmission, comparable to the single layer skull and confirming the ineffectiveness of poroelastic material complemented with a CMM just like the fluid model has shown.

2.3.1 Imaging through a poroelastic skull with a NHCMM

To confirm the NHCMM is effective for the imaging application, an ultrasonic plane wave is transmitted through the bilayer structure to calculate the back scattering field caused by a brain tumor (Fig. 2.6a). The density and sound speed of the brain tumor are $\rho_t = 1500$ kg/m^3 and $c_t = 2000$ m/s, the same as those used in the fluid model. The shadow in the scattered field caused by the tumor can still be visualized, demonstrating the effectiveness of the NHCMM in the poroelastic model. Comparing the results to the fluid equivalent shows a reduction in the contrast of the shadow. This is due to the information carrying in-plane k-vectors that cause minimal longitudinal wave energy to be converted to the shear mode. This mode conversion results in losing part of the imaginary information. Alternatively, using the CMM results in a strong reflection from the bilayer. The shadow of the brain tumor is not observed (Fig. 2.6b). The back scattered field through the CMM and skull bilayer is similar to imaging through the skull directly (Fig. 2.6c).

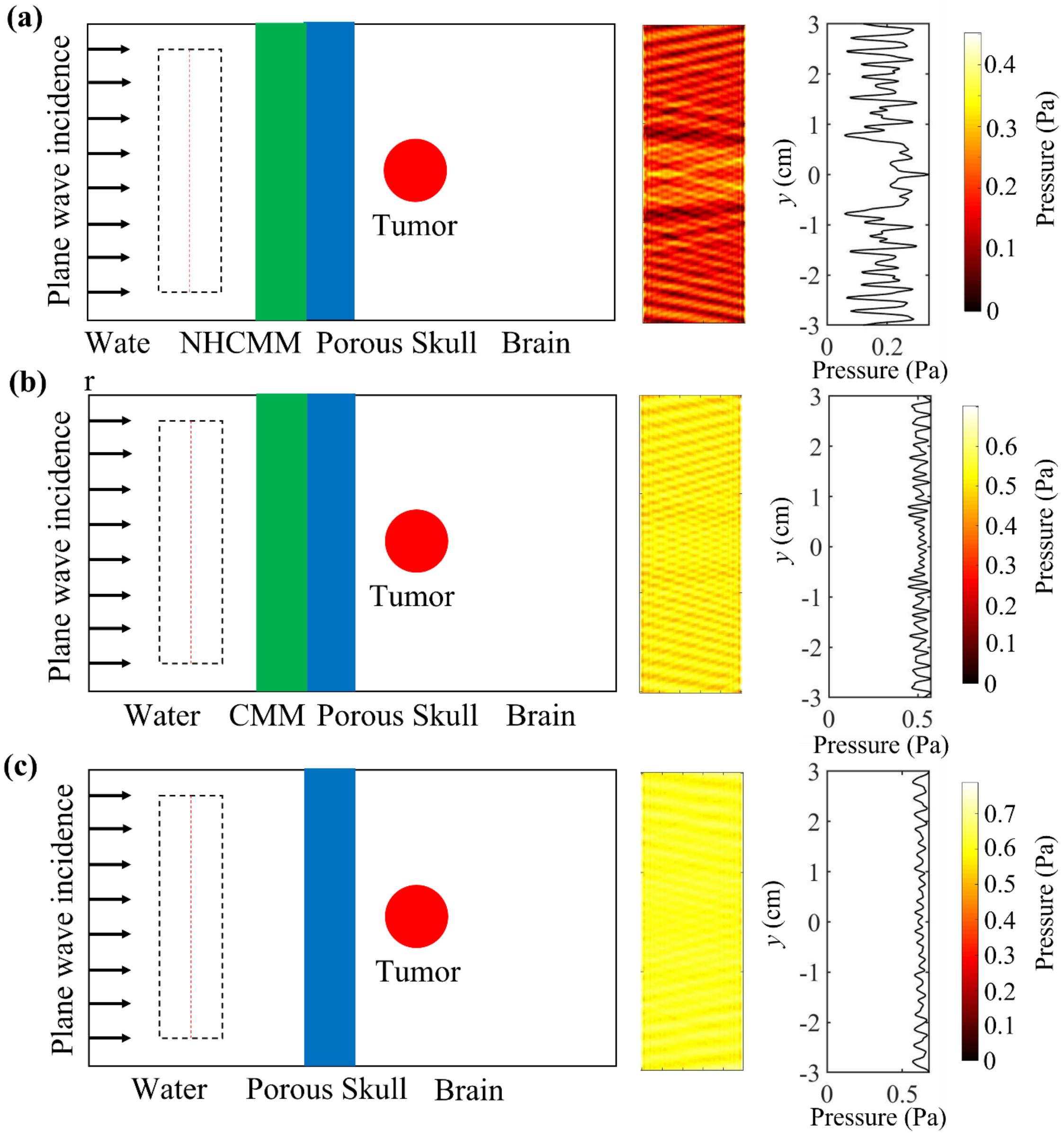

Figure 2.6: Ultrasonic imaging of a brain tumor through a porous skull simulated with a poroelastic layer using Biot's model. (a) Imaging through the skull complemented by the NHCMM. (b) Imaging through the skull complemented by the CMM. (c) Imaging directly through skull. For (a) and (b), the amplitude of the reflected wave in the dashed rectangle (20 mm by 60 mm) with the right boundary 10 mm away from the outer boundary of the bilayer are shown. For (c), the right boundary of the dashed space is 20 mm away from the outer boundary of the skull. The reflected pressure amplitudes along the red line at the middle of the dashed space for all cases are plotted.

2.3.2 Focusing through a poroelastic skull with a NHCMM

The propagation of waves emitted by a focused ultrasound transducer is also calculated using a porous skull coupled to a NHCMM (Fig. 2.7a). The focused acoustic beam is observed at the same point as the fluid model, but with a significant portion of the energy propagating in different directions. This is due to the large in-plane k-vectors from oblique incidence that causes a severe shear mode conversion. This mode conversion is confirmed by observing the displacement field of the porous skull in the simulation. The improvement of the performance of the NHCMM for wave focusing requires the design to match both the longitudinal and shear properties of the skull. Coupling the skull to the CMM shows the same focal point but has a much lower energy (Fig. 2.7b). Focusing an ultrasound beam through a single layer of skull illustrates a similar amount of energy transmission as the CMM complemented system; however, the focal point is shifted to the left due to the changing refractive index of the system (Fig. 2.7c).

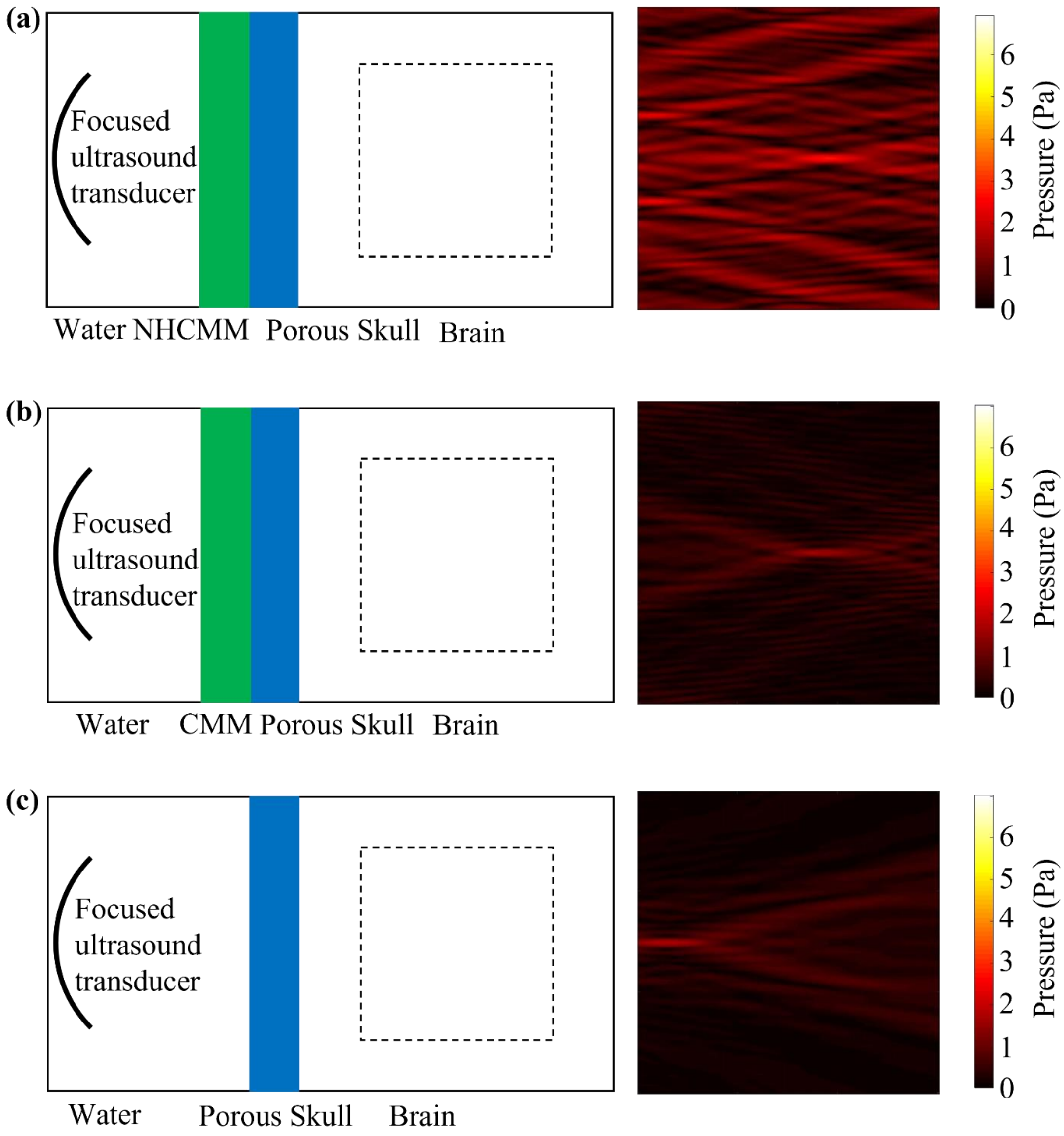

Figure 2.7: Focused ultrasound generated by a curved transducer. (a) Focusing through the poroelastic skull complemented by the NHCMM. (b) Focusing through the skull complemented by the CMM. (c) Focusing directly through the poroelastic skull. The pressure amplitude in the square (60 mm by 60 mm) are shown. The left boundary of the square is 20 mm away from the inner boundary of the poroelastic skull.

2.4 Imaging through an imperfect skull

In this section, we apply NHCMMs to skull surfaces with unique geometries and irregularities to evaluate the performance of NHCMMs under near realistic imaging circumstances. We employ a multi-step imaging process by collecting the initial reflected pressure field caused by an irregular skull region and an initial metamaterial layer that is not perfectly matched, tailor the metamaterial parameters to complement the skull region, and collect a second pressure field with the tumor present. The tumor location is ascertained by calculating the contrast to noise ratio of the higher amplitude backscattered pressure field compared to the rest of the pressure field. Even with the skull irregularities, the imaging information of an acoustic scatterer is preserved through the bilayer and reconstructible despite the scattering effects caused by the skull imperfections. Evaluating the performance of NHCMMs with various defects is critical to understanding its effectiveness for non-invasive neurological procedures and diagnostic imaging.

We consider several bone irregularities that are typical to the skull, including changes in curvature, thickness, and the presence of cavities in the skull; the NHCMM must be adaptable to ensure lossless transmission through any skull geometry for practical use of NHCMMs in the future. We construct a multilayer system consisting of the NHCMM, skull, brain tissue, and a tumor structure, with the same material properties as the previous section. After studying the initial pressure field and finely tuning the NHCMM parameters to optimize it for the complex geometry of the skull, we can detect the acoustic shadows caused by the tumor in the reflected pressure fields, demonstrating significantly improved acoustic transmission capable of detecting the tumor presence.

We evaluate the backscattered pressure field for each case to determine the efficacy of the NHCMM with near realistic skull conditions. Specifically, we measure the two-dimensional backscattered pressure field that is 60 mm wide for the sloped and blood vessel cases or 50 mm wide for the curved skull cases, and extends up 20 mm. For the curved cases, this measurement area is directly above the NHCMM boundary, and for the sloped and blood vessel cases the measurement area is 10 mm above the NHCMM. This region is illustrated in the model set-up diagrams as a rectangular region marked by a black dashed line. Additionally, we compute the pressure amplitude at the midpoint of the backscattered pressure field, indicated by a red dashed line through the center of the backscattered pressure field region. To quantify the backscattered signal coming from the tumor region, the contrast to noise ratio (CNR) is calculated by taking the average pressure amplitude of the pressure profile between x = $\pm$ 15 mm (directly above the tumor) and comparing it to the standard deviation of the noise floor taken between x = $\pm$ 25 mm and x = $\pm$ 20 mm. The formula for this calculation is $CNR = \frac{S_i - S_o}{\sqrt{\delta_i^2 + \delta_o^2}}$, where S_i and S_o are the signal amplitudes inside and outside the region of interest respectively, and δ_i and δ_o are the standard deviations of the noise inside and outside the region of interest, respectively. The exact coordinates of where the signal and background measurements are taken vary slightly from case to case, but the CNR measurements for one experimental design with tuned NHCMM and its corresponding control case with a flat non-adjusted NHCMM are calculated using the same coordinates. The CNR for ultrasound tends to be lower than optical imaging modalities due to the inherent noisiness of the background, or speckle, so

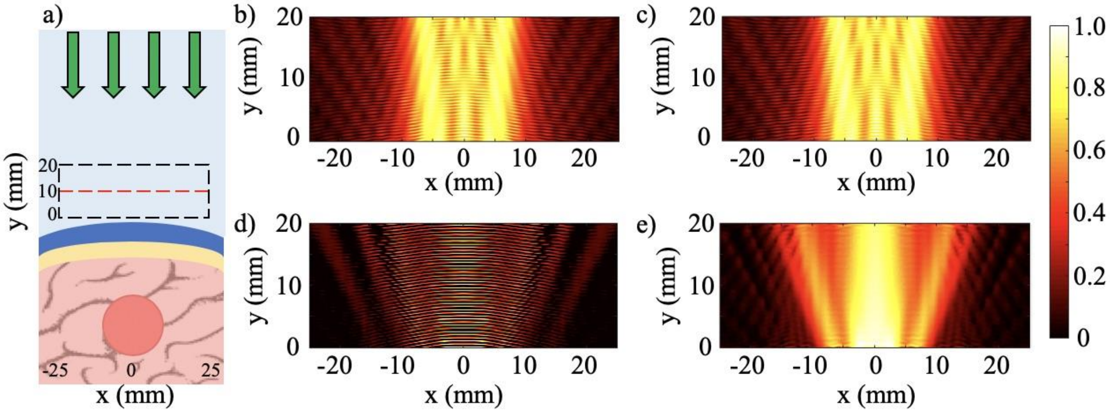

Figure 2.8: Method to retrieve tumor scattering from the total pressure field. (a) Diagram of tumor-skull-NHCMM with incident pressure (green arrows). (b) Incident and reflected acoustic pressure field of an imaging plane wave incident on a concentric NHCMM-skull bilayer with a skull radius of 100 mm. (c) Incident and reflected acoustic pressure field of the same geometry in (b) but with a brain tumor. (d) The subtraction of the measured pressure fields in (b) and (c). (e) Filtering the results in (d) using a two-dimensional Fourier transform to isolate the backscattering from just the tumor. The color bar represents the normalized pressure amplitude.

a CNR of 1.3 or greater was considered sufficient for distinguishing the tumor presence, which is greater than or on par with ultrasound and MRI papers using CNR as a quantifying metric for the quality of their images [63-65].

For the sloped skull cases, the tumor detection is calculated by collecting measurements of the scattered pressure field with the uniform 10 mm thick NHCMM and comparing the CNR of that measurement to the CNR of the scattered pressure field when the NHCMM is adjusted to match the sloping condition. For the curved, blood vessel, and combination cases, the detection of tumors through the NHCMM/skull bilayer is done by comparing the backscattered pressure field of each geometric configuration with and without the tumor present. An example of this process is exhibited in Figure 2.8, which observes the total pressure field scattered by a tumor with 10 mm radius surrounded by a curved skull with a 100 mm outer radius formed by concentric circles (Figure 2.8a). The total pressure field from the curved skull layer with no tumor is also calculated as a control case illustrated in Figure 2.8b. Adding a tumor in the same geometry results in a different backscattering pressure field but is not easily distinguishable (see Figure 2.8c). We subtract these pressure fields to determine the backscattering from only the tumor (see Figure 2.8d) and filter the result with a two-dimensional Fourier transform with the known frequency and propagation direction of the wave. An inverse Fourier transform on the filtered k-space yields the backscattered pressure field in Figure 2.8e that corresponds to the absolute value of the reflected pressure field from the tumor. Afterwards, the CNR is taken for the filtered reflected pressure field from the tumor (Figure 2.8e) as well as the unfiltered case (Figure 2.8c) which serves as a control CNR value.

2.4.1 Imaging through a sloped skull

We construct skull geometries with an internally varying thickness to understand its effect on the imaging capabilities of NHCMM. Several sloped cases are modeled, ranging from a 0.5 mm rise over a 60 mm distance (0.8% slope) to a 2 mm rise (3.3% slope), and an additional case is modeled of the skull thickness changing to be 2 mm thicker in the center of the field as compared to the edges of the imaging window (± 6.67% slope). In all circumstances, the minimum skull thickness is 10 mm. The first metamaterial for each case has a constant 10 mm thickness, matching the thickness of a uniform skull. The second metamaterial condition of each case mirrors the varying thickness of the skull; this can be accomplished by controlling the active circuit components of the NHCMM to compensate for the varying thickness, rather than altering the physical thickness of the

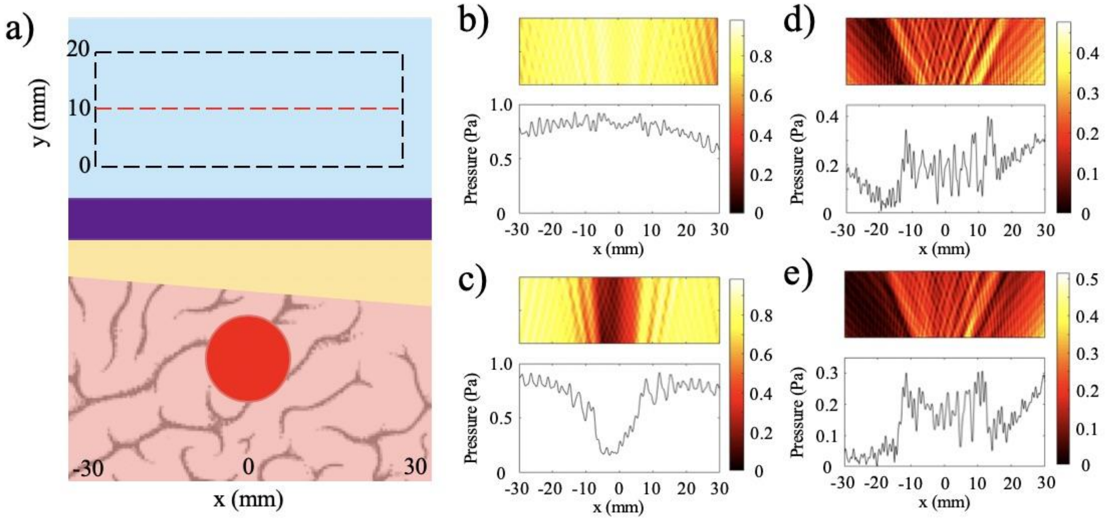

Figure 2.9: Effects of skull sloping on ultrasound imaging with NHCMM. (a) Illustration of the skull sloping model used in full wave simulations. Plane wave incidence from the top of the subfigure. Reflected pressure fields are taken in the black dashed rectangles with the pressure amplitude recorded on the red dashed line. (b) Scattered pressure field from imaging through a skull with an internal slope of 1.67% compensated by a flat metamaterial. (c) Scattered pressure field from imaging through a skull with a larger internal slope of 3.33% compensated by a flat metamaterial. (d) Scattered pressure field from imaging through a skull with a 1.67% slope compensated by a metamaterial with the mirrored skull geometry. (e) Scattered pressure field from imaging through a skull with a 3.33% slope compensated by a metamaterial with the mirrored skull geometry. The color bars represent pressure amplitudes in Pa.

metamaterial each time. In all the simulations, the material parameters are kept consistent to that of the general model.

The general setup for imaging through a skull with varying thickness is illustrated in Figure 2.9a with a plane wave incident on the NHCMM-skull bilayer with an increase in thickness of 1 mm and 2 mm (1.67% and 3.33% slope), and results shown in Figures 2.9b-2.9e. The backscattered pressure field is observed in a rectangular region denoted by the dashed black rectangle in Figure 2.9a to evaluate the performance of the metamaterial. In this case, the area is shifted 10 mm away from the metamaterial with a 60 mm width and 20 mm height. The pressure amplitude on the red dashed line in the middle of the area is also plotted. The backscattered pressure fields through the sloped skulls compensated by a metamaterial with constant thickness (10 mm) are plotted in Figures 2.9b and 2.9c for the 1.67% and 3.33% sloping geometries, respectively. In Figure 2.9b, the backscattered pressure field of the tumor is not distinguishable from the noise, indicated by the pressure field. Interestingly, the skull with greater internal slope of 3.33% (2 mm rise) has a region of minimal reflection (see Figure 2.9c). This is due to the accidental satisfaction of the Fabry-Perot condition at this bilayer thickness, resulting in a reduced pressure reflection and masking the backscattering of the tumor. Since the flat metamaterial is ineffective for imaging through the sloped skull, we alter its design to directly mirror the skull geometry. In order to non-invasively determine the internal geometry of the skull, we sweep the effective thickness of the metamaterial to satisfy the Fabry-Perot condition [66] with its effects on the reflected pressure field illustrated in Figure 2.9c. Since the NHCMM is designed with active circuit elements, we can change the resistance and capacitance values that control the active response of each unit cell in the metamaterial to alter its local effective thickness [20]. Given that the skull has sloped internal geometry, sweeping the metamaterial thickness results in a reduced pressure reflection wherever the Fabry-Perot condition is satisfied. It is important to note that when the thickness of the metamaterial exceeds the thickness of the skull, the reduced reflection that indicates the satisfaction of the Fabry-Perot condition is no longer observed. Therefore, we begin sweeping the effective metamaterial thickness at values near zero and denote the locations of reduced pressure reflections to determine the slope of the interior of the skull. Once the thickness variation is determined, the NHCMM is designed to mirror this skull geometry. With this metamaterial compensating the exterior of the skull, the resulted backscattered pressure fields imaging the tumor are illustrated in Figures 2.9d and 2.9e for the smaller and larger slopes, respectively. These pressure fields indicate the presence of the tumor with acoustic shadows located at $x = \pm 15$ mm. CNR values of 1.78 for the 1.67% slope (1 mm rise) case and 1.87 for the 3.33% slope (2 mm rise) case confirm significant contrast between the backscattered tumor signal and the surrounding brain tissue. In comparison, the CNR of the 1.67% and 3.33% slope cases with a uniform metamaterial are 0.20 and -1.64, respectively. The 3.33% slope control CNR is negative due to the Fabry-Perot resonance, causing a sharp decrease in the pressure amplitude. From these plots, it is clear that a uniform metamaterial cannot possibly resolve fluctuations in backscattered pressure caused by tumorous tissue, but adjusting the metamaterial parameters such that it matches the sloping profile enables tumor region detection with good precision.

In addition to cases with a 1 mm and 2 mm rise, we considered a 10 mm thick skull with sloped regions increasing by 0.5 mm (.83% slope), 0.75 mm (1.25% slope) and 1.5 mm (2.5% slope). These cases are presented in Figure 2.10 with both the uniform metamaterial compensation and the perfectly matched metamaterial conditions plotted. The uniform metamaterial is the same one designed in [20], which models the impact of a 10 mm thick NHCMM on the lossless transmission of ultrasound through a flat, equally thick skull region. As can be seen from the pressure amplitude profile of the backscattered pressure in the control cases (Figs. 2.10a-2.10c), it is impossible to detect the presence of abnormal brain tissue if an improperly matched NHCMM is used. Once the metamaterial is tuned to match the slope gradient (Figs. 2.10d-2.10f), an elevated pressure signal is seen in the center of the amplitude profile. The CNR values for the tuned 0.5 mm rise, 0.75 mm

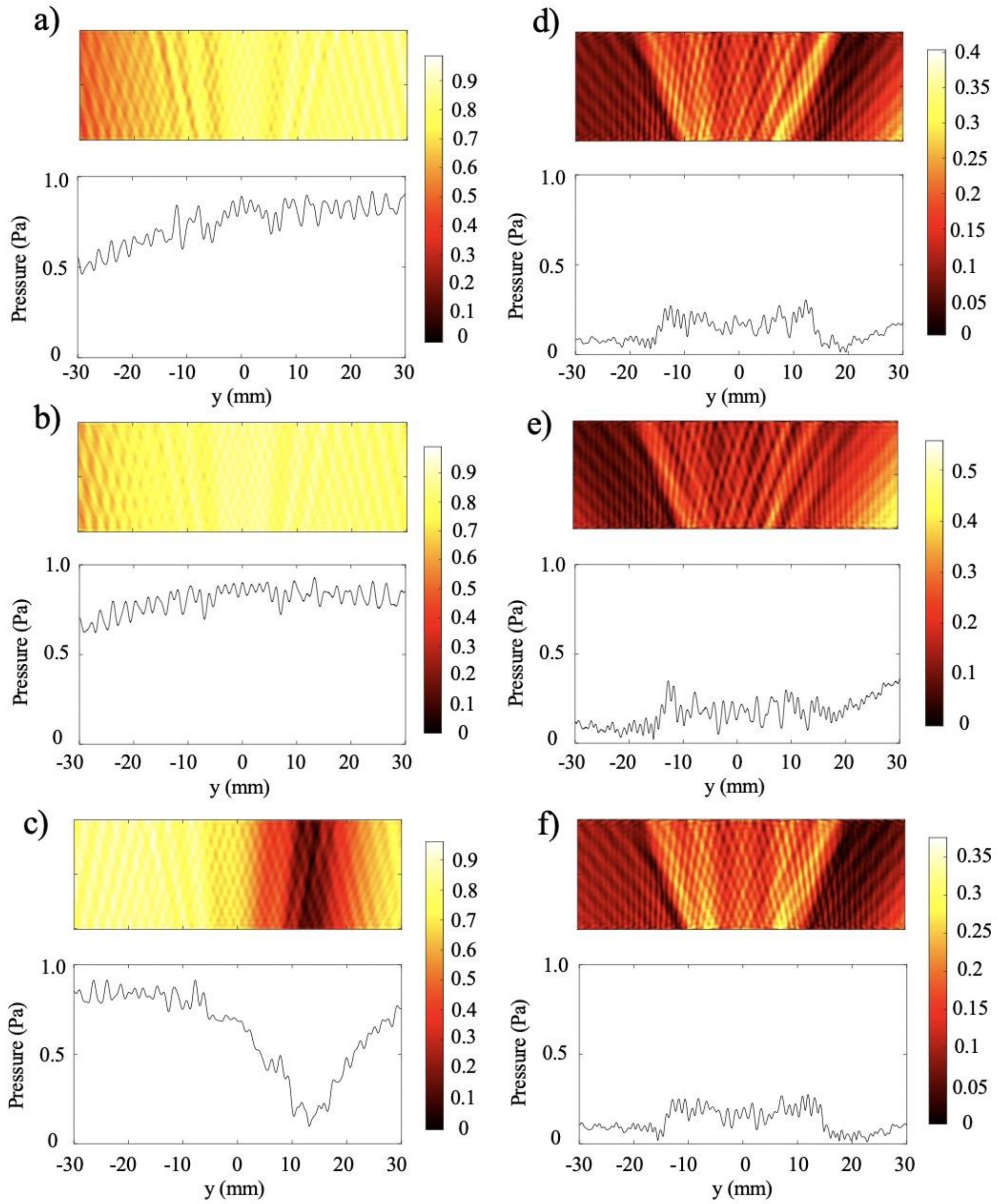

Figure 2.10: Additional skull sloping cases. (a), (b), and (c) are scattered pressure fields from skull thicknesses increasing by 0.5 mm, 0.75 mm, and 1.5 mm, respectively, with a 10 mm uniform NHCMM. (d), (e), and (f) are corresponding .83% (0.5 mm rise), 1.25% (0.75 mm rise), and 2.5% (1.5 mm rise) sloped cases with tuned NHCMM layers to match the skull thickness. The color bars represent pressure amplitudes in Pa.

rise, and 1.5 mm rise NHCMM cases are 2.40, 1.49, and 2.52, respectively, and the CNR for the uniform metamaterial cases are 0.85, 0.83, and 0.09, respectively. Even if the skull increases in thickness by only 0.5 mm over a 60 mm imaging region corresponding to a slope of 0.83%, the uniform metamaterial is completely ineffective at non-healthy tissue detection. This further demonstrates the importance of an appropriately designed NHCMM for biological conditions, and that ultrasound can diagnose tumor presence once the NHCMM matches the skull geometry.

Lastly, to determine if a tunable NHCMM can work with more complex skull geometries, the NHCMM is tested against a skull region that increases in thickness by 2 mm in the center of the imaged region (6.67% slope) and decreases back to a 10 mm thickness at the edge of the imaging region (-6.67% slope). The multi-slope model set-up and the filtered scattered pressure field with properly designed NHCMM are presented in Figure 2.11. The tumor is directly underneath the skull when it peaks in thickness (Figure 2.11a). When the flat, uniform NHCMM is applied to this skull, multiple regions of Fabry-Perot resonance appear and no tumorous tissue can be detected (Fig. 2.11b). Once the NHCMM is tuned to match the skull sloping pattern, the tumorous tissue reveals itself through the increased backscattered pressure amplitude compared to the healthy brain tissue, which has a weak reflected amplitude close to zero (Fig. 2.11c). The CNR of the tumor region compared to the background is 1.36, indicating a strong and detectable difference in pressure reflection. If a uniform, 10 mm thick NHCMM metamaterial is used instead, the CNR is -0.51, meaning the tumor tissue is completely undetectable. The variety of cases considered in this section demonstrate that the NHCMM can significantly improve glioblastoma and other brain tumor detection, so long as the NHCMM is tuned to match the skull sloping condition.

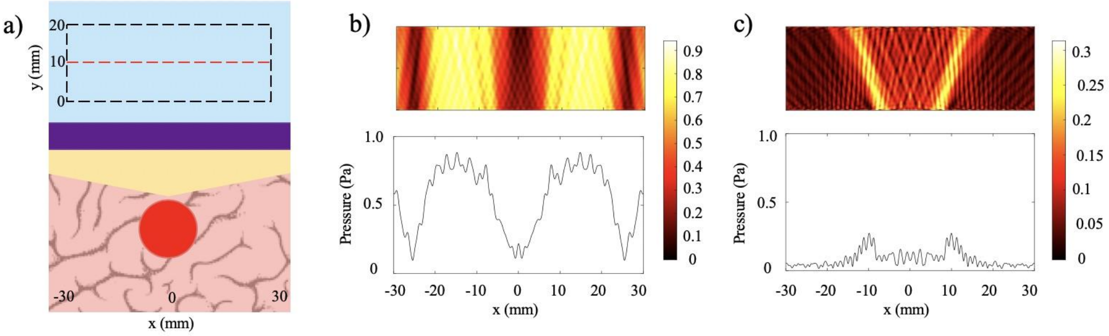

Figure 2.11 Multi-slope condition. (a) Diagram of the skull/NHCMM condition with the skull slope changing by ± 6.67%, peaking in thickness at the center of the imaging region, coupled with a uniform 10 mm thick NHCMM. (b) Scattered pressure field from the multi-slope skull coupled with a 10 mm thick NHCMM. (c) Scattered pressure field from the multi-slope skull with a NHCMM layer that matches the changes in thickness of the skull. The color bars represent pressure amplitude in Pa.

2.4.2 Imaging through a curved skull

We test the effect of skull curvature on ultrasonic imaging by simulating the NHCMM-skull bilayer with two distinct geometric configurations and two curvatures. We design the skull curvature using two different configurations to ensure that the method of creating curvature in the computer model did not significantly impact the simulation nor the NHCMM performance. The first geometric configuration considers the metamaterial and skull as a concentric bilayer of circular shells with thickness along the radial direction being 10 mm, and the skull layer having an external radius of 100 mm and 50 mm for the smaller and larger degrees of curvatures, respectively. The second geometric configuration models the skull and metamaterial as the overlapping regions of shifted circular shells with equal radii. We construct this configuration by modeling three circular arcs with center points spaced 10 mm from one another, resulting in two shell regions that represent the metamaterial and skull. Once again, this setup is studied with the two different curvatures with the radii of the skull being either 100 mm or 50 mm. Consequently, the metamaterial and skull have a slightly different thickness along the radial direction for this geometric configuration. With these geometric configurations, we evaluate the imaging capability of NHCMM compensating a skull with curvature. Each of these simulations have the same material parameters as the general model. The reflected pressure fields with and without a tumor present in the brain tissue are observed.

The results from the skull curvature studies are presented in Figure 2.12. The general setup is shown in Figure 2.12a with a plane wave incident on the NHCMM-skull bilayer having two different curvatures. The backscattered pressure field in the rectangular area enclosed by the dashed black lines is analyzed to characterize the imaging performance of the metamaterial in Figure 2.12a. The area is adjacent to the exterior of the metamaterial with a 50 mm width and 20 mm height. Within the area, the amplitude of the pressure field is measured along the red dashed line 10 mm away from the metamaterial to detect the presence of the tumor (see Figure 2.12a). We use two control cases as a basis for comparison. In the first case, a full wave simulation models plane wave incidence onto a tumor without NHCMM or skull. Without the bilayer, the observed rectangular area is shifted 20 mm closer to the tumor. The plot of the pressure amplitude indicates the presence of a tumor with acoustic shadows located at $x = \pm 13$ mm (see Figure 2.12b). For a second control case, we observe the scattered pressure field from a flat skull compensated by NHCMM. The backscattered pressure field is similar to the previous case with the acoustic shadows at $x = \pm 15$ mm to indicate the presence of the tumor in Figure 2.12c, demonstrating the effectiveness of the metamaterial. The CNR value for this condition is

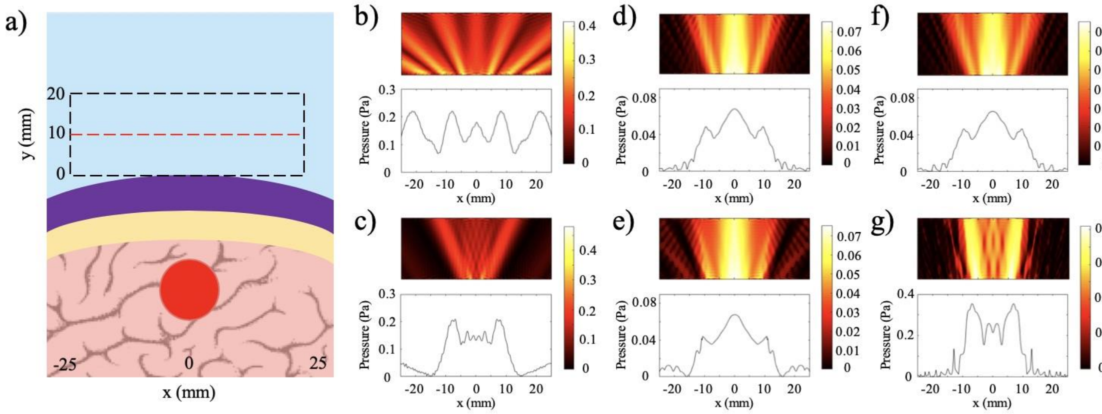

Figure 2.12: Effects of skull curvature on ultrasound imaging with NHCMM. (a) Illustration of the curved NHCMM-skull setup with a plane wave incident from the top of the subfigure. Reflected pressure fields are taken in the black dashed rectangles with the pressure amplitude recorded on the red dashed line. (b) Backscattered pressure field and pressure amplitude from a tumor without either NHCMM or skull layers. (c) Backscattered pressure field amplitude resulted from imaging through a flat NHCMM-skull bilayer. (d) Filtered pressure field amplitude resulted from imaging through a curved, concentric NHCMM-skull bilayer with an outer skull radius of 100 mm. (e) Filtered pressure field amplitude resulted from imaging through a curved, concentric NHCMM-skull bilayer with an outer skull radius of 50 mm. (f) Filtered pressure field amplitude resulted from imaging through a curved NHCMM-skull bilayer modeled by shifted circular arcs having radii of 100 mm. (g) Filtered pressure field amplitude resulted from imaging through a curved NHCMM-skull bilayer modeled by shifted circular arcs having radii of 50 mm. The color bars represent pressure amplitudes in Pa.

1.99. For the concentric skull geometries, Figures 2.12d and 2.12e illustrate the reflected pressure fields with skull radii of 100 mm and 50 mm for the smaller and larger curvatures, respectively. Here, we note that the similarity between the two cases; both indicate the presence of a tumor with acoustic shadows at $x=\pm16$ mm. The CNR values for the 100 mm and 50 mm radii are 3.14 and 2.74, respectively. For the bilayer constructed with shifted circular arcs, Figures 2.12f and 2.12g illustrate the reflected pressure fields with the skull outer radii equal to 100 mm and 50 mm for the smaller and larger curvatures, respectively. The backscattered pressure field obtained through the bilayer with the smaller curvature in Figure 2.12f shows similar results to the pressure fields in Figures 2.12d and 2.12e with an acoustic shadow at $x = \pm16$ mm. However, the pressure field resulted from imaging through the larger curvature has an acoustic shadow at $x = \pm11$ mm (see Figure 2.12g). The CNR values for the 100 mm and 50 mm shifted arc cases are 2.80 and 2.70, respectively. While both of the curvature cases modeled by the shifted arcs indicate the presence of a tumor, the difference in their acoustic shadows illustrate how the curvature affects the backscattered pressure field. On the other hand, the consistency of the pressure fields in Figures 2.12d and 2.12e demonstrates the effectiveness of the concentric bilayer geometry, illustrating that the skull curvature has a minimal effect on the resulted backscattered pressure field. Proper filtering of the backscattered pressure helps to strengthen the tumor signal and increase the CNR values, but even in the unfiltered case the CNR value is above the 1.3 threshold. Based on these models, properly designed NHCMMs that match the local skull curvature are shown to be effective for ultrasonic imaging with different degrees of curvature.

2.4.3 Imaging through a skull with blood vessels

Blood vessels in the brain may form local skull abnormalities and cause the appearance of unwanted artifacts in ultrasound images [67]. Using microbubbles as an ultrasound contrast agent, the location and geometry of major blood vessels along the interior of the skull can be determined [47]. In this case, the scattered pressure field from a blood vessel-induced indent in the skull through the NHCMM can be approximated. Simulations were modeled with hemispherical portions removed from the skull to mimic this defect. The half-ellipse portions were created using Bezier lines in COMSOL. The smaller blood vessel ellipse had a minor axis radius of 0.8 mm and a major axis radius of 4 mm, while the larger blood vessel had minor and major axis radii of 1.6 mm and 8 mm, respectively. Since the actual blood vessel has similar material properties to the tissue and water, it was modeled with the same material parameters of water. Each simulation applies the same material parameters as the general model and observe the reflected pressure field with and without tumor presence.

The results for blood vessel irregularity cases are shown in Figure 2.13 with the general geometric configuration illustrated in Figure 2.13a. The location and dimensions of the pressure field observation window match that of the variable thickness study. In particular, we study the cases of blood vessel indentations with three different locations and two different sizes. In Figures 2.13b and 2.13c, we observe the backscattered pressure fields of the NHCMM-skull bilayer with the smaller and larger blood vessel geometries, respectively. For these cases, the locations of the blood vessel indentations lie on the same axis as the tumor, resulting in the symmetric reflected fields. Here, we observe the presence of a tumor with the acoustic shadow illustrated in the plotted pressure amplitudes located at $x = \pm 18$ mm for both smaller and larger blood vessels. The CNR values for the small and large blood vessel geometries are 1.78 and 1.52, respectively. In comparison, the CNR of the scattered pressure field from the small and large blood vessel conditions without proper signal filtering is 0.37 and 0.44, respectively. The resultant pressure fields for the cases where the locations of the blood vessels shift 10 mm to the right are illustrated in Figures 2.13d and 2.13e. This shift was included in the simulation to observe the effect of blood vessel and tumor overlap on the imaging performance. The backscattered pressure fields indicate the presence of an acoustic scatterer with shadows at $x = -17$ mm and $x = 20$ mm for the small blood vessel and $x = -18$ mm and $x = 14$ mm for the larger blood vessel. The CNR values for filtered signals of the small and large blood vessel geometries shifted

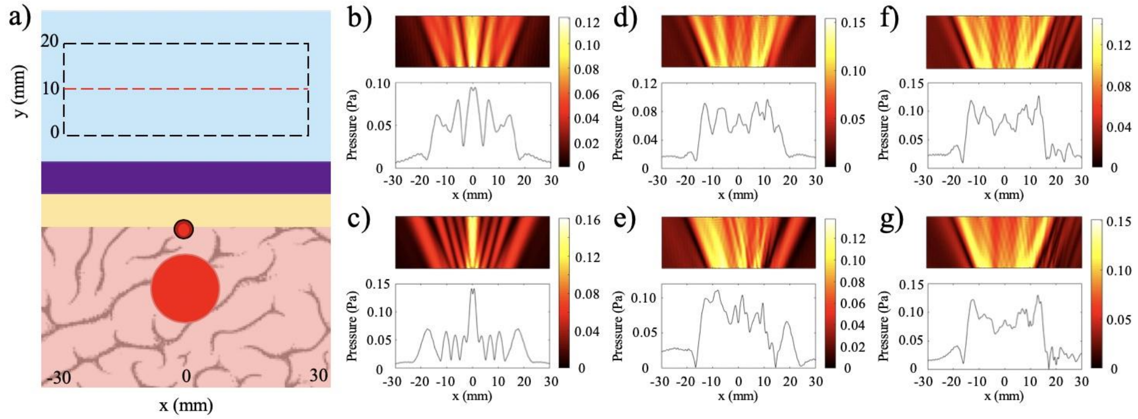

Figure 2.13: Effects of blood vessel induced indentation on ultrasound imaging with NHCMM. (a) Illustration of the NHCMM-skull bilayer with a blood vessel imprinting on the interior side of the skull. Reflected pressure fields are taken in the black dashed rectangles with the pressure amplitude recorded on the red dashed line. (b) Scattered pressure field from imaging through a skull having a small blood vessel vertically aligned with the tumor and compensated by NHCMM. (c) Scattered pressure field from imaging through a skull having a larger blood vessel vertically aligned with the tumor and compensated by NHCMM. (d) Scattered pressure field from imaging through a skull having a small blood shifted 10 mm to the right from its location in (b) compensated by NHCMM. (e) Scattered pressure field from imaging through a skull having a medium blood vessel shifted 10 mm to the right from its location in (c) compensated by NHCMM. (f) Scattered pressure field from imaging through a skull having a small blood vessel shifted 20 mm to the right from its location in (b) compensated by NHCMM. (g) Scattered pressure field from imaging through a skull having a medium blood vessel shifted 20 mm to the right from its location in (c) compensated by NHCMM. The color bars represent pressure amplitude in Pa.

10 mm to the right are 1.92 and 1.60, respectively, compared to the unfiltered signal CNR values of 0.29 and 0.47, respectively. Reconstructing the tumor geometry from this backscattered pressure field results in a shift in the tumor location. However, shifting the blood vessel another 10 mm to the right improves the symmetry of the backscattered field with acoustic shadows located at $x = \pm 17$ mm for the small blood vessel and $x = -17$ mm and $x = 18$ mm for the large blood vessel (see Figures 2.13f and 2.13g). This improvement is due to the blood vessel and tumor shift being far enough to avoid overlap. The CNR values of the filtered signals from the small and large blood vessel shifted 20 mm to the

right are 1.71 and 1.78, respectively, above the CNR threshold. The control CNR values for the small and large blood vessel 20 mm shifted case are 0.29 and 0.27, respectively. The results from these models indicate the effectiveness of NHCMMs for imaging through the skull with blood vessels. In order to detect the tumor presence with acceptable signal contrast, it is critical to properly filter the pressure signal, as indicated by the filtered signals consistently having above-threshold CNR values compared to the unfiltered signals having CNR values of 0.27-0.47. This filtering can be accomplished by tuning the NHCMM parameters to compensate for the skull indents caused by the blood vessel after using microbubble contrast agents to determine the location of the blood vessel.

2.4.4 Imaging through a skull with multiple irregularities

To ensure that the NHCMM is tunable for any skull geometry, we created a model of a skull region with a combination of skull sloping, skull curvature, and skull aberrations caused by blood vessel presence. The skull curvature was modeled by creating layers of shifted concentric circles, each with a 100 mm radius, as described in Section 2.3. We tested this geometry both with a uniform circular tumor with a 10 mm radius as well as a pear-shaped, irregular tumor 24 mm in length. The results for this case are shown in Figure 2.14, with the model conditions for the non-uniform tumor reproduced in Figure 2.14a. The skull is curved slightly and increases in thickness at the right edge of the imaging window, with a large blood vessel and corresponding hemispherical skull indent directly above the tumor. As shown in Figure 2.14b, which has the scattered pressure field from this skull shape condition and circular tumor with a precisely tuned NHCMM to match the skull

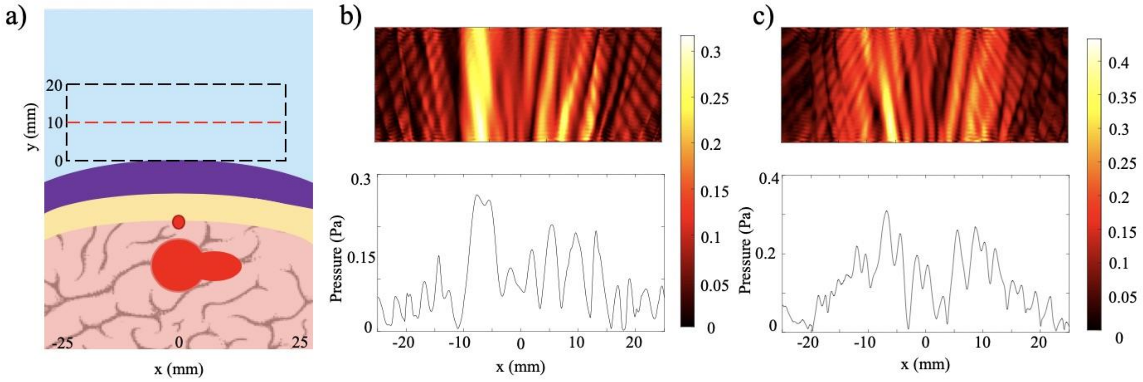

Figure 2.14: Effects of multiple skull inhomogeneities on ultrasound imaging with NHCMM. (a) Diagram of the skull, NHCMM, blood vessel, and tumor arrangement. The skull was modeled to be curved and increased in thickness towards the right end of the imaging window. The tumor in the diagram is the shape of the pear-shaped irregular tumor. A large blood vessel is located above the tumor which creates a hemispherical indent in the skull. (b) The scattered pressure field of the inhomogeneous skull with a uniform tumor and precisely tuned NHCMM. (c) The scattered pressure field of the inhomogeneous skull and irregular tumor with a precisely tuned NHCMM to match the skull geometry. The color bars represent pressure amplitudes in Pa.

properties precisely, an increase in the pressure amplitude appears in the center of the pressure field, an indicator of abnormal tissue which causes this backscatter. In Figure 2.14c, the pressure amplitude caused by the pear-shaped tumor also increases in the center of the pressure field and has a distinctly different profile from that in Figure 2.14b. The CNR of these pressure fields are 1.39 for the circular tumor and 1.96 for the irregular tumor, compared to CNR values of 0.96 and 1.39 for the circular and irregular tumor cases, respectively. Based on the CNR values for the irregular tumor, the unfiltered pressure field can still detect the tumor presence, but the filtered case provides greater contrast to help distinguish the tumor. This model provides further evidence that a properly matched NHCMM can resolve tissue abnormalities through a lossy barrier such as the skull.

2.4.5 Further discussion

The tunable NHCMM in Section 2.4 is capable of achieving lossless acoustic transmission through lossy barriers such as the skull, regardless of the skull shape or internal geometry. Previous research has investigated NHCMMs for brain imaging [20] but confined its research to a flat and homogenous skull layer, lacking consideration of the complexity of different skull regions. We prove that using a uniform NHCMM, such as the one in [20], fails to locate a brain tumor through a non-uniform skull layer in Figs. 2.9b and 2.9c, Figs. 2.10a, 2.10b, and 2.10c and Fig. 2.11b; even slight variations in the skull thickness throughout the imaging window caused the uniform NHCMM to be completely ineffective at detecting the abnormal tissue region. By incorporating active circuit components in the NHCMM, taking an initial measurement of the acoustic reflection caused by the unique skull geometry, and tuning each circuit such that the effective metamaterial parameters precisely match that skull region's geometry, perfect acoustic transmission can be achieved through lossy barriers. More specifically, the NHCMM calibrating procedure for each patient would begin by applying the NHCMM to a relatively flat skull region and adjusting the circuit components until the known reflection pulse signal from the skull disappear. When imaging through skull regions with more complex geometry, the pre-calibrated parameters will be used for fine tuning of the unit cells based on the skull non-uniformity as described in this work. Thus, this NHCMM imaging technique can be implemented in patients of all ages, head sizes, or tumor locations in the brain, as the acoustic properties of the skull are determined on a case-by-case basis and the tunable NHCMM can be altered to match those acoustic properties.

Ultrasound is already widely used for tumor detection in a variety of biological systems. In patients with early stage cervical cancer, ultrasound was capable of detecting both large (>40 nm) and small (<20 mm) tumors with high fidelity and performed better than MRI [68]. Furthermore, computer-aided ultrasound systems are capable of detecting tumors on the millimeter-scale [69]. Additionally, ultrasound is implemented in several types of neurological therapies, such as thalamic stimulation for comatose patients, and has been implemented in resolving brain vasculature in combination with microbubble ultrasound contrast agents. However, the frequency used in thalamic stimulation is much lower than typical diagnostic ultrasound such that it cannot be used for imaging, and the blood vessel imaging can only be accomplished with significant skull thinning [43]. By implementing a tunable NHCMM system, collecting a preliminary backscattered pressure field and altering the NHCMM parameters to compensate for variations in that pressure field caused by the skull geometry, tumors can be detected through the skull with high fidelity. Based on the findings in this work as well as those in the literature cited above, we anticipate that this NHCMM/skull imaging system coupled with high frequency diagnostic ultrasound can easily image millimeter-scale tumors, suggesting that tunable NHCMMs could lead to significant advances in medical imaging technology for the early diagnosis and treatment of brain tumors.

It is important to note that the NHCMMs designed in this section use plane-wave ultrasound. The resolution limits of plane-wave ultrasound imaging is determined by the full-width half max of the ultrasound beamwidth, given by the formula $FWHM = 1.206\lambda z/L$, where λ is the wavelength of the ultrasound in a given medium, calculated by dividing the incident frequency by the medium sound speed, z is the imaging depth, and L is the length of the transducer face [70]. Using a 1.5 MHz linear array transducer, the smallest resolvable object is approximately 600µm, and this resolution limit improves as the frequency increases. When this NHCMM is physically realized, the resolution will be dependent on the unit cell size of the metamaterial as governed by manufacturing limitations. However, advances in microfabrication techniques can help ensure that the physically realized metamaterial unit cell size remains on the 100 μm to mm scale, not significantly hindering the fundamental resolution limit of this technology. As for the upper limit of the tumor detection, this is dependent on the imaging window length; in order to reveal a clear difference in pressure amplitude contrast from the tumor versus the background signal, the tumor cannot fill the entire ultrasound imaging window. In the CNR analysis, a 10 mm region on both ends of the imaging window was used to establish the background signal and noise values. Since most medical imaging transducers range from 50-150 mm in length, this means that an absolute maximal tumor size detectable by this ultrasound/NHCMM design is about 130 mm. Researchers noted an average malignant glioma tumor size to be 78 mm with minimum and maximum tumor sizes of 2.8 mm and 206.6 mm [71]. It is important to note that the maximum size in that paper is inflated as it is a combination of measurements taken from multiple regions, so most tumor sizes will not reach that large. Based on this information, the NHCMM should be capable of detecting the vast majority of brain tumors, especially if used for early diagnosis.

This section modeled the NHCMM working with a variety of skull inhomogeneities, including skull curvature, aberrations caused by blood vessels, and changing skull thickness. One environmental condition not explicitly considered in these simulations is the presence of the scalp at the surface. The scalp was not included in the simulations due to having acoustic properties similar to tissue; based on the findings in [72], the thickness of skin on the scalp and forehead ranges from 1.2-1.8 mm depending on the studied region, and the change in thickness between different areas ranges from 30-100 µm, much smaller (thickness < $\lambda/10$) than the wavelength from the ultrasound transducer. Because of the scalp uniformity, we predict that the scalp presence would cause a slight phase variation in the signal, and thus was deemed not critically important in the NHCMM/skull models. In addition, the irregularities considered in this section may be more extreme than the irregularities in a thinner region of the skull. The thickness and curvature of a real human skull differs depending on the cranial bone being imaged, so imaging through a thin layer of temporal bone will be easier than through thick parietal bone at the back of the skull. Furthermore, the 10 mm skull thickness used in the simulations is representative of a worst-case scenario; in reality, most skulls range from 5.3 mm to 7.5 mm in thickness and is dependent on sex but not age [73]. We used such a thick skull layer to prove that bone thickness was not a limitation to the usefulness of NHCMM for brain tumor detection, and in reality, the resulting pressure signal from tumor/ultrasound interaction will be even stronger and more obvious.

2.5 Design of the circuit elements

We determine a method to experimentally realize NHCMMs by retrieving the elements of an active circuit used to manipulate the acoustic response of a passive material and allow full control of its effective material properties. An input signal from an active circuit has experimentally modulated the real and imaginary components of the effective density and bulk modulus of an otherwise passive material to achieve single negativity [18]. This method relies on transducers to sense incident pressure waves and drive a phase shifted signal with gain to superimpose an active acoustic signal onto the passive material response. The independence of these pressure waves are characterized by the sum of the active and passive reflection and transmission coefficients that comprise the total effective response,

$$R = R_{pass} + R_{act} \text{ ,} \tag{2.1}$$

$$T = T_{pass} + T_{act} \text{ ,} \tag{2.2}$$

where R and T are the total acoustic reflection and transmission coefficients respectively, R_{pass} and T_{pass} are the passive acoustic transmission and reflection coefficients respectively, and R_{act} and T_{act} are the active reflection and transmission coefficients respectively. The independent contributions of the passive and active components allows for the isolation of the active influence on the material. Using a feedback loop circuit, R_{act} and T_{act} are fully characterized by the coupling efficiencies of the transducers used and a constant gain [18],

$$R_{act} = \frac{h_i h_{ro} G}{1 - h_i G} \text{ ,} \tag{2.3}$$

$$T_{act} = \frac{h_i h_{to} G}{1 - h_i G} \text{ .} \tag{2.4}$$

where G represents the gain, the coupling term $h_i = \frac{v_i}{p_i}$ represents the efficiency of the input pressure and resulted input voltage on the sensing transducer, $h_{io} = \frac{v_i}{v_o}$ represents the efficiency of the voltage between sensing and driving transducer, $h_{ro} = \frac{p_r^{act}}{v_o}$ represents the efficiency of the reflected pressure wave from an output voltage, and $h_{to} = \frac{p_t^{act}}{v_o}$ represents

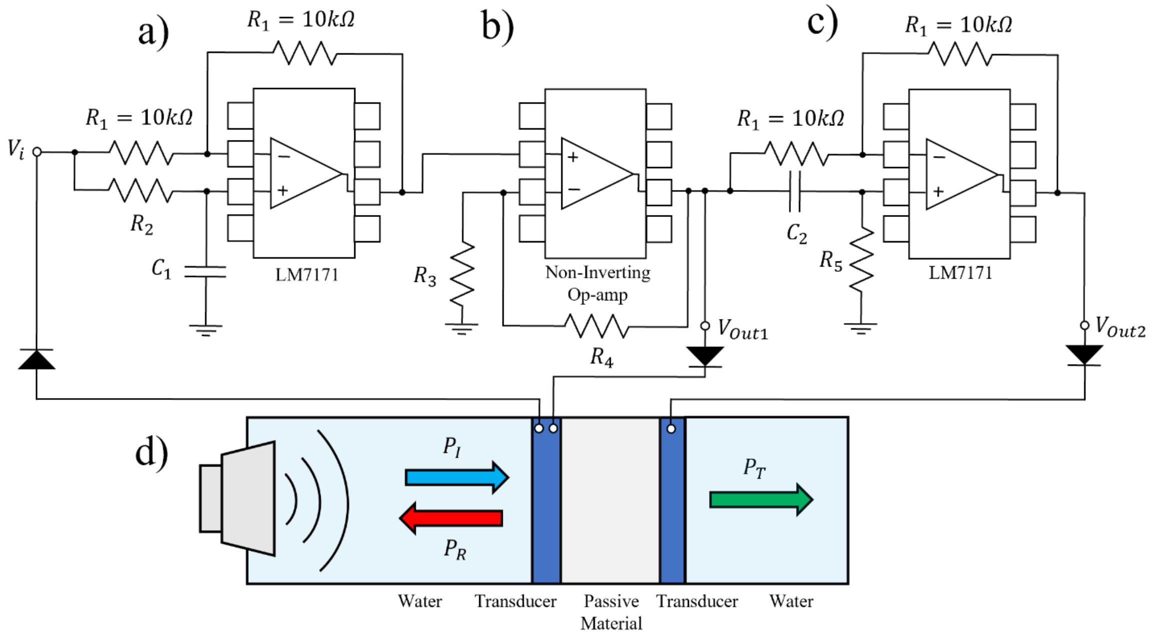
a)
b)
c)
d)
$R_1 = 10k\Omega$
$R_1 = 10k\Omega$
V_i
R_2
C_1
LM7171
R_3
Non-Inverting
Op-amp
R_4
V_{Out1}
$R_1 = 10k\Omega$
$R_1 = 10k\Omega$
C_2
R_5
LM7171
V_{Out2}
P_I
P_R
P_T
Water
Transducer
Passive
Material
Transducer
Water

Figure 2.15: Schematic of the NHCMM with a tunable feedback loop circuit (a) Phase shifting circuit for high frequency signals employing a LM7171 operational amplifier. The phase is tuned by modulating R2and C1 to achieve a desired phase from 0 to -180 degrees. (b) Active gain circuit using a Non-Inverting Op-amp to change the gain by changing the resistance values of R3 and R4. (c) Phase shifting circuit for high frequency signals employing a LM7171 operational amplifier. The phase is tuned by modulating R5 and C2 to achieve a desired phase. (d) One-dimensional waveguide employing water as the background medium to send incident signals and record the resulting reflection and transmission coefficients as a potential experimental set up.

the efficiency of the transmitted pressure wave from an output voltage. We extend this principle of superimposed acoustic responses by employing two transducers with independent phase control coupled to either side of a passive material to enable monopolar and dipolar modes that analytically demonstrate double negativity.

In order to control this parameter modulation at any frequency, we determine the reflection and transmission coefficients for the effective material with its desired density and bulk modulus as well as the reflection and transmission coefficients for a selected passive material using methods described in [56]. These known coefficients allow for the design of the active circuit components needed to achieve the determined R_{act} and T_{act}.

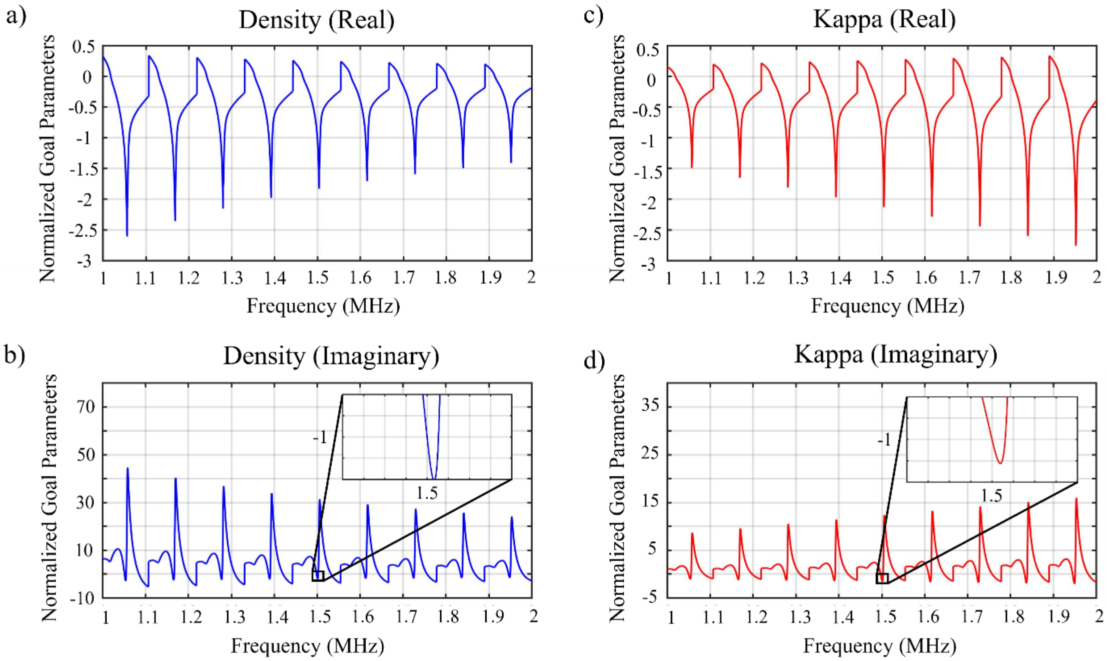

Figure 2.16: Retrieved material parameters that enable ultrasound transmission through the skull (a) Plot of the real effective density values normalized by the desired real density over a frequency range of 1-2MHz. (b) Plotting the imaginary effective density values normalized by the desired imaginary density over a frequency range of 1-2MHz. (c) Plot of the real effective bulk modulus normalized by the desired real bulk modulus over a frequency range of 1-2MHz. (d) Plot of the imaginary effective bulk modulus normalized by the desired imaginary bulk modulus over a frequency range of 1-2MHz.

We design the appropriate circuit elements by selecting a 10 mm thick layer of PDMS with density, $\rho = 969$ kg/m^3 and sound speed, $c = 1119$ m/s to represent the passive material, and the parameters of a 10 mm thick NHCMM having density, $\rho = -0.9999(1900 + 50i)$ kg/m^3 and sound speed, $c = -0.9999(2835 + 80i)$ m/s directly opposite of a human skull. Calculating the reflection and transmission coefficients of both materials at 1.5MHz require the circuit parameters satisfy the determined R_{act} and T_{act} but allow degrees of freedom for selected efficiency terms, $h_i h_{ro}$ and h_{io} in Equation 2.3. Choosing $h_i h_{ro} = 0.1$ and $h_{io} = 0.1$ and solving for the remaining unknowns yields a gain, $G = 4.2716$ with a phase, $\phi_1 = -6.95^o$ and efficiency term, $h_i h_{to}$= 0.1090 with phase $\phi_2 = 35.91^o$. The results require two independent phase shifting circuits (Figs. 2.15a and 2.15c) to independently control the phase of each transducer along with a single gain circuit (Fig. 2.15b). The values required to achieve a $\phi_1 = -6.95^o$ phase shift in Fig. 2.15a are resistance, $R_2 = 644.3\Omega$ and capacitance, $C_1 = 10$pF, while the resistor and capacitor values required to realize a $\phi_2 = 35.91^o$ phase shift in Fig. 2.15c are $R_5 = 3.438$ kΩ and $C_2 = 10$pF. To achieve the proper gain, $G = 4.2716$ the circuit in Fig. 2.15b requires a resistance $R_3 = 1$ kΩ and resistance $R_4 = 3.272$ kΩ. We facilitate a mirror image of the circuit in Figs. 2.15a-2.15c to achieve the desired material parameters for bidirectional incidence, employing diodes to filter the incident and driving signals.

With the circuit elements determined, we plot the real and imaginary effective density (Figs. 2.16a and 2.16b respectively) and bulk modulus (Figs. 2.16c and 2.16d respectively) as a function of the frequency from 1-2 MHz normalized by the desired parameter outputs. It is observed that in each plot the normalized parameter goal of negative one is achieved at 1.5MHz for each real and imaginary component, further verifying the results previously determined.

CHAPTER 3

WILLIS COUPLING

3.1 Bianisotropic gratings

This thesis chapter contains material that has been published in Applied Physics Letters [74] and the Journal of the Acoustical Society of America [75].

3.1.1 Introduction

Manipulating acoustic wave propagation facilitates the development of novel applications in numerous fields, including lensing [9], noise control [76,77], and high-intensity focused ultrasound therapies [78,79]. Due to the reversible nature of wave functions, classical acoustic waves propagate with symmetries in both time and space. Asymmetric transmission and reflection stem from breaking these symmetries for the realization of nonreciprocal acoustic propagation, inversion symmetry violation, or parity-time symmetry. A common way to achieve nonreciprocity in acoustics is by altering the frequency of incident waves using nonlinear materials and filtering unwanted frequencies with sonic crystals, enabling one-way acoustic propagation [80]. Using nonlinearities to achieve asymmetric wave propagation has also been demonstrated with active elements by coupling Helmholtz resonators with a piezoelectric material and a nonlinear circuit [51]. Alternative techniques to realize nonreciprocity have been accomplished with circular flow in a resonant ring cavity to introduce a momentum bias on the propagating wave [81]. This is an acoustic analog to the Zeeman Effect in electromagnetics, achieved by a magnetic field. Appling this approach of nonreciprocal circular flow to an array of cylindrical sonic crystals leads to the creation of a topologically protected edge state with one-way acoustic wave propagation, which is an acoustic analogy of the quantum Hall effect [82,83]. Besides breaking the time reversal symmetry with circular flow, topologically protected one-way edge states were also realized by breaking the inversion symmetry of phononic crystals that induces acoustic pseudospin, analogous to quantum spin Hall effect [84-87]. Generalizing topological acoustics in higher dimensions leads to the exploration of acoustic Weyl points and Fermi arcs, resulting in asymmetric wave propagation in three dimensions [88-90]. In addition, asymmetric wave transmission has been observed in non-Hermitian structures with pure loss effects [91]. Non-Hermitian acoustic structures with parity-time symmetry, where the loss and gain materials were exactly balanced, was demonstrated to exhibit asymmetric wave reflection while maintaining total transmission on both sides of the structure at their exceptional points [11,50,52]. Bianisotropic materials enable asymmetric wave scattering with unitary efficiency in the bulk state compared to the existing approaches [92]. Bianisotropic properties were observed in electromagnetism where a coupling tensor relates electric and magnetic fields with monopolar and dipolar moments in the scattered waves [93]. Acoustic bianisotropic materials couple the pressure and local particle velocity fields with monopole and dipole scattering resulting in asymmetric wave propagations [94-101]. In acoustics, bianisotropy describes the same phenomenon as Willis coupling. The bianisotropic material was used as an effective sound barrier [102]. The coupling between the pressure and local particle velocity fields along with the scattered acoustic monopole and dipole is characterized by a polarizability tensor. In a two-dimensional scenario, the polarizability tensor is a second order tensor given by

$$\begin{pmatrix} M \\ D_x \\ D_y \end{pmatrix} = \begin{pmatrix} \hat{\alpha}^{p} & \hat{\alpha}_x^{pv} & \hat{\alpha}_y^{pv} \\ \hat{\alpha}_x^{vp} & \hat{\alpha}_{xx}^{vv} & \hat{\alpha}_{xy}^{vv} \\ \hat{\alpha}_y^{vp} & \hat{\alpha}_{yx}^{vv} & \hat{\alpha}_{yy}^{vv} \end{pmatrix} \begin{pmatrix} p \\ v_x \\ v_y \end{pmatrix}, \tag{3.1}$$

where M is the monopole scattering, D_x and D_y are the dipole scattering along the *x* and *y* axis, p is the pressure field, v_x and v_y are the local particle velocity fields in the *x* and *y* directions, and $\hat{\alpha}_j^i$ are the elements of the polarizability tensor with *i* denoting the coupling between the pressure and local particle velocity fields and *j* denoting the coupling axes, respectively. Given an arbitrary polarizability tensor, one can obtain the scattering field of a bianisotropic particle [103]. For example, the scattering of a bianisotropic particle allowing for both forward and backward scattering, whose polarizability tensor is a function of frequency given by Fig. 3.1a, is obtained in Fig. 3.1b. Similarly, the scattering of another bianisotropic particle with a polarizability tensor given by Fig. 3.1c only permitting backwards scattering is shown in Fig. 3.1d.

In this section, we realize an acoustic bianisotropic grating with its polarizability tensor given by Fig. 3.1a at 6 kHz (wavelength equal to 57 mm). Because the bianisotropic grating we intend to fabricate is linear, the wavelength and frequency remain unchanged during the scattering process, and the incident and scattered wavevectors retain on a circle with its radius given by $k = 2\pi/\lambda = 109.9\ \mathrm{m}^{-1}$ (Figs. 3.2a and 3.2b). The Bloch wavevectors of the grating required to achieve this asymmetric wave propagation in Fig. 3.1b is given by the difference between the incident and scattered wavevectors shown by the black arrows in Figs. 3.2a and 3.2b. A -45-degree incident wave is completely reflected by the bianisotropic grating back towards the source that requires a Bloch wavevector $(-\sqrt{2}k, \sqrt{2}k)$ given by the structure (Fig. 3.2a). The time reversal of the scattering process

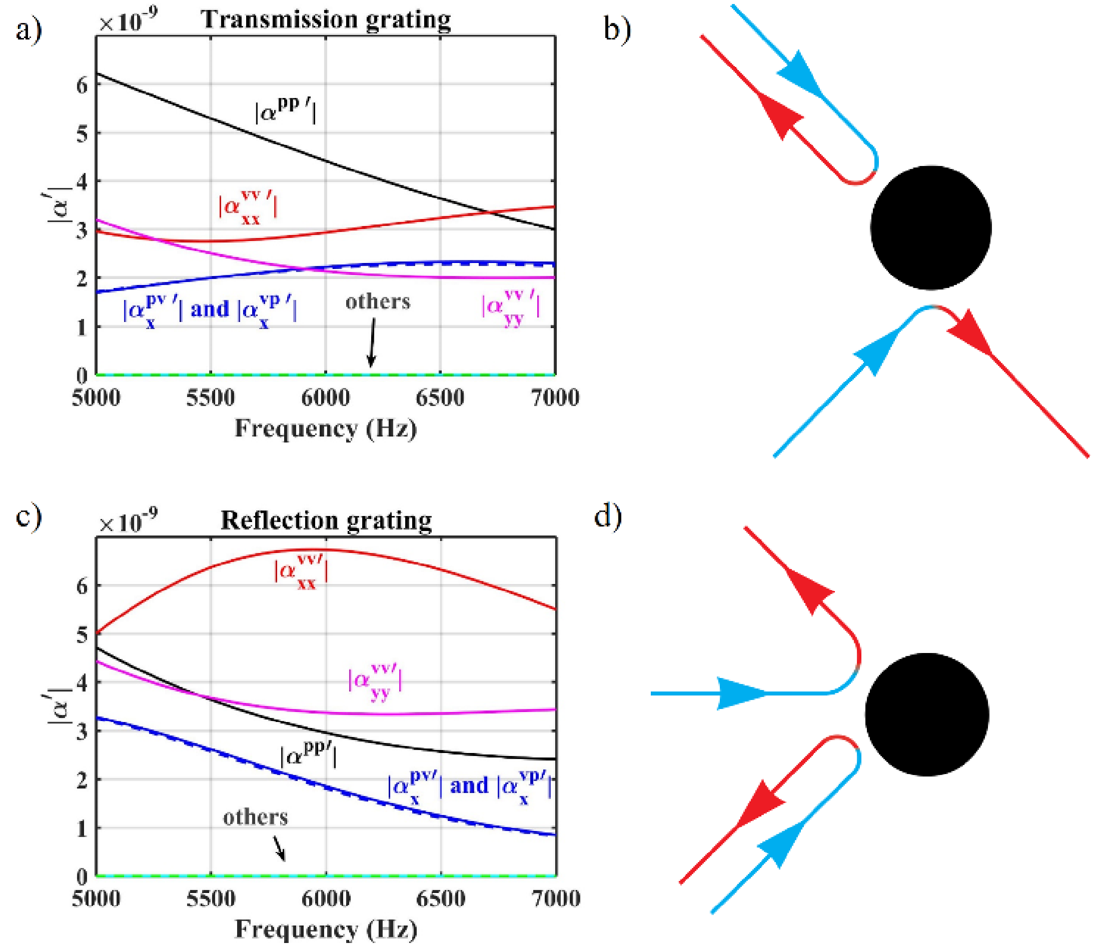

Figure 3.1: The polarizability tensor and its desired scattering outcome (a) The elements of the polarizability tensor of a bianisotropic particle that allows both forward and backward scattering as functions of frequency. (b) Asymmetric wave scattering for different incidences from the bianisotropic particle in (a). (c) The elements of the polarizability tensor of a bianisotropic particle with only backward scattering. (d) Asymmetric wave scattering for different incidences from the bianisotropic particle in (c). For both (b) and (d), the blue arrows represent incident and red arrows represent scattered waves, respectively.

for this incidence is identical to itself (Fig. 3.2a). On the other hand, a 45-degree incident wave is refracted with a total transmission in the -45-degree direction, which requires a Bloch wavevector $(0, -\sqrt{2}k)$ from the grating shown in Fig. 3.2b. The time reversal of this incident case exhibits the same refraction, confirming the preservation of time reversal symmetry in the bianisotropic grating. The asymmetric wave scattering of the -45- and 45-

degree incidents reveal the violation of parity symmetry in the *y* direction, indicating the inversion symmetry breaking of the bianisotropic grating about the *x*-axis. Thus, the mirrored Bloch wavevectors $(\sqrt{2}k, \sqrt{2}k)$ and $(0, \sqrt{2}k)$ about the x-axis are not provided by the grating. To realize this bianisotropic grating, we determine the grating periodicity from the scattered wave directions from the aforementioned polarizability tensor. The geometry of the unit cells are optimized based on a finite element method, which maximizes the scattering efficiency of the grating [35]. The resulting bianisotropic grating consists of a periodic array of scatterers along the y-axis with 40.4 mm spacing. Each scatterer consists of a rectangle having a base of 39.5 mm and height of 14.8 mm adjacent to a second rectangle with a 19.5 mm base and 21.2 mm height centered above the first (Fig. 3.2c). In order to confirm that the grating elements provide the desired scattering in Fig. 3.1b, Fourier analysis of the symmetry properties of the scattered wavevectors in the reciprocal space is performed (Fig. 3.2d), which results in the wavevectors required by the scattering in Figs. 3.2a and 3.2b.

3.1.2 Asymmetric Transmission

To verify the bianisotropic properties of the designed grating experimentally, 25 aluminum grating elements were machined by CNC milling (Fig. 3.2e). In our experiment, the grating elements were arranged in a two-dimensional waveguide with a height of 20 mm bounded by two 1000 mm by 1500 mm acrylic sheets. Plane waves were generated by a speaker array consisting of twelve 17 mm diameter speakers spaced $\lambda/2$ apart, positioned at a 45-degree angle relative to the grating with the closest edge of the array being 500 mm away from the grating (Fig. 3.2e). In order to create a consistent signal, the pressure amplitude of the speakers was controlled by a digital, multichannel

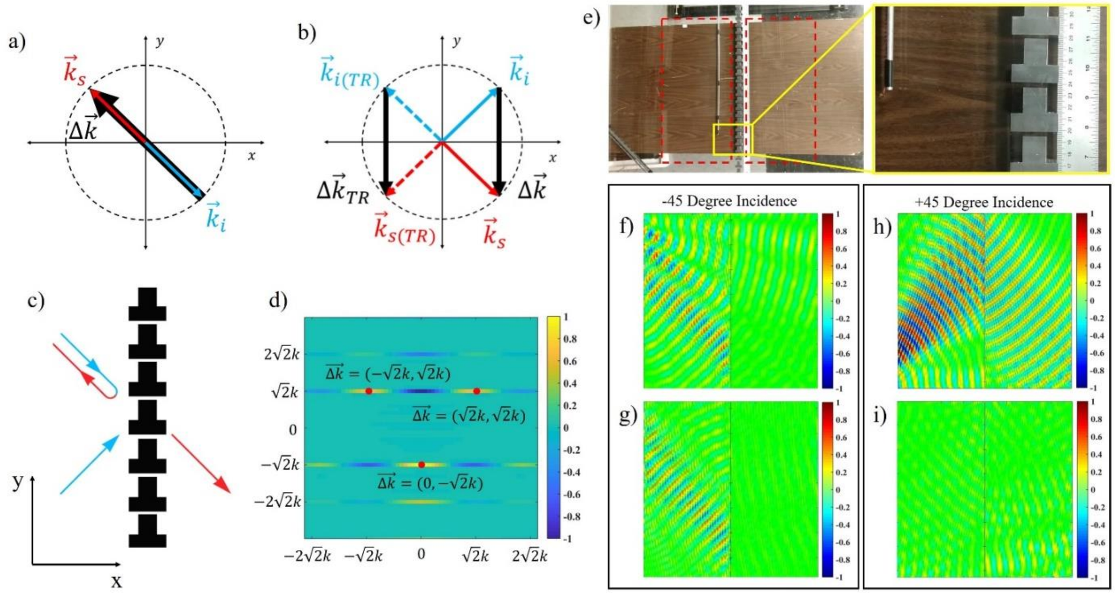

Figure 3.2: Wavevector analysis for the transmission wave-grating interaction with experiment results (a) Wave-grating interaction for the transmission case for -45-degree incidence in the reciprocal space. (b) Wave-grating interaction for +45-degree incidence as well as the time reversed case represented by the dashed lines. For both (a) and (b), the incident, scattered, and Bloch wavevectors are represented by $\vec{k}_i$, $\vec{k}_s$ and Δk, respectively. (c) Bianisotropic grating structure with asymmetric wave scattering in (a) and (b) determined by inverse Fourier analysis of the Bloch wavevectors. (d) Two-dimensional spatial Fourier transform of the grating geometry with the expected scattering wavevectors having the highest intensity. (e) Experimental set up for the bianisotropic transmission grating. The zoom out shows the detailed structure of the grating. The outlined rectangles with red dashed lines represent the scanned areas. (f) Measured pressure field of acoustic waves propagating with positive k_x component for -45-degree incidence. (g) Measured pressure field with negative k_x component for -45-degree. (h) Measured pressure field of acoustic waves propagating with positive k_x component for +45-degree incidence. (i) Measured pressure field with negative k_x component for +45-degree incidence. All the pressure fields in (f), (g), (h), and (i) are normalized by their corresponding maximum amplitude in each measurement.

recorder while an omnidirectional microphone attached to a motorized positioner measured the pressure fields for both -45- and 45-degree incidence cases. The motorized positioner was controlled by a MATLAB script to scan two 450 mm by 800 mm areas, which are 10 mm away from the grating with a scan resolution of $\lambda/10$. A lock-in amplifier records the amplitude and phase of the acoustic waves in the scan area (Fig. 3.2e). To distinguish the incident and scattered waves, spatial two-dimensional Fourier analysis is performed on the measured pressure fields, differentiating the waves with positive k_x (Figs. 3.2f and 3.2h) and negative k_x components (Figs. 3.2g and 3.2i). For -45-degree incidence, the acoustic wave is reflected back towards the source by the bianisotropic grating with pressure reflection coefficient R = 0.72 and no transmission through the grating (Fig. 3.2f and 3.2g). This experimental result matches the desired scattering of the bianisotropic structure in Fig. 3.1b with its polarizability tensor given by Fig. 3.1a. On the other hand, a 45-degree incidence results in a transmission at a -45-degree angle with pressure transmission coefficient T = 0.78 and no reflection from the grating (Figs. 3.2h and 3.2i), which matches the scattering of the bianisotropic material in Fig. 3.1b. The full wave simulations in Section 3.1.4 show near perfect reflection and transmission for the two incident cases, respectively, which indicates near perfect scattering efficiencies. The experimental error arises from the speaker array being an imperfect source that excites unwanted wavevectors. In addition, the finite dimensions of the waveguide possesses open boundaries at the edges of the acrylic sheets resulting in unwanted reflections. Further error arises from the fabrication and imperfect alignment of the grating. These experimental results confirm the feasibility for the realization of bianisotropic properties by breaking the inversion symmetry of the structure.

3.1.3 Asymmetric Reflection

The realization of a bianisotropic grating with polarizability defined by Fig. 3.1d at 6 kHz is similar to the procedure previously executed. By analyzing the wave-grating interaction in reciprocal space, the Bloch wavevectors are determined for each incidence case. We continue to use a bianisotropic grating with linear elements, the incident and scattered wavevectors are known to remain on a circle with radius k = 109.9 m^{-1} (Fig. 3.3a and 3.3b). A wave with 45-degree incidence interacting with the bianisotropic grating results in a total reflection back towards the source requiring a Bloch wavevector of $(-\sqrt{2}k, -\sqrt{2}k)$ (Fig. 3.3a). This Bloch wavevector is identical to that of the time reversal propagation. For normal incidence, the acoustic wave is fully reflected towards 135-degree direction, which requires a Bloch wavevector of $(-\left(1+\frac{\sqrt{2}}{2}\right)k, \frac{\sqrt{2}}{2}k)$ (Fig. 3.3b). The time reversal case for this incidence requires an identical Bloch wavevector, confirming the time reversal symmetry for both incidence cases. The asymmetric wave propagation for different incidence reveals the violation of parity symmetry about the x-axis. Similar to the bianisotropic grating above, the scattered wave directions determine the grating periodicity while a finite element method is used to optimize the unit cell geometry and maximize the scattering efficiency. The resulting bianisotropic grating consists of an array of scatterers having an 80.8 mm periodicity. Each scatterer consists of two rectangles: the first having a base of 18.5 mm and height of 26.5 mm directly underneath the second rectangle with a base of 9.4 mm and height of 21.2 mm (Fig. 3.3c). Analyzing the grating geometries with spatial Fourier transform reveals the resulted Bloch wavevectors in Fig. 3.3d matching the scattering wavevectors from the symmetry analysis in Figs. 3.3a and 3.3b. Inversion symmetry about the y-axis can be observed in Fig. 3.3d due to the sound hard boundary behind the grating serving as a mirror to any incident pressure signals.

The designed bianisotropic grating with thirteen elements are fabricated for the verification of the asymmetric wave scattering for the reflection only case (Fig. 3.3e). The grating elements were arranged linearly in the same waveguide described above. The

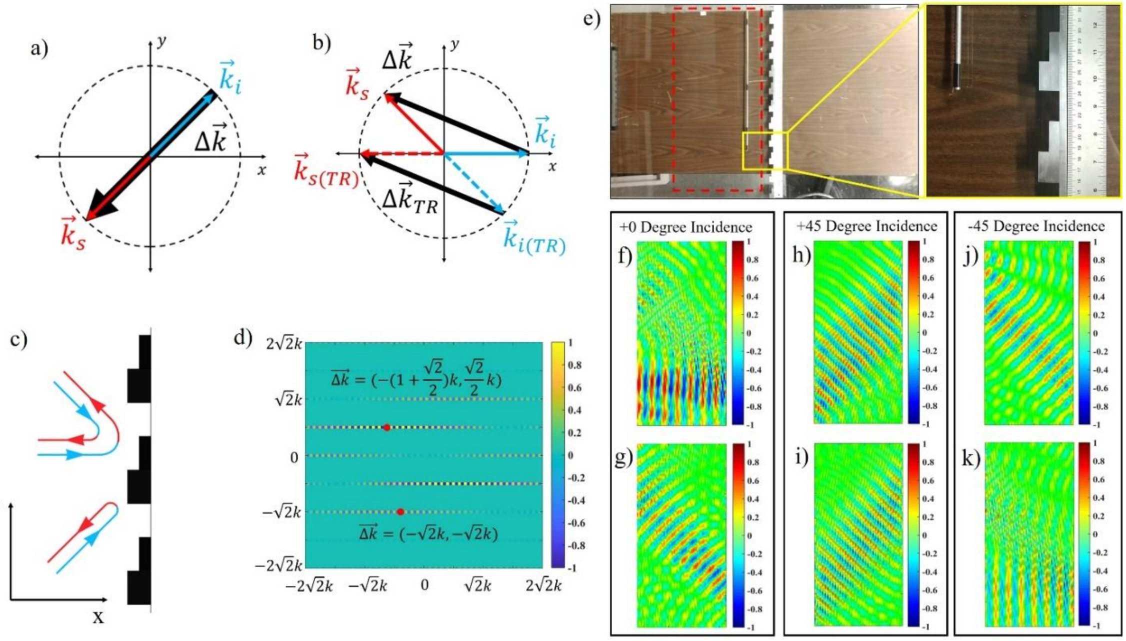
a)
b)
c)
d)
e)
$\vec{k}_i$
$\vec{k}_s$
$\Delta\vec{k}$
$\vec{k}_{s(TR)}$
$\vec{k}_{i(TR)}$
$\Delta\vec{k}_{TR}$
x
y
$\overrightarrow{\Delta k} = (-(1+\frac{\sqrt{2}}{2})k, \frac{\sqrt{2}}{2}k)$
$\overrightarrow{\Delta k} = (-\sqrt{2}k, -\sqrt{2}k)$
$2\sqrt{2}k$
$\sqrt{2}k$
0
$-\sqrt{2}k$
$-2\sqrt{2}k$
+0 Degree Incidence
+45 Degree Incidence
-45 Degree Incidence
f)
g)
h)
i)
j)
k)

Figure 3.3: Wavevector analysis for the reflection wave-grating interaction with experiment results (a) Wave-grating interaction for the reflection case for 45-degree incidence in the reciprocal space. (b) Wave-grating interaction for normal incidence as well as the time reversed case represented by the dashed lines. For both (a) and (b), the incident, scattered, and Bloch wavevectors are represented by $\vec{k_i}$, $\vec{k_s}$ and Δk, respectively. (c) Bianisotropic grating structure with asymmetric wave scattering in (a) and (b) determined by inverse Fourier analysis of the Bloch wavevectors. (d) Two-dimensional spatial Fourier transform of the grating geometry with the expected scattering wavevectors having the highest intensity to the left of the inversion symmetry about the y-axis (e) Experimental set up for the bianisotropic reflection grating. The zoomed in image shows the detailed structure of the grating. The outlined rectangle with red dashed lines represents the scanned areas. (f) Measured pressure field of acoustic waves propagating with a positive k_x component for normal incidence. (g) Measured pressure field with negative k_x component for normal incidence. (h) Measured pressure field of acoustic waves propagating with positive k_x component for +45-degree incidence. (i) Measured pressure field with negative k_x component for +45-degree incidence. (j) Measured pressure field of acoustic waves propagating with positive k_x component for -45-degree incidence. (k) Measured pressure field with negative k_x component for -45-degree incidence. All the pressure fields in (f), (g), (h), (i), (j), and (k) are normalized by their corresponding maximum amplitude in each measurement.

speaker array was positioned in the same location for angled incidence, but was relocated to the end of the waveguide, 660 mm away from the grating for the normal incidence case. The motorized positioner scanned an identical rectangular area to measure the total pressure field with both incident and scattered waves. The two-dimensional spatial Fourier analysis mentioned above is used to separate the incident and scattered waves. Experimental measurement shows a normal incidence interacting with the bianisotropic grating results in a reflection at a 135-degree angle with reflection coefficient R = 0.76 (Figs. 3.3f and 3.3g). The time reversal of this incidence is illustrated in Figs. 3.3j and 3.3k with a reflection coefficient R = 0.88. The 45-degree incident wave is reflected with a reflection coefficient R = 0.84 back towards the source (Figs. 3.3h and 3.3i). These experimental results match with the desired scattering of the bianisotropic material in Figs. 3.1e and 3.1f, whose polarizability tensor is given by Fig. 3.1d. Once again, the simulations show a near perfect reflection for each incident case in Section 3.1.4. The unwanted wavevectors produced by the imperfect source array as well as the open boundaries at the edges of the waveguide affect the reflections in the experiment as shown in the Fourier analysis of the propagating waves in Section 3.1.4. The fabrication and alignment errors of the grating also contribute to the experimental error.

3.1.4 Full wave simulations

We determine the reflection and transmission coefficients for each incident case using Fourier analysis of the total pressure field to compare the intensities of the incident and scattered wavevectors in reciprocal space. The measured and simulated pressure fields illustrate the wave-grating interaction for a particular incidence and are represented in reciprocal space by the corresponding wavevectors comprising the total pressure field. Due to the linearity of the grating, all of the acoustic energy lies on a circle of constant frequency with a radius equal to the magnitude of the incident wavevector. We note that the wavevectors with the highest intensities correspond to the incident and scattered signals,

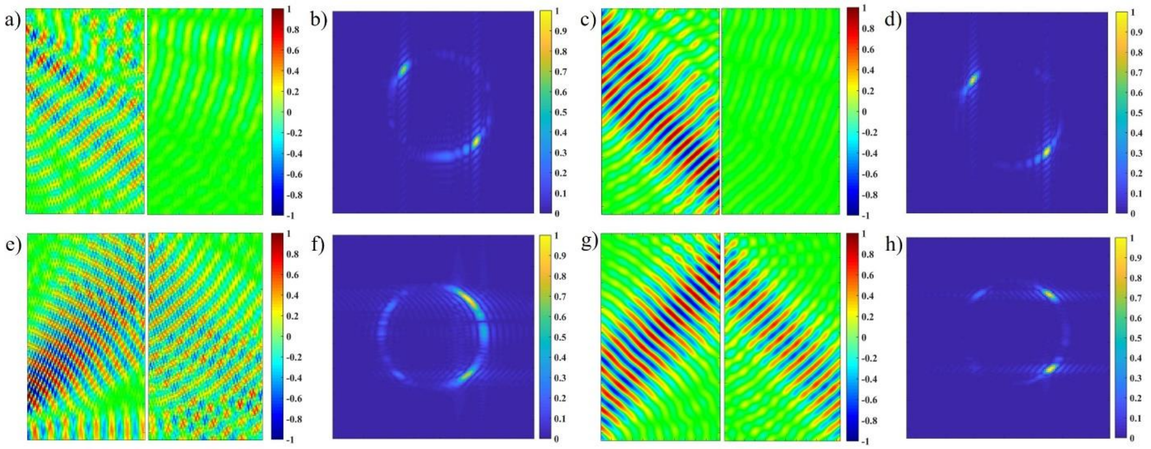

Figure 3.4: Fourier analysis of the wave-grating interaction for the 45-degree transmission experiment and full-wave simulation results (a) Measured pressure field for the transmission grating having -45-degree incidence and reflection directed back towards the source. (b) two-dimensional Fourier transform of (a) with the expected wavevectors having the highest intensities. (c) Simulated pressure field for -45-degree incidence case. (d) two-dimensional Fourier transform of (c) with wavevectors having peak intensities matching (b). (e) Measured pressure field for 45-degree incidence and -45-degree transmission. (f) Fourier transform of the measured pressure field in (e) illustrating expected wavevector locations in reciprocal space. (g) Simulated pressure field for 45-degree incidence. (h) Two-dimensional Fourier transform of (g) with wavevectors having peak intensities matching (f).

with the weaker intensities representing unwanted scattering. The transmission and reflection coefficients of the grating determine the overall scattering efficiency being sought to maximize and is determined by the ratio of incident intensity to the reflected or transmitted intensity in reciprocal space. The measured and simulated pressure fields of the transmission grating having -45-degree incidence and retroreflection is illustrated in Figs. 3.4a and 3.4c respectively. The two-dimensional Fourier transform of these fields reveal the incident and scattering wavevectors in reciprocal space (Figs. 3.4b and 3.4d) and are compared to yield a reflection coefficient R = 0.72 and 0.95 for the experiment and simulation respectively. The alternative case with 45-degree incidence and -45-degree transmission (Figs. 3.4e and 3.4g) results in an experimental and simulated transmission T

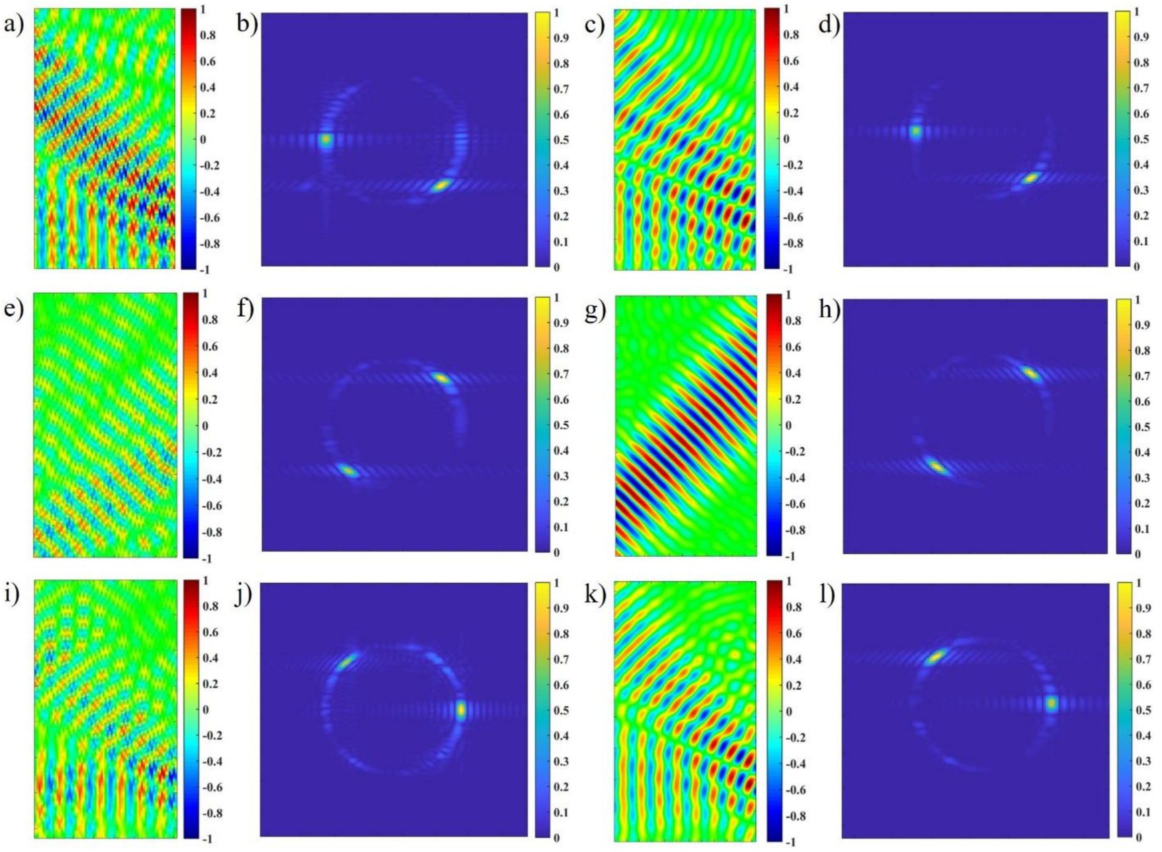

Figure 3.5: Fourier analysis of the wave-grating interaction for the 45-degree reflection experiment and full-wave simulation results (a) Measured pressure field for the reflection grating having a -45-degree incidence and normal reflection. (b) Two-dimensional Fourier transform of (a) with the expected wavevectors having the highest intensity values. (c) Simulated pressure field for -45-degree incidence. (d) Two-dimensional Fourier transform of (c) with wavevectors having peak intensities matching (b). (e) Measured pressure field for 45-degree incidence with reflection directed back towards the source. (f) Fourier transform of the measured pressure field in (e) having peak intensities matching the expected wavevectors. (g) Simulated pressure field for 45-degree incidence. (h) Two-dimensional Fourier transform of (g) with wavevectors having peak intensities matching (f). (i) Measured pressure field for normal incidence with a 135-degree reflection. (j) Two-dimensional Fourier transform of (i) having peak intensities at expected wavevector locations. (k) Simulation of normal incidence case. (l) Two-dimensional Fourier transform of (k) having wavevectors matching (j).

= 0.78 and 0.96 respectively, determined by the previously detailed wavevector analysis (Figs. 3.4f and 3.4h). The high simulation transmission and reflection coefficients indicate near perfect scattering efficiencies. The determined experimental coefficients are reduced due to the excitation of unwanted planewaves from the imperfect source as well as the open boundary at edge of the waveguide as seen in the reciprocal space of the pressure field.

To determine the scattering efficiency of the reflection grating, an identical wavevector analysis of reciprocal space is performed on a two-dimensional Fourier transform of the total pressure field. For an acoustic signal having -45-degree incidence and normal reflection (Figs. 3.5a and 3.5c), the intensities of the incident and scattered wavevectors in reciprocal space (Figs. 3.5b and 3.5d) are directly compared to determine experimental and simulated reflection coefficients R = 0.88 and 0.94 respectively. Alternatively, a 45-degree incident signal reflecting directly back towards the source (Figs. 3.5e and 3.5g) resulted in a reflection coefficient R = 0.84 and 0.99 for experimentation and simulation respectively (Figs. 3.5f and 3.5h). Observing the pressure field resulted from normal incidence and 135-degree reflection (Figs. 3.5i and 3.5k) yielded R = 0.76 and 0.97 for experimentation and simulation respectively using the established wavevector analysis in reciprocal space (Figs. 3.5j and 3.5l). Similar to the transmission simulations, the reflection simulations demonstrate near perfect scattering efficiencies as indicated by the reflection coefficients. However, the experimental reflection coefficients are lower due to the unwanted wavevector excitations from the imperfect source and open boundaries at the edge of the waveguide illustrated in reciprocal space as the non-zero wavevector intensities not localized to either the incident or scattered signals.

3.1.5 Determining the scatterer geometries

We design a grating with near perfect scattering efficiency by optimizing the unit cell geometry within a defined periodicity using a finite element method and Fourier analysis. To define the grating periodicity, we refer to the grating equation for normal reflection

$$d = \frac{m\lambda}{sin(\theta)}, \tag{3.2}$$

where d represents the periodicity, m is the diffraction order, λ the wavelength, and θ the angle of incidence. The only constraints in place are the grating periodicity and asymmetry required to invoke the asymmetric scattering. Thus, we seek to study the simplest structure possible following these constraints while minimizing the spatial resolution. Each unit cell is determined to be two rectangular structures of differing widths that equally divide the grating periodicity in three equal heights. A finite element program varies the respective widths of each section, iterating different unit cell geometries to study the wave-grating interaction for the selected scattering angle. We determine the maximum scattering efficiency for the desired wavevectors by performing a two-dimensional Fourier transform of the resulted pressure fields and compare the intensities of the incident and scattered wavevectors in reciprocal space. The unit cell geometry with the highest efficiency is selected, and the iterative process is repeated to optimize the scatterer heights while maintaining the grating periodicity.

3.1.6 Bianisotropic gratings for 35-degree incidence

We design a bianisotropic transmission grating with a 6 kHz working frequency and 35-degree transmission or retroreflection by analyzing the required wave-grating interaction needed to produce the desired asymmetric scattering. The difference of the

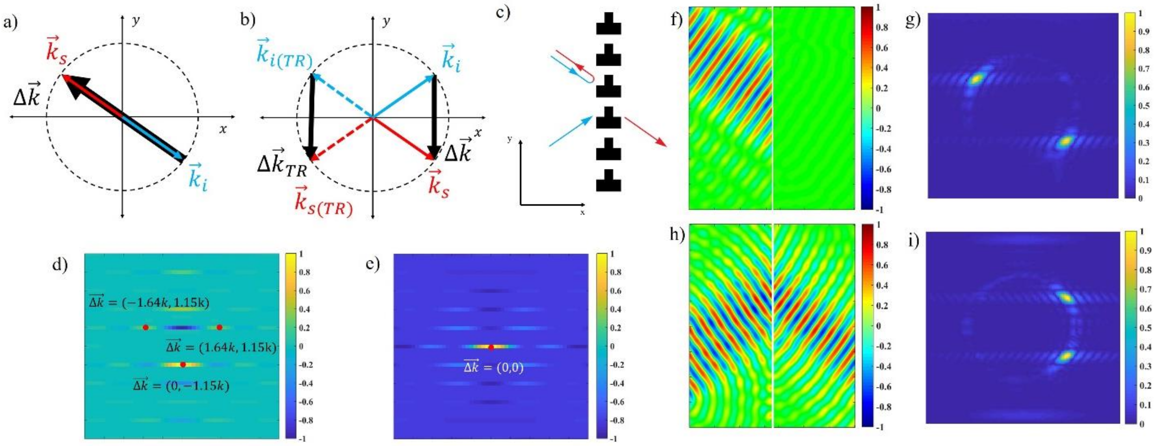

Figure 3.6: Wavevector analysis for the 35-degree transmission grating and full-wave simulation results (a) Wave-grating interaction for the transmission grating having -35-degree incidence and 145-degree reflection in reciprocal space, allowing for the determination of the required grating Bloch wavevector. (b) Wave-grating interaction for 35-degree incidence as well as the time reversed case represented by the dashed lines. For both (a) and (b), the incident, scattered, and Bloch wavevectors are represented by $\vec{k}_i$, $\vec{k}_s$ and Δk, respectively. (c) Bianisotropic grating structure with asymmetric wave scattering in (a) and (b) determined by inverse Fourier analysis of the incident and scattered wavevectors. (d) Real component of the two-dimensional spatial Fourier transform of the grating geometry with the expected Bloch wavevectors having the highest intensity. (e) Imaginary component of the two-dimensional spatial Fourier transform of the grating geometry having a zero vector. (f) Simulated pressure field of a -35-degree incident signal interacting with the bianisotropic transmission grating. (g) two-dimensional Fourier transform of (f) with wavevectors having peak intensities matching the desired scattering in (a). (h) Simulated pressure field of a 35-degree incident signal interacting with the bianisotropic transmission grating. (i) Two-dimensional Fourier transform of (h) with wavevectors having peak intensities matching the desired scattering in (b).

incident and scattered signals in reciprocal space determine the Bloch wavevectors required by the grating. In the case of retroreflection from -35-degree incidence requires a Bloch wavevector of (-1.64*k*, 1.15*k*) as illustrated in Fig. 3.6a. On the other hand, transmission of a 35-degree incident signal requires a Bloch wavevector (0, -1.15*k*) shown in Fig. 3.6b in addition to an identical Bloch wavevector for its time reversal case. Knowing this wave-grating interaction, we design a grating with 49.8 mm periodicity from Equation 3.2. A finite element method iterates the possible unit cell designs to determine the grating geometry as Fourier analysis is performed to maximize the scattering efficiency. Each scatterer consists of the two rectangular blocks vertically adjacent to one another, one having a 39 mm width and 18.5 mm height directly underneath a centered second block having 13 mm width and 16.5 mm height (Fig. 3.6c). The real component of a spatial two-dimensional Fourier transform of the scatterer geometries reveal the structure's intrinsic Bloch wavevectors (Fig. 3.6d) match Figs. 3.6a and 3.6b while the imaginary part of the transform has a non-interacting zero vector (Fig. 3.6e). The simulated pressure field for the bianisotropic transmission geometry having -35-degree incidence and retroreflection (Fig. 3.6f) yields a reflection coefficient R = 0.97 when the intensities of the incident and scattered wavevectors are compared in reciprocal space (Fig. 3.6g). Alternatively, the simulated field of the grating having 35-degree incidence and -35-degree transmission (Fig. 3.6h) yields a reflection coefficient R = 0.97 by Fourier analysis (Fig. 3.6i).

The design of the bianisotropic reflection grating with an identical working frequency and interacting with normal or 35-degree incident signals follows a similar process detailed by the transmission grating. The grating's Bloch wavevectors are determined by the difference of incident and scattered signals in reciprocal space illustrated in Figs. 3.7a and 3.7b. A 35-degree incident signal with a direct reflection back towards the source yields a Bloch wavevector (-1.64k, 1.15k) while the normal incident and its time reversal case require a Bloch wavevector of (-1.82k, 0.57k). The grating's dependence on the incident angle leads to a 99.6 mm periodicity determined by Equation 3.2. Iterating over many unit cell geometries to determine the unit cell with the maximum scattering efficiency yields the structures with the Bloch wavevectors in Figs. 3.7a and 3.7b. The

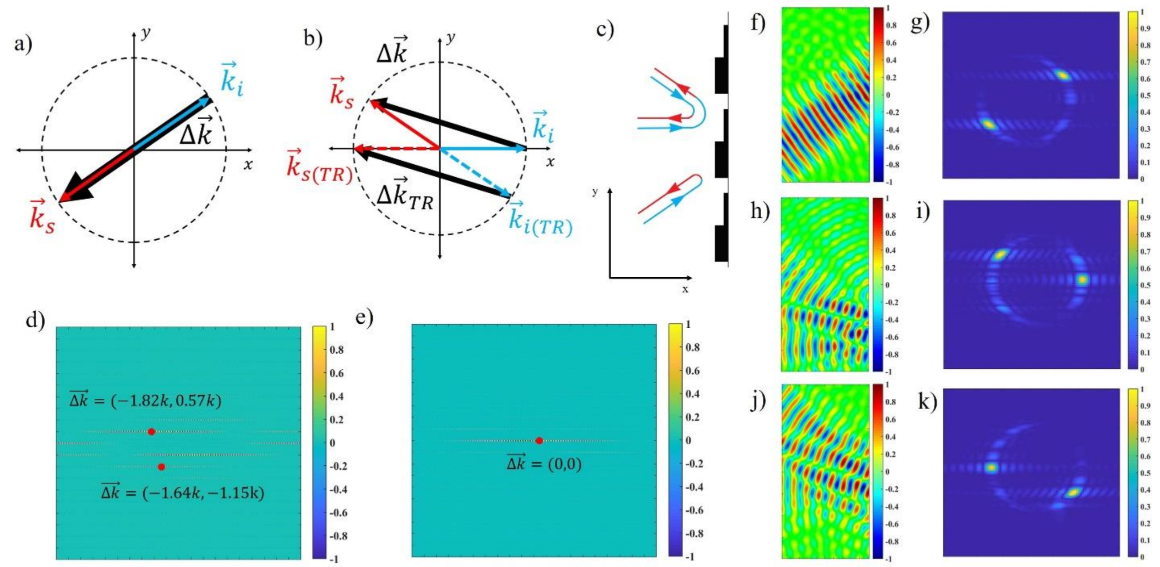

Figure 3.7: Wavevector analysis for the 35-degree reflection grating and full-wave simulation results (a) Wave-grating interaction for the reflection case for 35-degree incidence in reciprocal space and corresponding grating Bloch wavevector. (b) Wave-grating interaction for normal incidence as well as the time reversed case represented by the dashed lines. For both (a) and (b), the incident, scattered, and Bloch wavevectors are represented by $\vec{k}_i$, $\vec{k}_s$ and Δk, respectively. (c) Bianisotropic grating structure with asymmetric wave scattering in (a) and (b) determined by a finite element program to maximize the grating efficiency. (d) Real component of a two-dimensional spatial Fourier transform of the grating geometry with the expected scattering wavevectors having the highest intensity to the left of the inversion symmetry about the y-axis (e) Imaginary component of the two-dimensional spatial Fourier transform of the grating geometry having a zero vector. (f) Simulated pressure field of a 35-degree incident signal interacting with the bianisotropic reflection grating (g) Two-dimensional Fourier transform of (f) with wavevectors having peak intensities matching the desired scattering in (a). (h) Simulated pressure field of a normally incident signal interacting with the bianisotropic transmission grating. (i) Two-dimensional Fourier transform of (h) with wavevectors having peak intensities matching the desired scattering in (b). (j) Pressure field of a -35-degree incident signal and normal reflection after interacting with the grating. (k) Two-dimensional Fourier transform of (j) with wavevectors having peak intensities matching the desired scattering in the time reversal incidence in (b).

scatterer geometry is comprised of a rectangular block having a 41 mm height and 15.6 mm width directly underneath a second block having a 39 mm height and 5.1 mm width (Fig. 3.7c). The real part of a spatial two-dimensional Fourier transform of the geometries reveals the grating Bloch wavevectors (Fig. 3.7d) match Figs. 3.7a and 3.7b while the imaginary part of the transform continues to be a non-interacting zero vector (Fig. 3.7e). Full wave simulations of the finalized geometries yield a pressure field having 35-degree incidence and retroreflection (Fig. 3.7f) with reflection coefficient R = 0.97 after the previously described wavevector analysis is carried out (Fig. 3.7g). For the other incidence case having normal incidence and 145-degree reflection, the total pressure field is plotted in Fig. 3.7h with a reflection coefficient R = 0.95 from Fourier analysis (Fig. 3.7i). Time reversal of this incidence yields a pressure field illustrated in Fig. 3.7j with its reciprocal space in Fig. 3.7k having a reflection coefficient R = 0.97.

3.1.7 Bianisotropic gratings for 70-degree incidence

Further validating the design process, we simulate the transmission and reflection gratings interacting with 70-degree incidence. The bianisotropic transmission grating with Bloch wavevectors (-0.68*k*, 1.88*k*) and (0, -1.88*k*) shown in Figs. 3.8a and 3.8b is designed with 30.4 mm periodicity from Equation 3.2. Iterating the possible unit cell designs with a finite element method and analyzing the two-dimensional Fourier transform of the resulted pressure field determines the ideal grating geometry for maximum scattering efficiency. Each scatterer consists of the two rectangular blocks vertically adjacent to one another, one having 40.8 mm width and 6.4 mm height directly underneath a second centered block having 30 mm width and 14.2 mm height illustrated in Fig. 3.8c. The spatial two-dimensional Fourier transform of the grating structures have a real component matching the determined Bloch wavevectors in Figs. 3.8a and 3.8b and a non-interacting zero vector representing the imaginary part of the transform (Figs. 3.8d and 3.8e). The full wave simulations of the determined grating structures are plotted for each incident case,

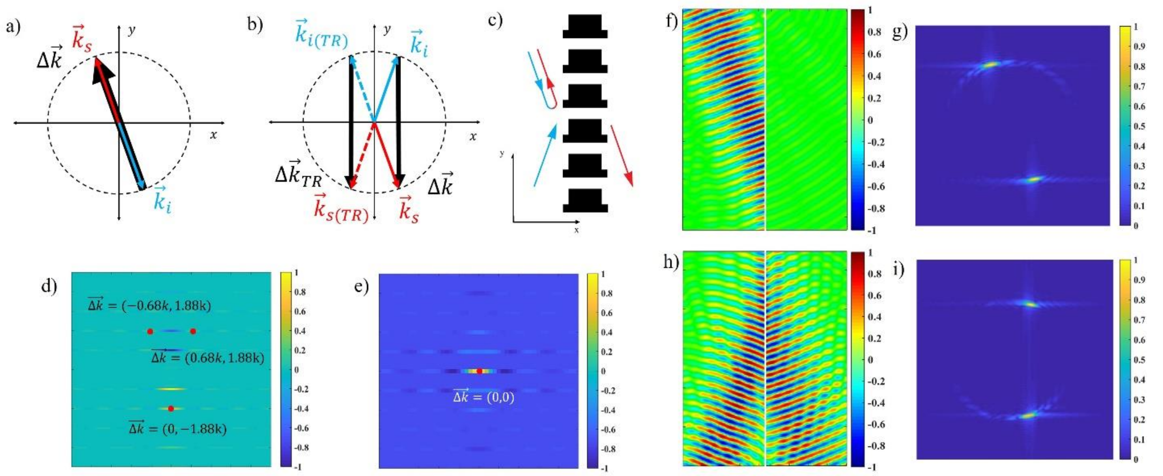

Figure 3.8: Wavevector analysis for the 70-degree transmission grating and full-wave simulation results (a) Wave-grating interaction for the reflection case for -70-degree incidence in reciprocal space and corresponding grating Bloch wavevector. (b) Wave-grating interaction for 70-degree incidence as well as the time reversed case represented by the dashed lines. For both (a) and (b), the incident, scattered, and Bloch wavevectors are represented by $\vec{k}_i$, $\vec{k}_s$ and Δk, respectively. (c) Bianisotropic grating structure with asymmetric wave scattering in (a) and (b) determined by inverse Fourier analysis of the incident and scattered wavevectors. (d) two-dimensional spatial Fourier transform of the grating geometry with the expected Bloch wavevectors having the highest intensity. (e) Imaginary component of the two-dimensional spatial Fourier transform of the grating geometry having a zero vector. (f) Simulated pressure field of a -70-degree incident signal interacting with the bianisotropic transmission grating (g) Two-dimensional Fourier transform of (f) with wavevectors having peak intensities matching the desired scattering in (a). (h) Simulated pressure field of a 70-degree incident signal interacting with the bianisotropic transmission grating. (i) Two-dimensional Fourier transform of (h) with wavevectors having peak intensities matching the desired scattering in (b).

beginning with a signal having -70-degree incidence and direct reflection back towards the source (Fig. 3.8f). Comparing the incident and scattered wavevectors in reciprocal space yields a reflection coefficient R = 0.94 (Fig. 3.8g). Looking at a signal having 70-degree incidence and -70-degree transmission, results in a pressure field illustrated by Fig. 3.8h with a transmission coefficient T = 0.95 evaluated from two-dimensional Fourier analysis.

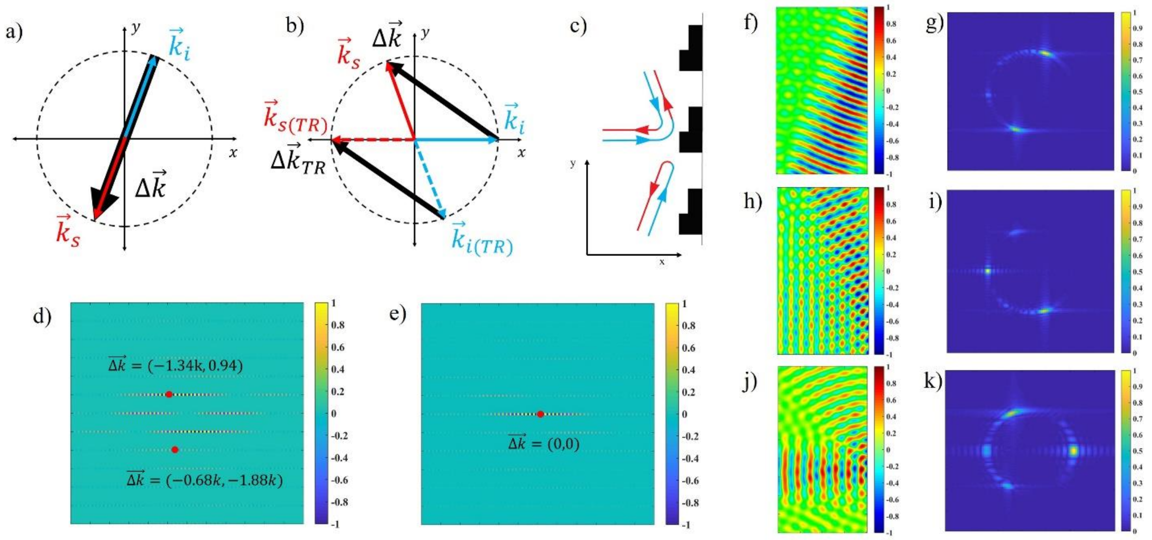

Figure 3.9: Wavevector analysis for the 70-degree reflection grating and full-wave simulation results (a) Wave-grating interaction for the reflection case with 70-degree incidence in reciprocal space and corresponding grating Bloch wavevector. (b) Wave-grating interaction for normal incidence as well as the time reversed case represented by the dashed lines. For both (a) and (b), the incident, scattered, and Bloch wavevectors are represented by $\vec{k}_i$, $\vec{k}_s$ and Δk, respectively. (c) Bianisotropic grating structure with asymmetric wave scattering in (a) and (b) determined by a finite element program to maximize the grating efficiency. (d) Real component of a two-dimensional spatial Fourier transform of the grating geometry with the expected scattering wavevectors having the highest intensity to the left of the inversion symmetry about the y-axis (e) Imaginary component of the two-dimensional spatial Fourier transform of the grating geometry having a zero vector. (f) Simulated pressure field of a 70-degree incident signal interacting with the bianisotropic reflection grating (g) two-dimensional Fourier transform of (f) with wavevectors having peak intensities matching the desired scattering in (a). (h) Simulated pressure field of a normally incident signal interacting with the bianisotropic transmission grating. (i) two-dimensional Fourier transform of (h) with wavevectors having peak intensities matching the desired scattering in (b). (j) Pressure field of a -70-degree incident signal and normal reflection after interacting with the grating. (k) two-dimensional Fourier transform of (j) with wavevectors having peak intensities matching the desired scattering in the time reversal incidence in (b).

Proceeding to the bianisotropic grating design tailored to interact with waves having 70-degree or normal incidence, we design a grating with 60.8 mm periodicity determined by Equation 3.2. To realize the desired asymmetric scattering, we determine the grating's Bloch wavevectors as (-0.68*k*, -1.88*k*) and (-1.34*k*, 0.94*k*) illustrated in Figs. 3.9a and 3.9b respectively. We iterate over many possible geometries using a finite element program to determine the maximum grating efficiency using two-dimensional Fourier analysis. The resulting geometries are comprised of a rectangular structure with 16.7 mm width and 15.3 mm height directly underneath a second rectangle having 10.2 mm width and 18.2 mm height illustrated in Fig. 3.9c. The real component of a spatial two-dimensional Fourier analysis of the resulting structures yield Bloch wavevectors matching those determined in Figs. 3.9a and 3.9b, and a zero vector in the imaginary component not interacting with the grating (Figs. 3.9d and 3.9e). A 70-degree incident signal interacts with the grating resulting with a direct reflection back towards the source (Fig. 3.9f) with reciprocal space illustrated in Fig. 3.9g yielding a reflection coefficient R = 0.95. The pressure filed having normal incidence and 120-degree reflection is illustrated in Fig. 3.9h with reciprocal space in Fig. 3.9i yielding a reflection coefficient R = 0.95 while the pressure field of its time reversal case is illustrated in Fig. 3.9j with reflection coefficient R = 0.97 determined from evaluation of its reciprocal space in Fig. 3.9k.

A two-dimensional spatial Fourier transform of the resulting geometries for each grating design revealed the desired Bloch wavevectors in reciprocal space for only in the real part of the transform. The imaginary part of each Fourier transform yielded a zero-vector that does not interact with the incident wave. Fig. 3.10a illustrates the zero vector of the bianisotropic transmission grating that interacts with signals having 45-degree incidence while Fig. 3.10b illustrates a zero vector for the 45-degree reflection grating.

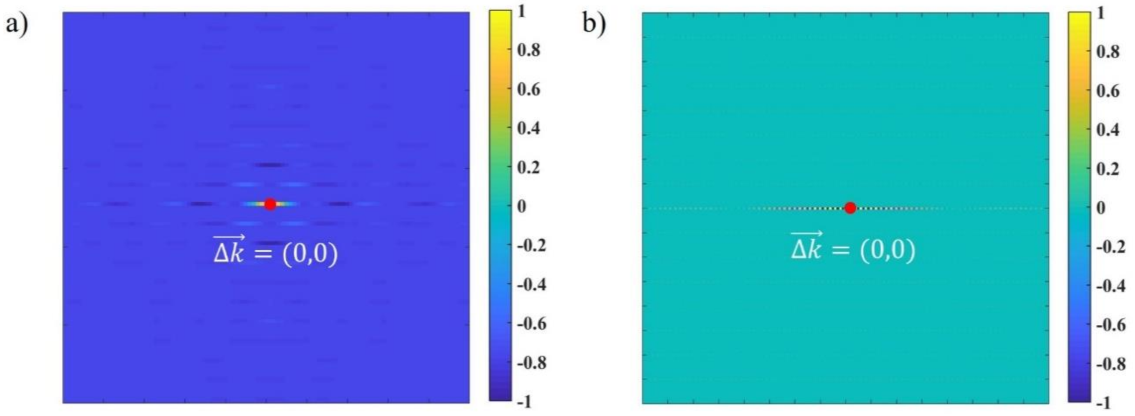

Figure 3.10: Imaginary Fourier component of the 45-degree bianisotropic grating (a) Imaginary component of a two-dimensional spatial Fourier transform of the transmission grating geometries indicating no interaction with incident signal. (b) Imaginary component of a two-dimensional spatial Fourier transform of the reflection grating geometries

3.2 Willis coupling enabling extreme effective material properties

3.2.1 Introduction

Acoustic metamaterial research aims to develop artificial materials with effective material properties that go beyond what is found in nature to enable superior control over sound wave propagation for applications in biomedical imaging [22,23,41-44], noise control [104-107], and cloaking technologies [15,108-112]. Passive metamaterials demonstrate these exotic effective material properties, but their lossy behavior, narrow bandwidth, and lack of tunability limits their effectiveness for practical applications [2]. Active metamaterials use electric circuits to compensate for these disadvantages [11,52]. These circuits are highly tunable and can be adjusted in real time to allow reconfigurable focusing and beam steering [13]. Simple alterations of the active circuitry modulate the effective material properties of the unit cell to achieve negative effective densities and bulk moduli [18,19].

While existing active metamaterials overcome many disadvantages of their passive counterparts, they were all based on local resonance that limit the available effective parameter range, making them unsuitable for applications that require extreme effective densities and/or bulk moduli such as transformation acoustics-based cloaking [15,58,111], wave steering with extreme angles [100], and ultrathin sound isolators [102]. In this section, we propose an active metamaterial with strong Willis coupling to dramatically broaden the accessible range of the effective density and bulk modulus by at least two orders of magnitude compared to that of a non-Willis active metamaterial with a symmetric control circuit. Willis coupling, analogous to bianisotropy in electromagnetics, is a cross-coupling of the pressure and local particle velocity fields that couples the monopolar and dipolar responses of metamaterial unit cells [95,113-116]. These coupled responses result in asymmetric wave propagation to realize ultrathin nonreciprocal sound isolators, abnormal acoustic metagratings with high efficiency, and decorated membranes with large Willis coupling [20,117-119]. Additionally, passive acoustic scatterers with maximum Willis coupling overcome inherent efficiency limitations of conventional metasurfaces for arbitrary wavefront manipulation [98]. Besides fluid media that only support longitudinal waves, Willis coupling metamaterials were used to achieve asymmetric shear wave and asymmetric longitudinal wave propagation in elastic media [120]. PT-symmetric acoustics is an alternative method that enables asymmetric wave scattering by pairing materials with acoustic gain and loss properties [52,121,122]. Active Willis coupled metamaterials are also used to study virtualized unit cells for non-reciprocal, non-Hermitian, and topological systems [19,123,124]. It is worth noting that asymmetric wave propagation is not the focus of this section. In general, Willis coupling is qualitatively understood as two different types of coupling mechanisms [95]. The first, known as even coupling, is present when the geometric center and center of mass are offset, such that any resultant motion from an external force is a combination of the monopolar and dipolar responses [95]. The even coupling purely depends on the local properties of the metamaterial and has no reliance on the incident wave. The second, known as odd coupling, exhibits non-local effects due to its dependence on the incident wavevector [95]. It is difficult to distinguish the local or non-local behavior in Willis metamaterials, but the presence of Willis coupling extends the range of effective density and bulk modulus [125,126].

3.2.2 Modeling

We model the wave scattering of an active acoustic metamaterial with Willis coupling by decomposing the total acoustic response of the unit cell into its passive and active components as

$$R_{tot} = R_{pass} + R_{act}, \tag{3.3}$$

$$T_{tot} = T_{pass} + T_{act}, \tag{3.4}$$

where R_{tot} and T_{tot}, R_{pass} and T_{pass}, and R_{act} and T_{act} are the total, passive, and active acoustic reflection and transmission coefficients, respectively. In this section, we implement a similar passive structure consisting of an air layer (light purple part in Fig. 3.11a) sandwiched by two piezoelectric transducers (purple parts in Fig. 3.11a) and acoustic sensors (gold parts in Fig. 3.11a) used in [18]. The passive reflection and

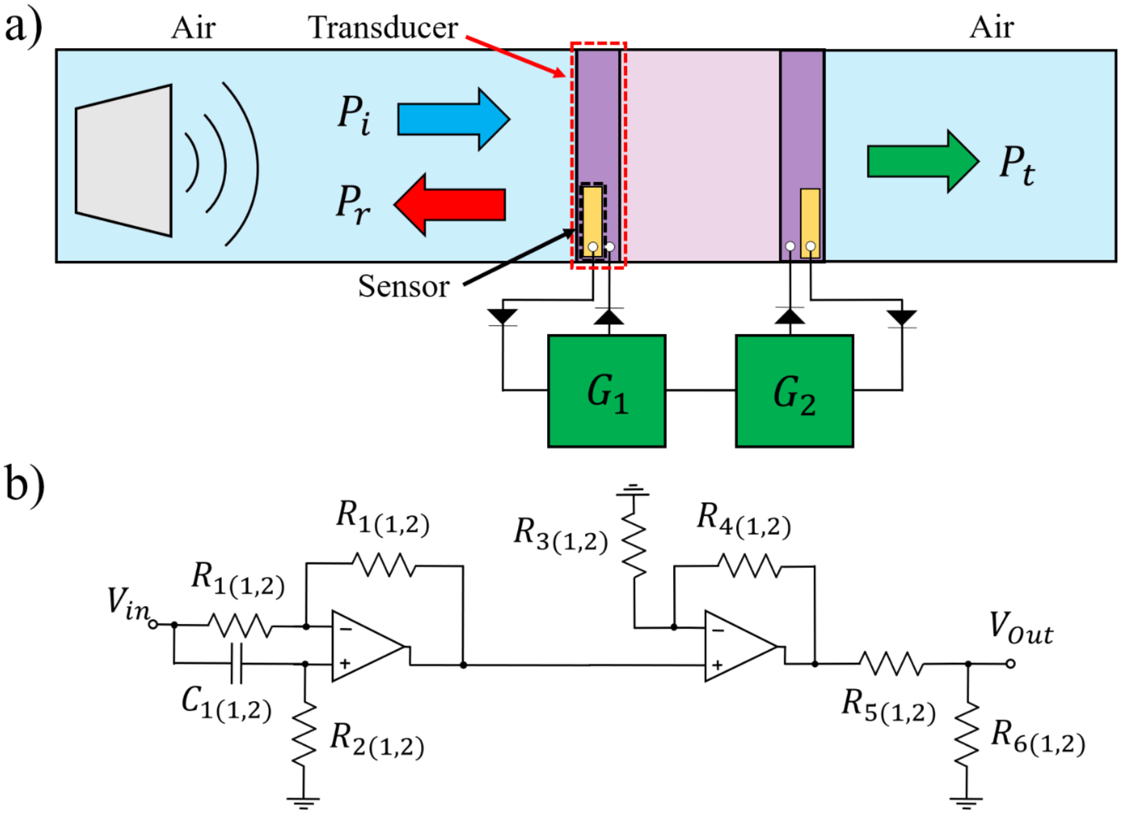

Fig. 3.11: Designed unit cell with active feedback control with Willis coupling when $G_1 \neq G_2$. (a) One-dimensional representation of the metamaterial confined in a waveguide with the active sensor-transducer pairs connected to the feedback control circuits (b) Active circuitry comprising each gain function for independent control of the phase and amplitude of G_1 and G_2. (1,2) in the subscripts of the circuit components denote the resistance or capacitance values for G_1 and G_2, respectively.

transmission coefficients were measured in [18] using a one-dimensional waveguide with rectangular cross-section when the active circuit components were off. We can control the total acoustic response of the metamaterial by modulating the active response. Our design introduces active control with two sensor-transducer pairs on both sides of the proposed unit cell to detect incident waves and superimpose an active acoustic signal through asymmetric feedback control circuits on the passive acoustic response of the structure (Fig. 3.11a). Note that the one-dimensional waveguide has hard-wall boundary conditions on the boundaries in parallel to the wave propagation that serve as perfectly reflecting/mirror boundaries and span the single unit cell effectively into a two-dimensional array. Given this setup, the active acoustic outputs are [18]

$$R_{L_{act}} = \frac{h_i h_{ro} G_1}{1 - h_{io} G_1}, \tag{3.5}$$

$$R_{R_{act}} = \frac{h_i h_{ro} G_2}{1 - h_{io} G_2}, \tag{3.6}$$

$$T_{act} = \frac{h_i h_{ro} G_1}{1 - h_{io} G_1} \cdot \frac{h_i h_{to} G_2}{1 - h_{io} G_2}, \tag{3.7}$$

where G_1 and G_2 are the gain functions of the feedback circuit, $R_{R_{act}}$ and $R_{L_{act}}$ are the active acoustic reflection coefficients when an incident wave propagates from the right and left respectively, h_i is the efficiency that converts a measured input pressure to an input voltage by the sensors, h_{io} is the ratio between the voltage sent out from the driving transducer and the detected voltage received by the sensor, h_{ro} is the efficiency that converts an output voltage to output active reflected pressure, and h_{to} is the efficiency that converts an output voltage to output active transmitted pressure. Since the sensor-transducer pairs are identical, the efficiency terms satisfy the condition $h_{ro} = h_{to}$. These efficiency terms fully characterize the coupling between the mechanical and electrical components in the metamaterial as they quantify the voltage to pressure and voltage to voltage conversions that occur in the active feedback loops. The efficiency terms can be measured following the procedure in [18]. For our numerical models, we use the experimentally determined passive material parameters and efficiency terms obtained in [18]. Based on Equations 3.5-3.7, the active transmission and reflection of the metamaterial can be directly controlled by the gain functions G_1 and G_2. These gain functions can be realized by the active circuits shown in Fig. 3.11b. The resistance and capacitance values of the active circuitry that are required to achieve the desired G_1 and G_2 are calculated in section 3.2.4.

Independent control of the gain functions G_1 and G_2 allows for the realization of unit cells with or without Willis coupling. In acoustics, Willis coupling is the cross-coupling of the pressure and local particle velocity fields, which appears in the constitutive relations as [95,96]

$$\mu = \rho v + \tilde{\psi}\frac{\partial \varepsilon}{\partial t}, \tag{3.8}$$

$$-p = \kappa\varepsilon + \psi\frac{\partial v}{\partial t}, \tag{3.9}$$

where μ is the momentum density, ρ is the mass density, v is the particle velocity, ε is the volume strain, p is the acoustic pressure, κ is the bulk modulus, and $\tilde{\psi}$ and ψ are the Willis coupling coefficients. The Willis coupling coefficients are proportional to an asymmetry coefficient $W = \psi\omega/Z$, where Z is the characteristic impedance [96]. This asymmetry coefficient modifies the specific acoustic impedances $Z_{sp}^{\pm} = Z(1 \pm iW)$, where the positive/negative sign indicates the wave propagation in the forward/backward direction. W can be calculated by the asymmetric acoustic reflection coefficients from the left R_L and from the right R_R and the transmission coefficient T as

$$W = \pm\frac{R_L - R_R}{i\sqrt{(1 - R_L R_R + T^2)^2 - 4T^2}}, \tag{3.10}$$

where R_L, R_R, and T are calculated by substituting Equations 3.5-3.7 into Equations 3.3 and 3.4. This equation indicates that Willis coupling is present with asymmetric acoustic reflection [96]. Equations 3.5 and 3.6 illustrate that the introduction of unequal gain functions G_1 and G_2 result in asymmetric acoustic reflections and, by extension, Willis coupling. Alternatively, this implies that non-Willis media require the gain functions to satisfy $G_1 = G_2$. This non-Willis gain function condition ensures symmetric feedback control circuits and equal reflection coefficients for an acoustic signal incident on either side of the metamaterial.

To determine the effective properties of the active unit cell with Willis coupling for the calculation of accessible material parameter range, we use a generalized parameter retrieval method based on the reflection coefficients R_L and R_R, the transmission coefficient T, and the passive length of the unit cell derived in [96].

3.2.3 Results

We retrieve the effective density and bulk modulus of a unit cell with and without Willis coupling for $G_1 = 2e^{i(0.87)}$ to investigate the effect of Willis coupling on the effective density and bulk modulus from 2.00-3.00 kHz. As previously mentioned, our model uses the efficiency terms and passive material parameters from [18] with $\rho_{pass} = (15 - 4i)\rho_{air}$ and $\kappa_{pass} = (1.15 - 0.3i)\kappa_{air}$, as well as a material thickness $d = 5mm$ and air as the background medium ($\rho_{air} = 1.225\frac{kg}{m^3}$ and $\kappa_{air} = 1.41 \times 10^5 Pa$). Figure 3.12a shows the arithmetic mean of the imaginary part of the asymmetry coefficient, W, as a function of the amplitude and phase of G_2 near 2.50 kHz calculated from Equations 3.3-3.7 and 3.10. The arithmetic mean is given by the average value of Im(W) over 2.45 kHz to 2.55 kHz. The non-Willis case occurs when $G_1 = G_2 = 2e^{i(0.87)}$, and is achieved with the active circuitry in Fig. 3.11b. The complex effective density and bulk modulus

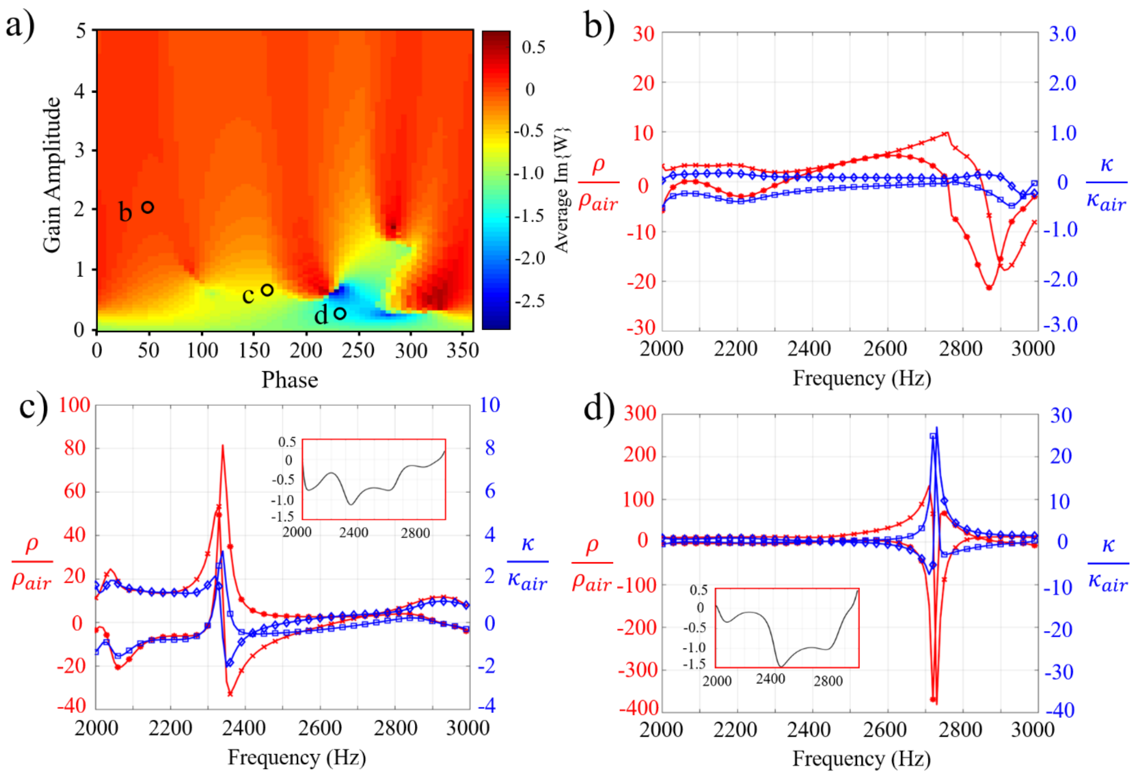

Fig. 3.12: Effects of Willis coupling on effective material parameters. (a) The arithmetic mean of the imaginary part of the asymmetry coefficient as a function of the amplitude and phase of G_2 near 2.50 kHz. The three marked points correspond to (b), (c), and (d), respectively. (b) The complex effective density and bulk modulus normalized to air without Willis coupling when $G_1 = G_2 = 2e^{i(0.87)}$. (c) The complex effective density and bulk modulus normalized to air with Willis coupling when $G_1 = 2e^{i(0.87)}$ and $G_2 = 0.6e^{i(2.79)}$. (d) The complex effective density and bulk modulus normalized to air with Willis coupling when $G_1 = 2e^{i(0.87)}$ and $G_2 = 0.15e^{i(4.10)}$. In (b) and (c), the blue diamond and blue square lines plot the real and imaginary bulk modulus, respectively and the red x and red star lines plot the real and imaginary density, respectively. The subplots in (c) and (d) display the corresponding asymmetry coefficient of the Willis coupled metamaterial from 2.00-3.00 kHz.

normalized to air of the non-Willis case exhibit frequency bands of negative effective density from 2.85-3.00 kHz and negative effective bulk modulus from 2.92-3.00 kHz (Fig. 3.12b). A Willis coupling case is achieved when $G_1 \neq G_2$, where we set $G_1 = 2e^{i(0.87)}$ and $G_2 = 0.6e^{i(2.79)}$. The selection of the amplitude and phase of G_2 for the Willis coupled metamaterial is based on the magnitude of the imaginary part of the asymmetry coefficient (Fig. 3.12a) that indicates a large change in the specific acoustic impedance. The complex effective density and bulk modulus normalized to air for this Willis coupling case exhibit a frequency band with negative effective density from 2.33-2.63 kHz and negative effective bulk modulus from 2.34-2.68 kHz (Fig. 3.12c). The effective density and bulk modulus achieve a larger magnitude when the imaginary part of the asymmetry coefficient is non-zero (Fig. 3.12c) comparing with the non-Willis coupling case. A second Willis coupling case sets $G_1 = 2e^{i(0.87)}$ and $G_2 = 0.15e^{i(4.10)}$. In this case, the selection of the amplitude and phase of G_2 for the Willis coupled metamaterial is based on the magnitude of the imaginary part of the asymmetry coefficient (Fig. 3.12a). The complex effective density and bulk modulus normalized to air for this Willis coupling case exhibit a frequency band with negative effective bulk modulus from 2.68-2.91 kHz (Fig. 3.12d). The magnitudes of the effective density and bulk modulus increase to even higher values when the imaginary part of the asymmetry coefficient increases its magnitude (Fig. 3.12d). These two Willis coupling cases suggest an expansion of the range of realizable effective material parameter magnitudes as compared to the non-Willis counterpart.

To determine the accessible parameter range of our active metamaterial with and without Willis coupling, we independently vary the phase of the gain functions G_1 and G_2 from $[0, 2\pi]$ and the amplitude of the gain functions G_1 and G_2 from $[0, 5]$ and retrieve the effective density and bulk modulus at 2.97 kHz. This frequency corresponds to the monopolar resonance of the non-Willis case when $G_1 = G_2 = 1$. This monopolar resonance will occur at other frequencies when the complex gain functions vary for the non-Willis case. Thus, the selection of frequency is not critical to our results. The active metamaterial without Willis coupling maintains a symmetric feedback circuit with $G_1 = G_2$, while the active metamaterial with Willis coupling has an asymmetric feedback circuit

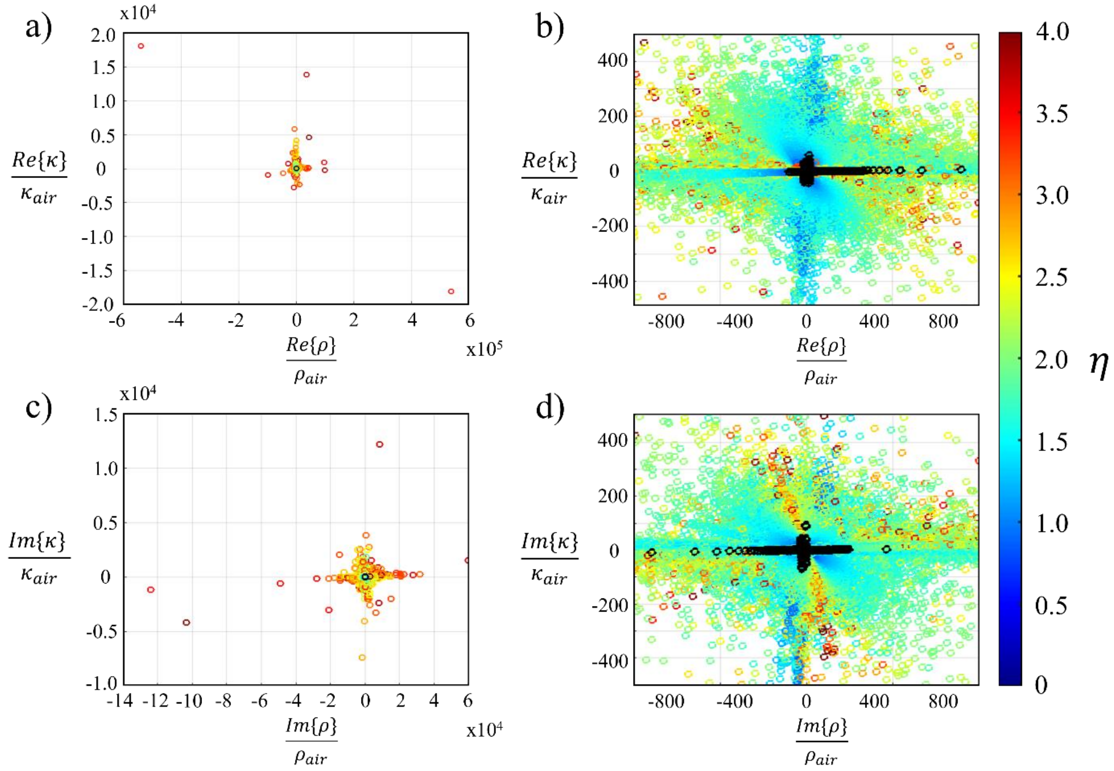

Fig. 3.13: Full effective parameter map of the complex density and bulk modulus for the active Willis coupled and non-Willis metamaterials. (a) Parameter map of the real part of the effective density and bulk modulus for the active metamaterial with and without Willis coupling. The real part of the effective density and bulk modulus are plotted on the horizontal and vertical axes, respectively. Additionally, the colored points and black points represent effective material parameters for Willis and non-Willis metamaterials, respectively. The color map quantifies the logarithm of the ratio of the imaginary part to the real part of the asymmetry coefficient, $\eta = \log_{10}(Abs(Im\{W\}/Re\{W\}))$. (b) Magnified window of (a) displaying a normalized density range of [-1000, 1000] and a normalized bulk modulus range of [-500, 500]. (c) Parameter map of the imaginary part of the effective density and bulk modulus for the active metamaterial with and without Willis coupling. The imaginary part of the effective density and bulk modulus are plotted on the horizontal and vertical axes, respectively. This subfigure has the same color scheme as (a). (d) Magnified window of (c) displaying a normalized density range of [-1000, 1000] and a normalized bulk modulus range of [-500, 500].

with $G_1 \neq G_2$. We discretize our parameter sweep of the two gain functions with step sizes of 0.005 and 10 degrees for the amplitude and phase changes over the proposed range. The full range of the real-valued effective material parameters are plotted in Fig. 3.13a with the effective density on the horizontal axis and effective bulk modulus on the vertical axis; the black and colored dots correspond to the retrieved material perimeters for the non-Willis and Willis coupling cases, respectively. In the most extreme cases, the available range of the real part of the effective density and bulk modulus with the active Willis coupled metamaterial spans three orders of magnitude beyond the effective parameter range of the non-Willis metamaterial, while the majority of densely clustered points surpass the non-Willis effective range by two orders of magnitude. The outermost points shown in Fig. 3.13a are due to the satisfaction of a resonance condition where the imaginary part of the asymmetry coefficient reaches a local maximum and the real part reaches a local minimum.

The effective density and bulk modulus of these outermost points are very sensitive to any circuit parameter variations. An extreme point in the fourth quadrant of Fig. 3.13a is achieved when $G_1 = 3.025e^{i(4.36)}$ and $G_2 = 2.12e^{i(2.18)}$ resulting in a normalized effective density and bulk modulus $Re(\rho) = 5.39 \times 10^5$ and $Re(\kappa) = -1.81 \times 10^4$. An extreme point in the third quadrant of Fig. 3.13c with the largest magnitude of the negative imaginary part of the effective density is achieved when $G_1 = 4.20e^{i(3.67)}$ and $G_2 = 2.095e^{i(3.84)}$ resulting in a normalized effective density and bulk modulus $Im(\rho) = -1.24 \times 10^5$ and $Im(\kappa) = -1.18x10^3$. While these extreme density and bulk modulus values are three orders higher than the non-Willis case, small variations in the resistance and capacitance values of the active circuits caused by typical manufacturing error results in significant drop (less than an order) to these extreme effective material parameter values.

For close inspection of the region of densely clustered points, we zoom in on the plot in Fig. 3.13a with the vertical and horizontal axes displaying a normalized density range of [-1000, 1000] and a normalized bulk modulus range of [-500, 500] (Fig. 3.13b). In this magnified window, all of the resultant parameter values from every possible non-Willis configuration are present. The full parameter range of the non-Willis configurations is completely covered by the Willis coupling cases' point density, indicating that the achievable effective density and bulk modulus of the non-Willis case is fully accessible by the active Willis coupled metamaterial. The real-valued effective density and bulk modulus range resulted from every active Willis coupled metamaterial drastically exceeds the non-Willis metamaterial parameter range by at least two orders of magnitude, both in the positive and negative directions. Similarly, we plot the full range and a magnified window of the imaginary part of the effective material parameters in Figs. 3.13c and 3.13d with the effective density on the horizontal axis and the effective bulk modulus on the vertical axis and the colored and black dots corresponding to the active metamaterial with and without Willis coupling, respectively. The available range of the imaginary parts of the effective density for the active metamaterial with Willis coupling spans about three orders of magnitude beyond the non-Willis metamaterial in the most extreme points, while the majority of points in Fig. 3.13c span two orders of magnitude beyond the non-Willis metamaterial. The imaginary part of the bulk modulus for the active metamaterial with Willis coupling spans one order of magnitude beyond the non-Willis metamaterial. Figure 3.13d zooms in on the plot of Fig. 3.13c to the same parameter range as Fig. 3.13b, where all of the resultant parameter values from every non-Willis configuration are present. Similarly, the imaginary part of the non-Willis parameters is fully accessible by the active Willis coupled metamaterial with a broader range and higher resolution. Thus, the accessible range of the imaginary part of the effective density and bulk modulus is much larger and denser with the active Willis coupled metamaterial as compared to the non-Willis metamaterial.

Each point in the Willis case with effective density and bulk modulus values that exceed the effective parameter range of the non-Willis case has a large imaginary part and a small real part of the asymmetry coefficient. Because of the asymmetric active components used in the metamaterial, the extreme effective material parameters result from the presence of Willis coupling. This dramatic effective parameter expansion is illustrated by the color map in Fig. 3.13, which shows the logarithim of the ratio of the imaginary part of the asymmetry coefficient to the real part of the asymmetry coefficient, η. The points with extreme effective parameter values have a much larger η than those within the vicinity of the non-Willis case (Fig. 3.13). This result indicates that the cause of the significant parameter range expansion is dominated by the imaginary part of the asymmetry coefficient.

To investigate the effect of the expanded accessible effective density and bulk modulus range on the wave propagation through the active metamaterial, we also calculate the effective refractive index and acoustic impedance normalized to air for our active metamaterial with and without Willis coupling at 2.97 kHz. The full range of the real parts of the effective refractive index and acoustic impedance are shown in Fig. 3.14a with the effective refractive index on the horizontal axis and effective acoustic impedance on the vertical axis. The black and colored dots correspond to the retrieved material parameters for the non-Willis and Willis coupling cases, respectively. While the available range of the real effective impedance ratio with Willis coupling spans three orders of magnitude more

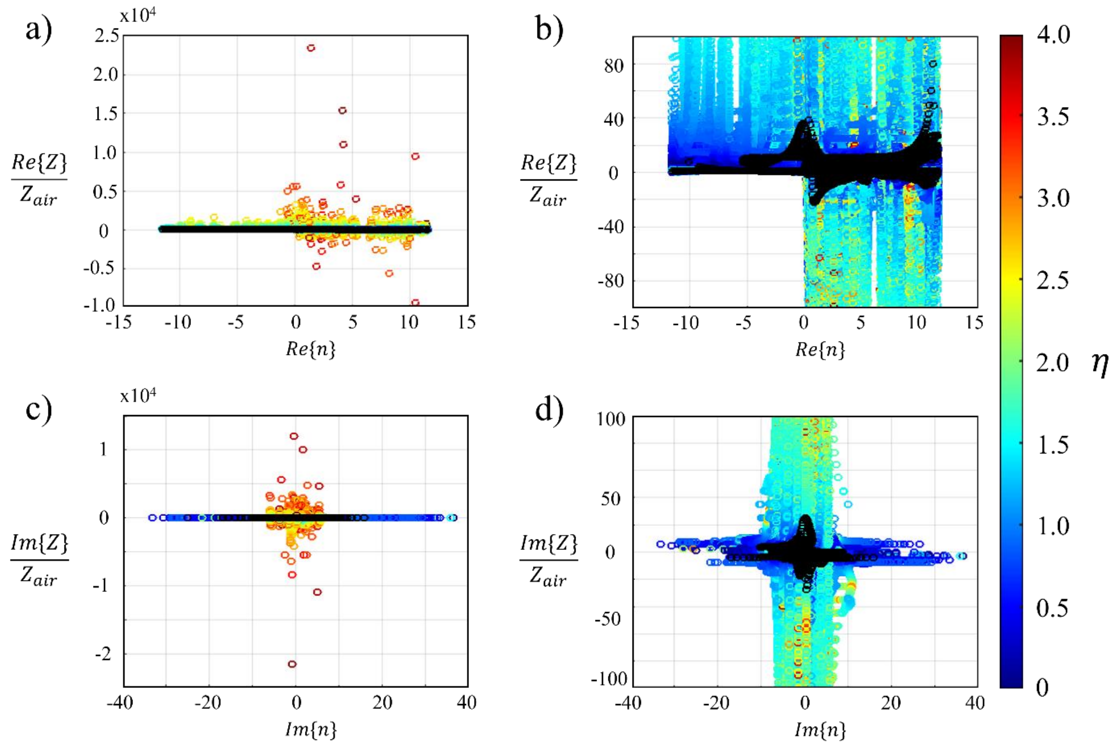

Fig. 3.14: Full parameter map of the complex effective refractive index and acoustic impedance normalized to air for the active Willis coupled and non-Willis metamaterials. (a) The real part of the effective refractive index and acoustic impedance for the active metamaterial with and without Willis coupling. The real part of the effective refractive index and acoustic impedance are plotted on the horizontal and vertical axes, respectively. Additionally, the colored points and black points represent effective material parameters for Willis and non-Willis metamaterials, respectively. The color map quantifies the logarithm of the ratio of the imaginary part to the real part of the asymmetry coefficient, $\eta = \log_{10}(Abs(Im\{W\}/\,Re\{W\}))$. (b) Magnified window of (a) displaying an acoustic impedance range of [-100, 100] (c) The imaginary part of the effective refractive index and acoustic impedance for the active metamaterial with and without Willis coupling. The imaginary part of the effective refractive index and acoustic impedance are plotted on the horizontal and vertical axes, respectively. This subfigure has the same color scheme as (a). (d) Magnified window of (c) displaying an acoustic impedance range of [-100, 100].

than the non-Willis cases in the most extreme points, the majority of densely clustered points span two orders of magnitude beyond the non-Willis case. The available range of the real part of the effective refractive index in both Willis and non-Willis cases are the same. The real part of the refractive index limits are identical due to the branch section of the arccosine function in the parameter retrieval method based on the deep subwavelength passive thickness of the metamaterial. A magnified window with the vertical axis displaying a normalized impedance of [-100, 100] (Fig. 3.14b) confirms that the range of the impedance of the active Willis coupled metamaterial dramatically exceeds the accessibility of the non-Willis cases. This three-order expansion of the acoustic impedance range (two orders for the denser points) aligns with the range expansion of the effective density and bulk modulus, because $Z = \sqrt{\rho\kappa}$. The larger range of the acoustic impedance can result in stronger impedance mismatch between the Willis coupled metamaterial and the background medium to form an ultrathin acoustic barrier with perfect sound isolation [117]. The lack of values in the double negative quadrant in Figs. 3.14a and 3.14b stems from the simultaneous negativity of the effective density, bulk modulus, and the resultant negative phase velocity c. By defining a characteristic impedance $Z = \rho c$ a negative density and phase velocity result in a positive acoustic impedance.

We show the full range and a magnified window of the imaginary part of the effective refractive index and acoustic impedance in Figs. 3.14c and 3.14d with the effective refractive index on the horizontal axis and the effective acoustic impedance on the vertical axis; the colored and black dots correspond to the active metamaterial with and without Willis coupling, respectively. The available range of the imaginary part of the effective acoustic impedance for the active metamaterial with Willis coupling spans about four orders of magnitude beyond its non-Willis counterpart in the most extreme cases. The majority of points in Fig. 3.14c that correspond to the Willis coupled metamaterial span two orders of magnitude beyond the points that correspond to the non-Willis case. The imaginary part of the refractive index for the Willis cases expands the range of the non-Willis cases by a factor of two. This broadened range of accessible points in the imaginary part of the refractive index implies an enhanced control of the acoustic loss and gain properties of the metamaterial. Figure 3.14d zooms in on the plot of Fig. 3.14c with the vertical axis displaying a normalized impedance of [-100, 100] to confirm that the range of the impedance for the active metamaterial with Willis coupling achieves high accessibility, dramatically extending beyond the range of the non-Willis metamaterial. Similar to the expanded range of the complex effective density and bulk modulus, the expanded range of the complex acoustic impedance also results from the prevalence of the imaginary part of the asymmetry coefficient, as shown in the color map of η in Fig. 3.14. The expanded ranges of the complex refractive index and acoustic impedance offer superior control of acoustic wave propagation through the active Willis coupled metamaterial.

3.2.4 Metamaterial circuit design

Based on Equations 3.5-3.7 in the main text, the active transmission and reflection of the metamaterial can be directly controlled by the gain functions G_1 and G_2. These gain functions can be realized by the active circuits shown in Fig. 3.11b. The phase shift of either gain function is given by

$$\theta = -2\arctan(R_{2(1,2)}C_{1(1,2)}\omega), \tag{3.11}$$

where θ indicates the final phase shift, $R_{2(1,2)}$ is the variable resistor value, $C_{1(1,2)}$ is the capacitance value, and ω is the angular frequency of the signal. The phase shift in Equation 3.11 only covers $[0, \pi]$. It is important to note that the positions of the resistor and capacitor ($R_{2(1,2)}$ and $C_{1(1,2)}$ in Fig. 3.11b) can be reversed to provide a positive or negative phase shift. This enables phase shifting over the entire range of 2π. The amplitude of the gain function can be controlled by the non-inverting op-amp circuits and voltage dividers to amplify or attenuate input voltage signals. The amplitude modulation is

$$V_{out} = V_{in}(1 + \frac{R_{4(1,2)}}{R_{3(1,2)}})(\frac{R_{6(1,2)}}{R_{5(1,2)}+R_{6(1,2)}}), \tag{3.12}$$

where V_{out} is an output voltage amplitude, V_{in} is an input voltage amplitude, and $R_{3(1,2)}$, $R_{4(1,2)}$, $R_{5(1,2)}$, and $R_{6(1,2)}$ are the resistors in Fig. 3.11b. Although the active response is fully controllable through the manipulation of the circuit components, certain conditions are required to avoid instability; specifically, the denominators of Equations 3.5-3.7 must be greater than zero to avoid the divergence of the feedback loop, implying the product of G_1 (G_2) and h_{io} must be less than one. The experimentally determined values of h_{io} in [18] yield a frequency-dependent magnitude consistently under 0.2. Therefore, the gain amplitudes need to be less than 5. Thus, we restrict the amplitude of the gain functions to [0,5] in this work, while their phases vary in the full range of 2π.

We use Equations 3.11 and 3.12 to calculate the resistance and capacitance values for the active circuits in the unit cell that achieve the desired amplitude and phase of the gain functions G_1 and G_2 for Willis and non-Willis metamaterials. The first non-Willis case presented in the main text occurs when $G_1 = G_2 = 2e^{i(0.87)}$, and is achieved with the active circuitry in Fig. 3.11b when $R_{1(1,2)} = 10k\Omega$, $R_{2(1,2)} = 1.865k\Omega$, $R_{3(1,2)} = R_{4(1,2)} = R_{5(1,2)} = R_{6(1,2)} = 1k\Omega$ and $C_{1(1,2)} = 100nF$. The first Willis coupling case is achieved when $G_1 \neq G_2$, and set $G_1 = 2e^{i(0.87)}$ and $G_2 = 0.6e^{i(2.79)}$ with the active circuitry $R_{1(2)} = 10k\Omega$, $R_{2(2)} = 6.93k\Omega$, $R_{3(2)} = R_{5(2)} = R_{6(2)} = 1k\Omega$, $R_{4(2)} = 200\Omega$, and $C_{1(2)} = 100nF$. The resistance $R_{2(2)}$ are changed to control the phase of G_2 in this case, but it is worth noting that the change of the capacitance can result in the same G_2 phase as long as the product of $R_{2(2)}$ and $C_{1(2)}$ remains constant. A second Willis coupling case sets $G_1 = 2e^{i(0.87)}$ and $G_2 = 0.15e^{i(4.10)}$ with the active circuitry $R_{1(2)} = 10k\Omega$, $R_{2(2)} = 886.8k\Omega$, $R_{3(2)} = R_{4(2)} = R_{6(2)} = 1k\Omega$, $R_{5(2)} = 450\Omega$, and $C_{1(2)} = 100nF$.

To view the effects of circuit error on the effective material parameters, we study an extreme point in the fourth quadrant of Fig. 3.13a that is achieved when $G_1 = 3.025e^{i(4.36)}$ and $G_2 = 2.12e^{i(2.18)}$ with active circuitry $R_{1(1)} = 10k\Omega$, $R_{2(1)} = 5.712k\Omega$, $R_{3(1)} = R_{5(1)} = R_{6(1)} = 1k\Omega$, $R_{4(1)} = 2.025k\Omega$, and $C_{1(1)} = 100nF$ and $R_{1(2)} = 10k\Omega$, $R_{2(2)} = 14.928k\Omega$, $R_{3(2)} = R_{5(2)} = R_{6(2)} = 1k\Omega$, $R_{4(2)} = 1.12k\Omega$, and $C_{1(2)} = 100nF$ resulting in a normalized effective density and bulk modulus $Re(\rho) = 5.39 \times 10^5$ and $Re(\kappa) = -1.81 \times 10^4$. For normal circuit components containing five percent error in their resistance or capacitance value, the resulted errors of the real part of the effective density and bulk modulus are -317.1% to 138.0% and -115.4% to 189.7% at this outer most point, respectively. Another extreme point occurs in the third quadrant of Fig. 3.13c with the largest magnitude of the negative imaginary part of the effective density. These effective parameter values are achieved when $G_1 = 4.20e^{i(3.67)}$ and $G_2 = 2.095e^{i(3.84)}$ with active circuitry $R_{1(1)} = 10k\Omega$, $R_{2(1)} = 14.928k\Omega$, $R_{3(1)} = R_{5(1)} = R_{6(1)} = 1k\Omega$, $R_{4(1)} = 3.20k\Omega$, and $C_{1(1)} = 100nF$ and $R_{1(2)} = 10k\Omega$, $R_{2(2)} = 10.989k\Omega$, $R_{3(2)} = R_{5(2)} = R_{6(2)} = 1k\Omega$, $R_{4(2)} = 1.095k\Omega$, and $C_{1(2)} = 100nF$ resulting in a normalized effective density and bulk modulus $Im(\rho) = -1.24 \times 10^5$ and $Im(\kappa) = -1.18x10^3$. Circuit components with a five percent error in their resistance or capacitance values have errors in the imaginary part of the effective density and bulk modulus of -1087.0% to

380.5% and -773.9% to 386.7% at this outer most point, respectively. The highly sensitive effective material parameters indicate the difficulty of achieving the most extreme parameter values in experiments.

3.2.5 Quality factor of the metamaterial

We study the quality factor of the effective material parameters to find that the extreme points in a selected data set do not require a high quality factor. We calculate the quality factor of the metamaterial unit cell based on the conventional definition for acoustic resonators in between 2.00 kHz to 3.00 kHz and plot the corresponding effective density and bulk modulus with the quality factor shown as a color map (Fig. 3.15). As shown, the quality factor required to achieve the most extreme points is lower than 50, which is achievable experimentally.

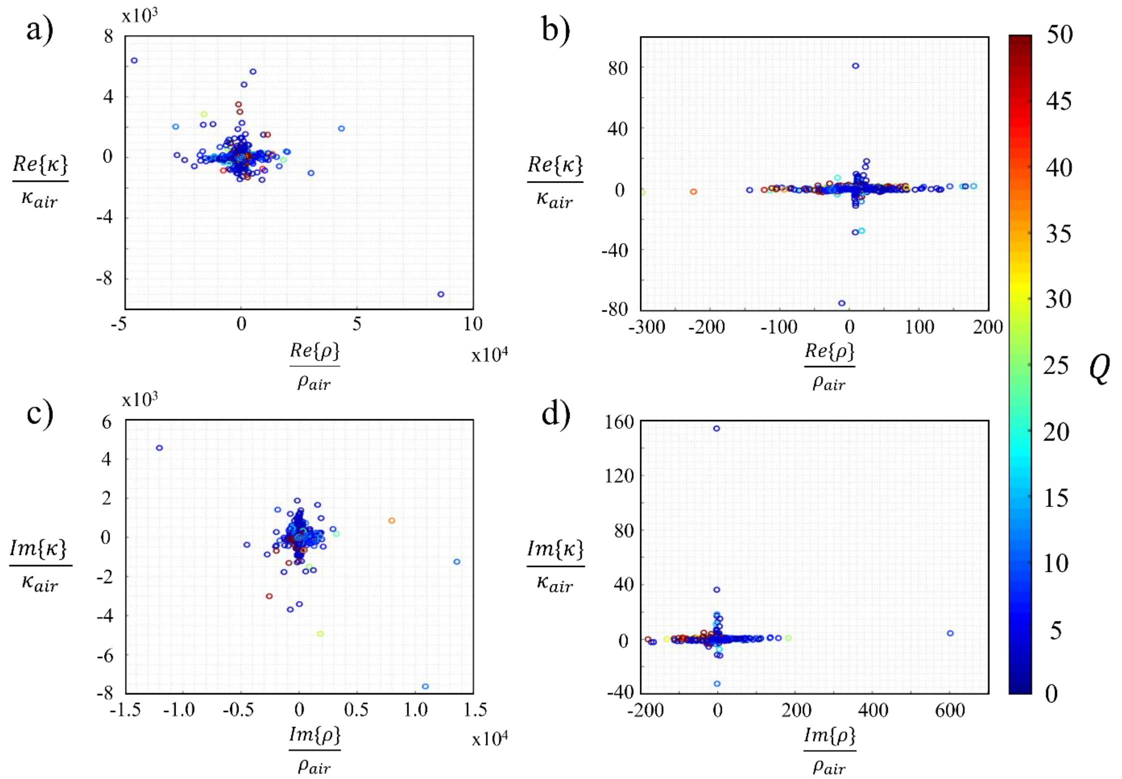

Figure 3.15: Effective material parameter plots for a non-Willis and Willis unit cell (a) Effective parameter map of the real part of the density and bulk modulus for the active metamaterial with Willis coupling. The real part of the effective density and bulk modulus are plotted on the horizontal and vertical axes, respectively. The color map quantifies the quality factor based on the conventional definition for acoustic resonators. (b) Effective parameter map of the real part of the density and bulk modulus for the active metamaterial without Willis coupling. The axes and color map in this subfigure are identical to (a). (c) Parameter map of the imaginary part of the effective density and bulk modulus for the active metamaterial with Willis coupling. The imaginary part of the effective density and bulk modulus are plotted on the horizontal and vertical axes, respectively. This subfigure has the same color scheme as (a). (d) Effective parameter map of the imaginary part of the density and bulk modulus for the active metamaterial without Willis coupling. The axes and color map in this subfigure are identical to (c).

CHAPTER 4

TRANSFORMATION ACOUSTICS

This thesis chapter contains material that has been published in Applied Physics Letters [127].

4.1 Introduction

The constitutive relations that govern wave propagation through a medium directly depend on the physical properties of the materials. This intrinsic relationship motivates researchers to create complex materials that manipulate wave propagation through mathematically defined coordinate transformations, known as transformation electromagnetics and acoustics [108,109,128]. This mapping leads to a unique design of wave bending and distortion that realizes electromagnetic and acoustic invisibility cloaks [15,110-112]. The transformation electromagnetics and acoustics are valid when the field equations describing wave propagation is invariant under coordinate transformations [108,109]. This is known to be true for Maxwell's field equations, and enable the theoretical development transformation electromagnetics [129-131]. Transformation invariance is also true for acoustics, given an anisotropic mass density tensor [132,133]. Transformation acoustics allows the design of acoustic metamaterials with effective anisotropic mass density properties that are used to experimentally demonstrate acoustic cloaking [15,111,112] and gradient index sonic lenses [134-136].

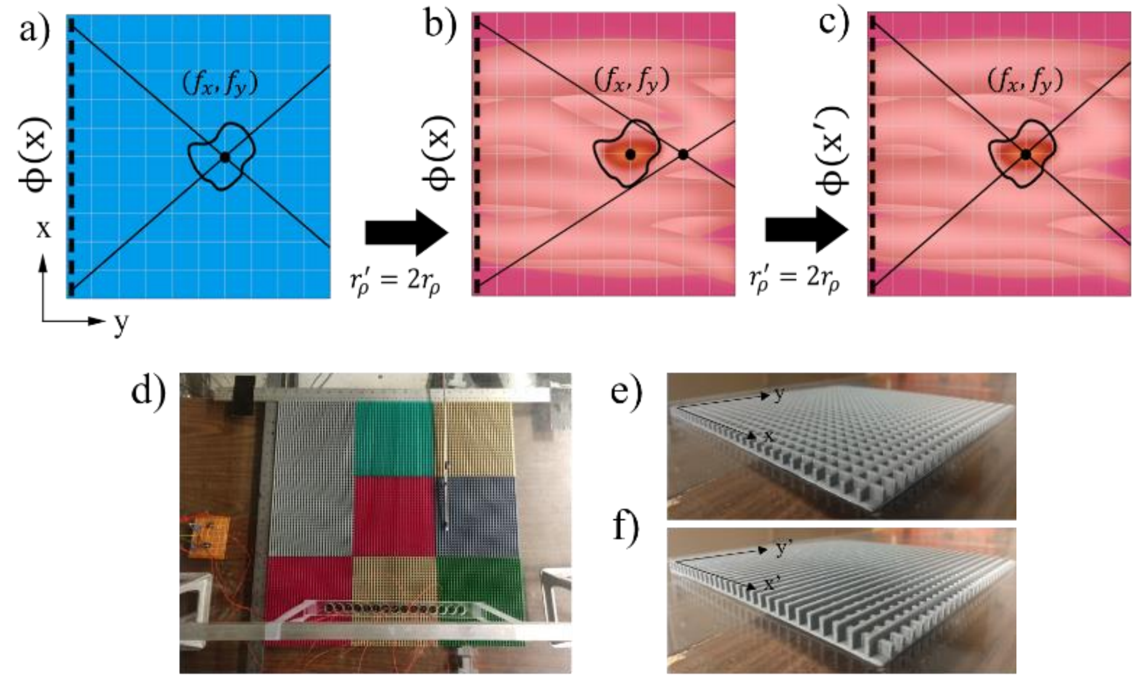

Figure 4.1: Anisotropic distortion of beamformed acoustic waves with the experiment setup. (a) Discretized transducer array with a phase gradient as a function of the x axis such that the desired acoustic focusing is achieved in an isotropic medium. (b) Identical transducer array with the same phase gradient in an anisotropic medium resulting in a focal point shifted from the desired location. (c) Same transducer array with a corrected phase gradient that restores the focal point to its original location. (d) Experimental setup in which two-dimensional SSAWs propagate across effective isotropic and anisotropic gratings. (e) Close up of the isotropic grating design. (f) Close up of the anisotropic grating design.

On the other hand, transformation acoustics facilitates the mapping of wave patterns in sophisticated materials to medium where the precise modeling of wave propagation is well-understood. This is critical for high precision applications in which acoustic waves propagate through anisotropic media; prime examples being biomedical acoustics and integrated on-chip systems. In recent years, biomedical ultrasound has demonstrated the ability to ablate cancerous tumors [24-29], pulverize kidney stones [30], and clear aortic plaque [33,34] in addition to being a noninvasive imaging tool for diagnostic purposes [40-44,137]. For many of these applications, beamforming by manipulating a phased array to generate a desired wave pattern in the body is critical (Fig. 4.1a). In addition to applications for bulk acoustic waves, integrated on-chip systems use surface acoustic waves (SAW) to manipulate, trap, and sort cells in a controlled environment [138,139]. These on-chip devices commonly use anisotropic piezoelectrics to support SAW propagation. For both bulk and surface acoustic waves, effective anisotropy distorts beamformed wave fronts and drastically affects the performance of the desired application (Fig. 4.1b). To address these effects, we apply a coordinate transformation to correlate anisotropic wave distortion with a required phase profile correction. In doing so, any unwanted anisotropic effects are suppressed, and the intended beamforming is restored (Fig. 4.1c). Here, we demonstrate the effectiveness of beamforming correction in anisotropic media using transformation acoustics for biomedical and on-chip applications via experimental validation using finned grating surfaces that support two-dimensional spoof surface acoustic waves (SSAWs) for focused and self-bending beams (Fig. 4.1d) [140,141]. Based on the dispersion relation of the grating [142], we mimic effective isotropic (Fig. 4.1e) and anisotropic (Fig. 4.1f) media by varying the fin heights in x and y directions. First, we apply transformation acoustics to correct focused ultrasound beams in anisotropic media.

4.2 Correcting focused acoustic waves

The focusing of the acoustic waves in an isotropic medium can be achieved by a transducer array with phase profile given by [143-147]

$$\phi(x) = -k_0\left[\sqrt{(x-f_x)^2+\left(y-f_y\right)^2}-f_y\right], \tag{4.1}$$

where $\phi(x)$ is the transducer phase along the horizontal axis, k_0 is the wave number of the isotropic medium, and f_x and f_y are the coordinates of the focal point. The origin is set at the center of the transducer array. The focal point is chosen to be at (70 mm, 150 mm) for 9 kHz waves in our experiment. As expected, the phase gradient determined by Equation 4.1 focuses the acoustic energy to the desired focal point in an isotropic medium in a numerical simulation (Fig. 4.2a). On the other hand, the same phase profile of the transducer array results in a shifted focal spot in an anisotropic medium with effective density 1.35 times greater in *x* than *y* (Fig. 4.2b). To correct for this shift, we map the coordinates (*x*, *y*) of the original isotropic medium to the coordinates (*x'*, *y'*) of the anisotropic medium with x = [$\sqrt{r_\rho}\cos(\theta)x' - \sin(\theta)y'$] and y = [$\sqrt{r_\rho}\sin(\theta)x' + \cos(\theta)\,y'$], where r_ρ is the ratio between the anisotropic density in the *x'* direction and the isotropic density, assuming the anisotropic density in *y'* direction is the same as the isotropic density and θ is the angle between the transducer array and the *x'* principle axis of the anisotropic medium. This coordinate transformation compensates the wavelength distortion along the principle axis due to the variance of sound speed as a result of the anisotropic density ($c_{x'} = c/\sqrt{r_\rho}$, where c and $c_{x'}$ are the sound speeds in the isotropic medium and along the *x'* axis in anisotropic medium, respectively). Substituting this transformation in Equation 4.1 yields the corrected phase profile for focused acoustic beams in an anisotropic medium (See Section 4.4.1 for details)

$$\phi(x', y') = -k_0\left[\sqrt{r_\rho(x' - f_x')^2 + \left(y' - f_y'\right)^2} - \frac{\sqrt{r_\rho}(y' f_x' + x' f_y')}{\sqrt{r_\rho x'^2 + y'^2}}\right]. \tag{4.2}$$

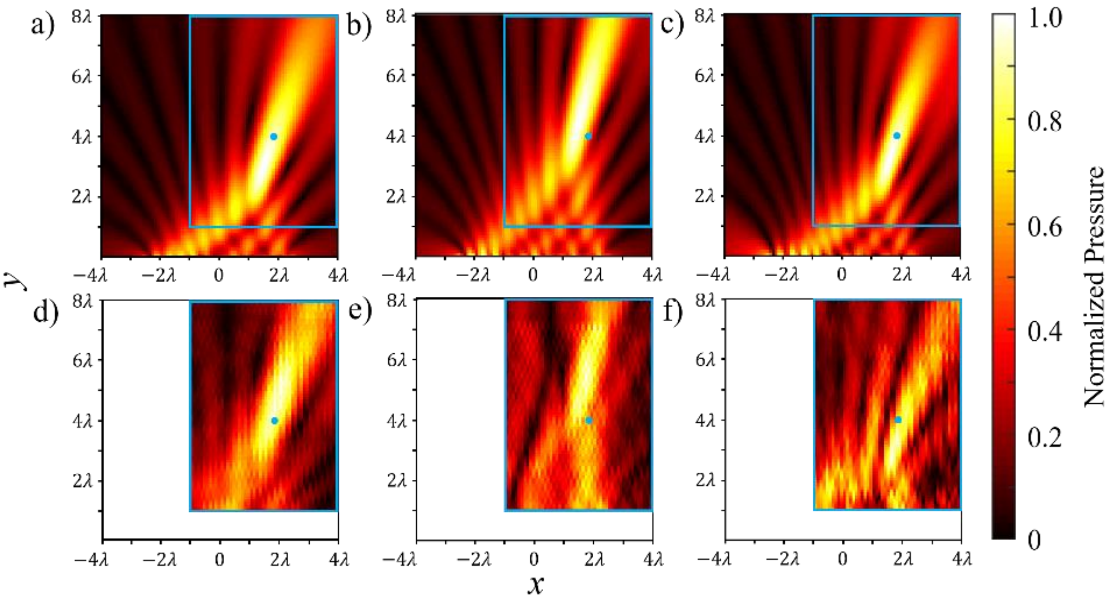

Figure 4.2: Simulation and experiment results for arbitrarily focused acoustic beams. (a) Simulation results of a focused acoustic beam in a two-dimensional isotropic medium that focuses 70 mm to the right and 150 mm above the center of the speaker array. (b) Simulation results of a focused acoustic beam in an effective two-dimensional anisotropic medium with the same phase profile as (a). Here, the resulted focal point shifts from the desired location. (c) Simulation results of a focused acoustic beam in an effective two-dimensional anisotropic medium with a corrected phase profile with a focal point matching (a). (d) Experimental replication of the simulation in (a) with a matching focal point. (e) Experimental replication of the simulation in (b) with a matching focal point. (f) Experimental replication of the simulation in (c) with a matching focal point.

Applying this phase gradient with the aforementioned anisotropic density ratio shifts the focal point back to its intended location (Fig. 4.2c). We perform experiments with the previously mentioned finned grating structures to verify the transformation. Isotropic and anisotropic grating surfaces were 3D printed and assembled from smaller square grating structures that combine to have a square surface area of 533×533 mm^2 (Fig. 4.1d). Small gaps or misalignments between gratings cause acoustic reflections that impact the beamforming performance, resulting in experimental error. The dispersion relation of the gratings determines the specific dimensions of each structure to mimic an effective isotropic

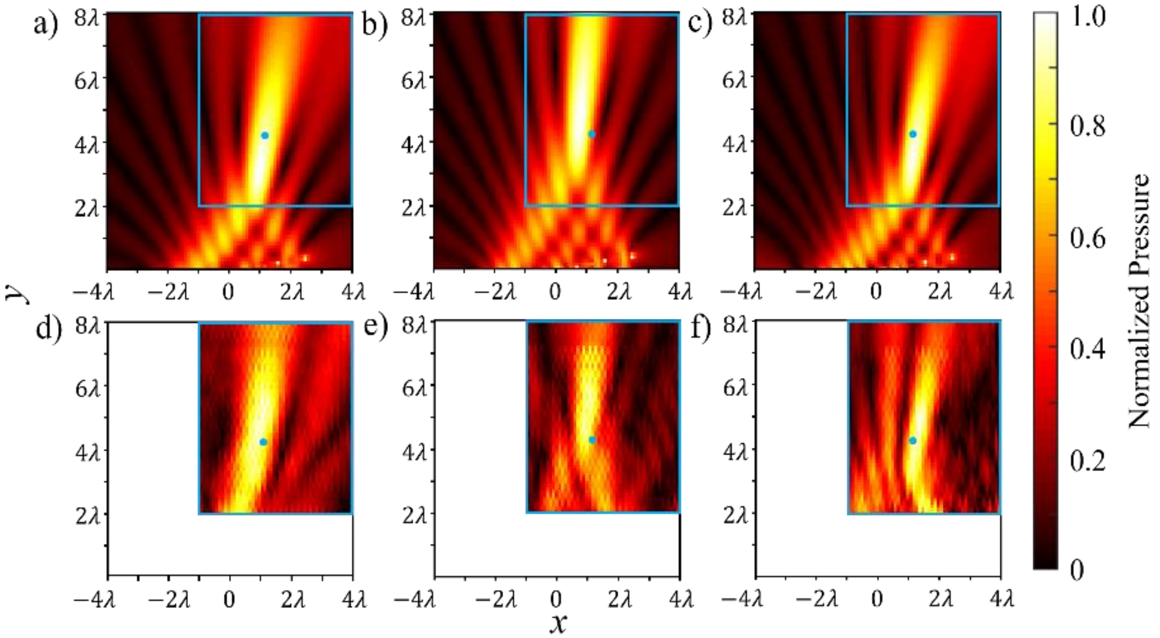

Figure 4.3: Simulation and experiment results for arbitrarily focused beams with a tilted source. (a) Simulation results of a focused acoustic beam in a two-dimensional isotropic medium that achieves the desired focal point with a ten-degree tilt. (b) Simulation results of a focused acoustic beam with the same phase profile in an effective two-dimensional anisotropic medium. Here, the focal point shifts from the focal point of the isotropic case. (c) Simulation results of a focused acoustic beam in an effective two-dimensional anisotropic medium with a corrected phase profile resulting in focusing at the desired focal point (d) Experimental replication of (a) with a matching focal point. (e) Experimental replication of (b) with a matching focal point. (f) Experimental replication of (c) with a matching focal point.

or anisotropic medium. Acoustic surface waves were generated with a transducer array consisting of twelve 17 mm diameter speakers with 19 mm periodicity. The phase gradients were created with a digital multichannel recorder with independent channels to control the phase profile. To measure the resulted pressure field, an omnidirectional microphone attached to a motorized positioner scanned a planar area (5λ by 7λ, where the wavelength in the isotropic medium λ= 38.1 mm) 2 mm above the grating surfaces with a scan resolution of λ/10 for each case (Fig. 4.2d-4.2f). A lock-in amplifier recorded the amplitude and phase of the acoustic waves to reconstruct the pressure fields above the grating surfaces. For an isotropic grating with a predetermined focal point at (70 mm, 150 mm) when the transducer array aligns with the *x'* axis, the acoustic intensity pattern matches with the desired focal point denoted by the blue dot in Fig 4.2d. When the same phase profile is applied to focus the acoustic wave on the anisotropic grating, the focal point shifts from the desired location to (57.15 mm, 209.55 mm) (Fig. 4.2e). Using the corrected phase profile in Equation 4.2, the focal point shifts back to its intended location (Fig. 4.2f).

The derived phase correction from transformation acoustics is also valid for more general cases in which the anisotropic axes are not in line with the speaker array. To demonstrate the focusing correction with misalignment, we tilt the transducer array 10 degrees and focus the acoustic wave to the same focal spot at 9 kHz. The theoretical model focuses the acoustic energy at the predetermined location (the blue dot) as illustrated in Fig. 4.3a. Again, switching the propagation medium to the anisotropic grating displaces the focal point to (38.1 mm, 215.65 mm) (Fig. 4.3b), while the corrected phase profile given by Equation 4.2 restores the focal point to its proper location in Fig. 4.3c. Experimental validation of the off axis anisotropic density is performed with a nearly identical experimental setup as the previous case. However, the microphone's scan area is reduced to a 5λ by 6λ rectangular area (indicated by the blue rectangle in Figs. 4.3a-4.3f) to avoid collision with the tilted transducer array. The experimental demonstration with propagation above the isotropic grating results in a focal point (Fig. 4.3d) in agreeance with the theoretical results shown in Fig. 4.3a. Switching the grating surface to the anisotropic medium shifts the focal point (Fig. 4.3e), matching the results in Fig. 4.3b, while applying the corrected phase profile shifts the focal point back to its intended location (Fig. 4.3f), matching Fig. 4.3c.

4.3 Correcting self-bending acoustic beams

To further demonstrate the effectiveness of transformation acoustics correcting anisotropic distortions, we restore the curved interference patterns of self-bending acoustic beams in anisotropic media. Without loss of generality, the resulted curved pattern of the acoustic beam is chosen to be $f(y) = \sqrt{r^2 - (y - r)^2}$,where r is the radius of the semicircular curve. The corresponding transducer array phase profile derived in [143-147] and applied in an isotropic numerical simulation to achieve an acoustic energy intensity profile matching the aforementioned equation (Fig. 4.4a). However, using the same phase profile on the transducer array in the previously discussed anisotropic medium distorts the semicircular interference pattern, resulting in an elliptical intensity profile (Fig. 4.4b). We use transformation acoustics to restore the original semicircular pattern (Fig. 4.4c) by applying the same coordinate transformation as the focusing case to correct the phase gradient. To verify the transformation, we conduct experiments using the previously described experimental setup where the transducer array is in line with the x' axis. For an isotropic grating with a semicircular acoustic interference pattern having radius 4λ, the acoustic intensity pattern matches the desired trajectory denoted by the blue arc in Fig 4.4d. When the same phase profile is applied on the anisotropic grating, the circular trajectory distorts to form an elliptical arc (Fig. 4.4e). Using the corrected phase profile, derived in section 4.4.2, the beam is restored back to its intended interference pattern (Fig. 4.4f).

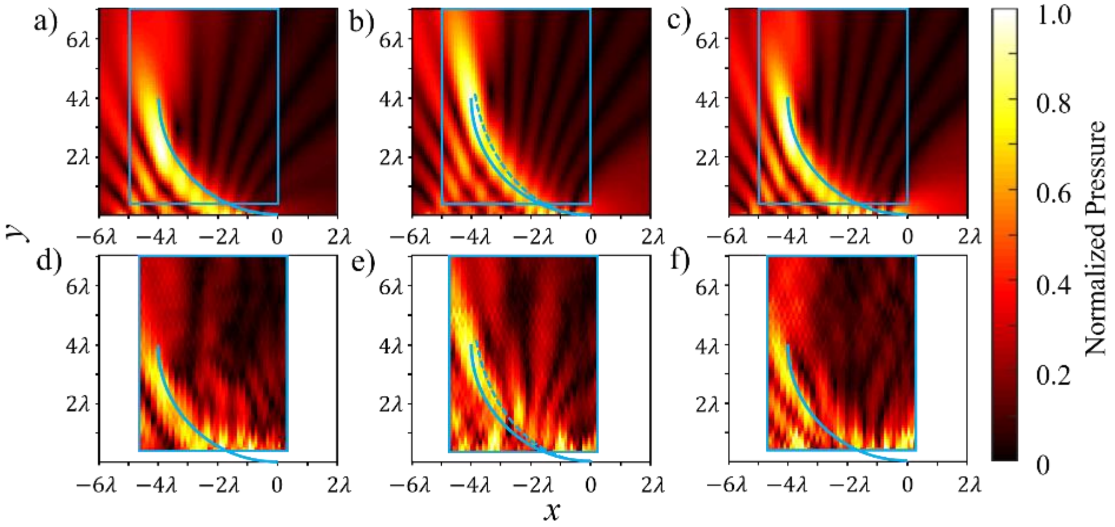

Figure 4.4: Simulation and experiment results for self-bending acoustic beams. (a) Simulation results of a self-bending acoustic beam in a two-dimensional isotropic medium that matches the desired beam pattern. (b) Simulation results of a self-bending acoustic beam in an effective two-dimensional anisotropic medium with the same phase profile. Here, the intensity profile shifts from the desired interference pattern. (c) Simulation results of a self-bending acoustic beam in an effective two-dimensional anisotropic medium with a corrected phase profile. Here, the resulted curved interference pattern matches the desired intensity profile in the isotropic case. (d) Experimental replication of the simulation in (a) with a matching curved interference pattern. (e) Experimental replication of (b) with a matching interference pattern. (f) Experimental replication of (c) with a matching interference pattern.

4.4 Focused and self-bending beam derivations

4.4.1 Focused beam

We use transformation acoustics to derive a phase gradient that corrects anisotropic distortions for focused acoustic beams in complex media. The transformation maps the coordinates (*x*, *y*) of the original isotropic medium to the coordinates (*x’*, *y’*) of the anisotropic medium with $x = [\sqrt{r_\rho}\cos(\theta)x' - \sin(\theta)y']$ and $y = [\sqrt{r_\rho}\sin(\theta)x' + \cos(\theta)\, y']$, where r_ρ is the ratio between the anisotropic density in the *x’* direction and the isotropic density and θ is the angle between the transducer array and the *x’* principle axis of the anisotropic medium. Substituting this coordinate mapping into the original phase profile that achieves focusing in an isotropic medium results in a phase profile that corrects for anisotropic distortions and correctly focuses beamformed acoustic waves in anisotropic media as,

$$\phi(x') = -k_0\left[\left(\sqrt{r_\rho}\cos(\theta)x' - \sin(\theta)y' - \sqrt{r_\rho}\cos(\theta)f_x' + \sin(\theta)\,f_y'\right)^2 + \left(\sqrt{r_\rho}\sin(\theta)x' + \cos(\theta)y' - \sqrt{r_\rho}\sin(\theta)f_x' - \cos(\theta)\,f_y'\right)^2\right]^{1/2} + k_0(\sqrt{r_\rho}\sin(\theta)f_x' + \cos(\theta)\,f_y'), \tag{4.3}$$

where k_0 is the isotropic wavenumber, and $\phi(x')$ is the transducer phase in the anisotropic medium. Further simplification of this expression leads to the final corrected phase gradient in Section 4.2 with the following steps: First, we combine the trigonometric terms in equation 4.3 as,

$$\phi(x') = -k_0\left[\left(\sqrt{r_\rho}\cos(\theta)(x' - f_x') - \sin(\theta)\left(y' - f_y'\right)\right)^2 + \left(\sqrt{r_\rho}\sin(\theta)(x' - {f_x}') + \cos(\theta)(y' - f_y')\right)^2\right]^{\frac{1}{2}} + k_0\left(\sqrt{r_\rho}\sin(\theta)f_x' + \cos(\theta)\,f_y'\right). \tag{4.4}$$

Squaring the terms in equation 4.4 results in the expression,

$$\phi(x') = -k_0\left[r_\rho\cos^2(\theta)\,(x' - f_x')^2 + \sin^2(\theta)\left(y' - f_y'\right)^2 - 2\sqrt{r_\rho}\cos(\theta)\sin(\theta)\,(x' - f_x')(y' - f_y') + r_\rho\sin^2(\theta)\,(x' - f_x')^2 + \cos^2(\theta)\left(y' - f_y'\right)^2 + 2\sqrt{r_\rho}\cos(\theta)\sin(\theta)\,(x' - f_x')(y' - f_y')\right]^{\frac{1}{2}} + k_0\left(\sqrt{r_\rho}\sin(\theta)f_x' + \cos(\theta)\,f_y'\right). \tag{4.5}$$

Trigonometric identities further simplify the argument of the square root to the expression shown:

$$\phi(x') = -k_0\sqrt{r_\rho(x'-f_x')^2+\left(y'-f_y'\right)^2} + k_0(\sqrt{r_\rho}\sin(\theta)f_x' + \cos(\theta)\, f_y'). \quad (4.6)$$

The final term on the right is further reduced by expressing sine and cosine in terms of the prime coordinate system as,

$$\sin(\theta) = \frac{y\prime}{\sqrt{r_\rho x\prime^2 + y\prime^2}}, \quad (4.7)$$

$$\cos(\theta) = \frac{\sqrt{r_\rho}x\prime}{\sqrt{r_\rho x\prime^2 + y\prime^2}}. \quad (4.8)$$

Plugging in equations (4.7) and (4.8) into equation (4.6) results in the expression,

$$\phi(x') = -k_0\sqrt{r_\rho(x'-f_x')^2+\left(y'-f_y'\right)^2} + k_0\left(\frac{\sqrt{r_\rho}y'}{\sqrt{r_\rho x'^2+y'^2}}f_x' + \frac{\sqrt{r_\rho}x'}{\sqrt{r_\rho x'^2+y'^2}}f_y'\right), \quad (4.9)$$

which further simplifies to the phase gradient in Section 4.2 that corrects focused acoustic beams in anisotropic media,

$$\phi(x') = -k_0\left[\sqrt{r_\rho(x'-f_x')^2+\left(y'-f_y'\right)^2} - \frac{\sqrt{r_\rho}(y'f_x'+x'f_y')}{\sqrt{r_\rho x'^2+y'^2}}\right]. \quad (4.10)$$

4.4.2 Self-bending beam

We use transformation acoustics to derive a phase gradient that corrects anisotropic distortions on curved intensity profiles in complex media. In contrast to the focused

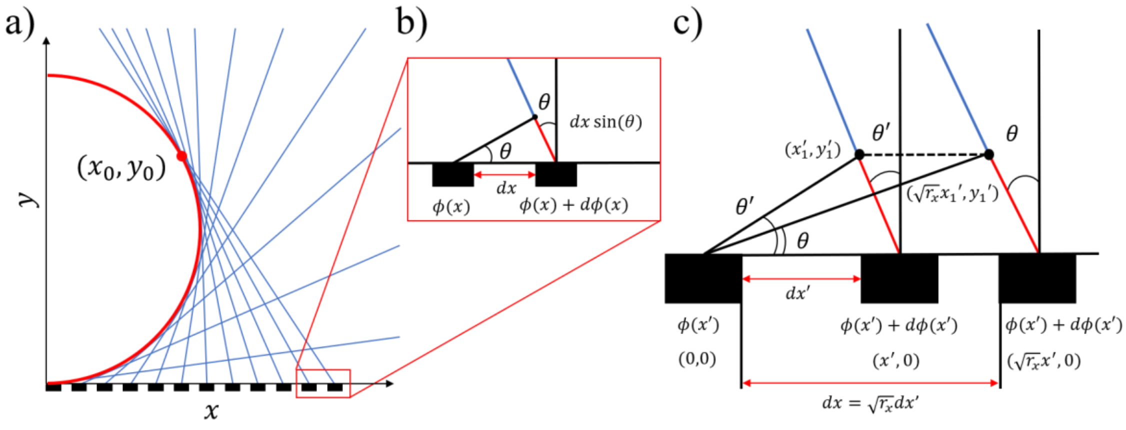

Figure 4.5: Derivation of the self-bending beam correction technique. (a) Geometric interpretation of a transducer array outputting a convex, curved acoustic beam represented by the red semicircle. The acoustic ray paths, represented by blue lines, are outputs from the transducer array along the x axis forming the desired curve with some determined phase gradient along the x axis. (b) Close up of the general relationship that defines the direction of an acoustic ray outputting from a transducer to its phase change along the x axis. (c) Transducers with transformed coordinate locations and the same phase output produce acoustic ray trajectories at different angles when compared to their untransformed counterparts.

correction, we cannot directly substitute the anisotropic coordinate mapping into the final phase gradient to restore the beamformed interference pattern to its desired shape in an isotropic medium. Instead, we transform the geometric equations used to derive the phase gradient of curved intensity profiles in isotropic media. These equations are given by [143-147],

$$f'(y_0) = -\tan(\theta), \tag{4.11}$$

$$x = x_0 + y_0\tan(\theta), \tag{4.12}$$

$$\frac{d\phi(x)}{dx} = -k_0\sin(\theta), \tag{4.13}$$

where k_0 is the isotropic wavenumber, θ is the angle between the vertical axis and acoustic ray trajectory, $\phi(x)$ is the transducer phase along the x axis, and (x_0, y_0) is a point on the curved beam trajectory. Expressions 4.11-4.13 all have simple geometric interpretations illustrated in Figs. 4.5a-4.5b. For example, Equation 4.11 is understood as the slope of a tangent line at any point (x_0, y_0) on the red curve, where as Equation 4.12 simply traces the acoustic ray path from a point on the curve (x_0, y_0) back to the x axis. The final geometric relation, Equation 4.13, correlates the angle of an acoustic ray output from a transducer on the x axis to the phase change from that source (Fig. 4.5b). With these geometric relations, we determine a phase gradient $\phi(x)$ that constructs an acoustic intensity profile resulting in a convex trajectory in an isotropic medium.

To replicate the desired intensity profile in an anisotropic medium, we use transformation acoustics to modify the geometric Equations 4.11-4.13 by mapping the original isotropic coordinate system (x, y) to the anisotropic coordinate system (x', y') with $y = y'$ and $x = \sqrt{r_\rho} x'$. Once this mapping transforms the transducer locations along the x axis, the angle of the acoustic ray trajectories shifts due to the effective spacing of the transducers (Fig. 4.5c). To correct for this angle change, we map the trigonometric terms dependent on θ in the isotropic medium to the trigonometric terms dependent on θ' in the anisotropic medium with $\tan(\theta) = \sqrt{r_\rho}\tan(\theta')$ and $\sin(\theta) = \sin\left(\arctan\left(\sqrt{r_\rho}\tan(\theta')\right)\right)$. These coordinate mappings redefine Equations 4.11-4.13 to represent the same geometric relationships in an anisotropic medium,

$$f'(y_0') = -\sqrt{r_\rho}\tan(\theta'), \tag{4.14}$$

$$x' = x_0' + y_0' \tan(\theta'), \tag{4.15}$$

$$\frac{d\phi(x')}{dx'} = -\sqrt{r_\rho} k_0 \sin\left(\arctan\left(\sqrt{r_\rho}\tan(\theta')\right)\right). \tag{4.16}$$

With these transformed equations, we derive a phase gradient that constructs a circular interference path in an anisotropic medium. To begin this derivation, we define the desired intensity profile of the circular interference pattern in an isotropic medium as,

$$\frac{x^2}{r_x^2} + \frac{(y - r_y)^2}{r_y^2} = 1, \tag{4.17}$$

where r_x and r_y are the radii of the curve in the *x* axis and *y* axis directions respectively. In addition to transforming the coordinate axes, we transform these radii terms by mapping $r_x = \sqrt{r_\rho} r'$ and $r_y = r'$. Substituting these transformations into Equation 4.17 results in the intensity profile we achieve in the anisotropic medium,

$$\frac{x'^2}{r'^2} + \frac{(y' - r_y')^2}{r'^2} = 1. \tag{4.18}$$

Solving Equation 4.18 for *x'* yields,

$$x' = \sqrt{r'^2 - (y' - r')^2}. \tag{4.19}$$

This equation is satisfied for any point along this curve as,

$$x_0' = \sqrt{r'^2 - (y_0' - r')^2}, \tag{4.20}$$

which is used to relate back to our governing geometric equations. Taking the derivative of Equation 4.20 and inputting this relation into Equation 4.14 yields,

$$-\frac{(y_0' - r')}{\sqrt{r'^2 - (y_0' - r')^2}} = -\sqrt{r_\rho} \tan(\theta'), \tag{4.21}$$

where y_0' is solved for as,

$$y'_0 = r'\left(\frac{\sqrt{r_\rho}\tan(\theta')}{\sqrt{1+r_\rho\tan^2(\theta')}} + 1\right). \tag{4.22}$$

Inputting 4.22 into 4.20 gives an expression for x'_0 as,

$$x'_0 = r'\sqrt{\frac{1}{1+r_\rho\tan^2(\theta')}}. \tag{4.23}$$

Now that we have expressions for x'_0 and y'_0, we express Equation 4.15 in terms of θ' as,

$$x' = r'\sqrt{\frac{1}{1+r_\rho\tan^2(\theta')}} + r'\left(\frac{\sqrt{r_\rho}\tan(\theta')}{\sqrt{1+r_\rho\tan^2(\theta')}} + 1\right)\tan(\theta'). \tag{4.24}$$

Equation 4.24 is now used to derive the phase relation along the *x'* axis with Equation 4.16. Expressing Equation 4.16 in terms of θ' yields,

$$\frac{d\phi(\theta')}{d\theta'}\frac{d\theta'}{dx'} = -\sqrt{r_\rho}k_0\sin\left(\arctan\left(\sqrt{r_\rho}\tan(\theta')\right)\right), \tag{4.25}$$

which is used to determine the relative transducer phase delay along the *x'* axis.

$$\phi(\theta')_a - \phi(\theta')_b = \int_{\theta'_a}^{\theta'_b} -\sqrt{r_\rho}k_0\sin\left(\arctan\left(\sqrt{r_\rho}\tan(\theta')\right)\right)\frac{dx'}{d\theta'}d\theta' \tag{4.26}$$

Equation 4.26 gives the relative phase difference between transducers to reconstruct the desired self-bending beam defined in Equation 4.18. With known transducer coordinates along the *x'* axis, we determine the θ values of the self-bending beam to numerically solve Equation 4.26 and yield the final transducer phase gradient that beamforms the desired acoustic intensity profile.

4.5 High anisotropy, grating dispersion, and full-wave simulations

4.5.1 High anisotropy

We further test the validity of the corrected phase gradient by restoring the curved interference pattern of self-bending beams in anisotropic media with significantly higher density ratios compared to Sections 4.2 and 4.3. Since the following study is purely numerical, we idealize the simulations with a larger transducer array that spans 10λ comprised of 1200 acoustic sources. Once again, the desired path of the acoustic beam propagates along a semicircular arc with radius 4λ defined by the function, $f(y) = \sqrt{r^2 - (y - r)^2}$. The corresponding transducer phase gradient determined by Equation 4.26 for an isotropic medium is applied to achieve an acoustic energy intensity profile matching the desired interference pattern denoted by the blue arc in Fig. 4.6a. However, using the same phase gradient on the transducer array in an anisotropic medium with an effective density 2 times greater in x than y severely distorts the interference pattern, resulting in an elliptical intensity profile following the dashed blue arc in Fig. 4.6b. To correct for this distortion, we consider the anisotropy of the medium and calculate a corrected phase gradient with Equation 4.26 to restore the original semicircular interference pattern. Applying the corrected phase gradient with the aforementioned anisotropic density ratio restores the circular interference pattern, as illustrated by Fig. 4.6c. To further demonstrate the effectiveness of the correction technique, the same study is repeated for an anisotropic medium with an effective density ratio 4 times greater in x than y. Once again, the previously determined isotropic phase gradient is applied in an isotropic medium to achieve an acoustic energy intensity profile that matches the desired

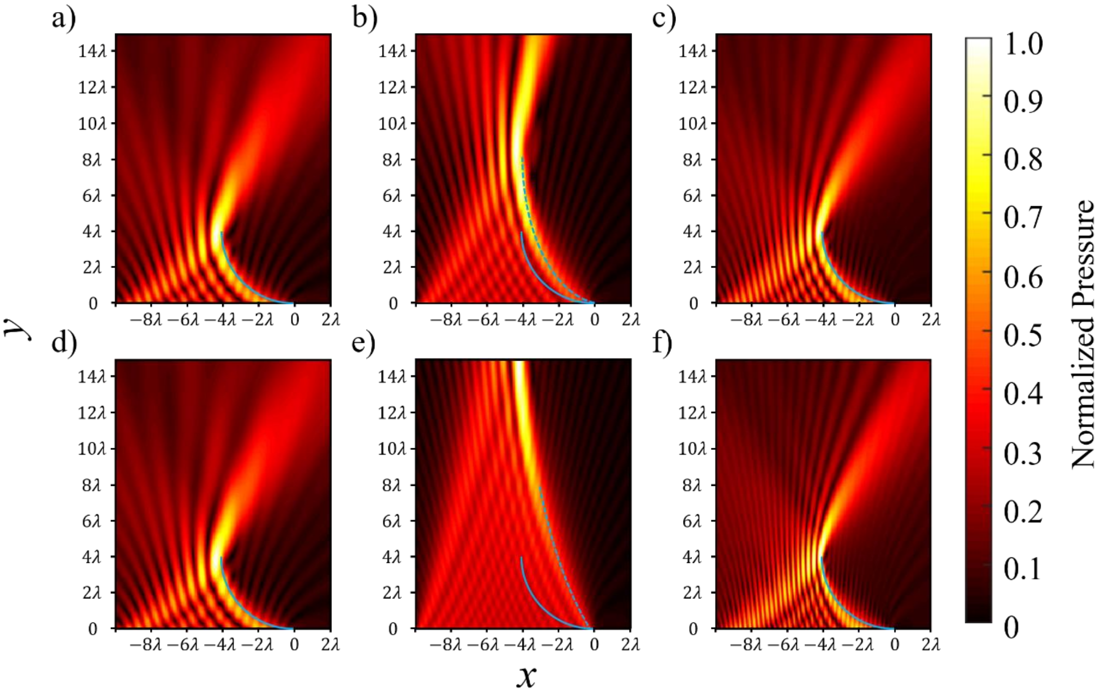

Figure 4.6: Correcting self-bending beams that propagate in highly anisotropic media. (a) Simulation results of a self-bending acoustic beam in a two-dimensional isotropic medium that matches the desired beam pattern. (b) Simulation results of a self-bending acoustic beam in a medium with an effective density two times greater in the x axis than the y axis. Here, we use the same phase profile as the previous isotropic case with a beam path shifted drastically from the desired interference pattern. (c) Simulation results of a self-bending acoustic beam in an effective two-dimensional anisotropic medium with a corrected phase profile. Here, the beam interference pattern matches the desired curve in the isotropic case. (d) Simulation results of a self-bending acoustic beam in a two-dimensional isotropic medium that follows the desired beam path. (e) Simulation results of a self-bending acoustic beam in a medium with an effective density four times greater in the x axis than the y axis. Here, we use the same phase profile as the previous isotropic case with a beam path shifted drastically from the desired interference pattern. (f) Simulation results of a self-bending acoustic beam in an effective two-dimensional anisotropic medium with a corrected phase profile. Here, the beam interference pattern matches the desired curve in the isotropic case.

interference pattern (Fig. 4.6d). For the aforementioned anisotropic medium with an effective density 4 times greater in the *x* than *y*, using the same phase gradient results in an extremely distorted intensity profile with an elliptical trajectory illustrated by the dashed blue arc in Fig. 4.6e. After considering the anisotropy of the medium, we calculate the corrected phase gradient with Equation 4.26 to restore the original interference pattern.

Applying the corrected phase gradient restores the circular interference pattern as illustrated by Fig. 4.6f. These numerical examples demonstrate the robustness of our transformation acoustics based correction technique to restore the distorted intensity profiles of self-bending acoustic beams in anisotropic media.

4.5.2 Grating dispersion

The one-dimensional dispersion relation with a dependency on grating fin height allows us to design an effective anisotropic medium using two different fin heights in the *x* and *y* directions. The one-dimensional dispersion relation is given by [142],

$$k = k_0\sqrt{1 + \frac{w^2}{p^2}\tan^2(k_0 T)}\,, \tag{S.25}$$

where k is the spoof surface acoustic wave (SSAW) wavenumber, w is the spacing between grating fins, p is the grating periodicity, and T is the grating fin height. To illustrate how the fin height impacts the surface wave propagation, we keep the grating parameters w and p to be constant, at 4.76 mm and 6.35 mm respectively. We plot the dispersion curves of these one-dimensional gratings with a 4 mm fin height and a 6.2 mm fin heights in Fig. 4.7a. The subsequent results are compared to the linear dispersion relation of air at audible frequencies (Fig. 4.7a). As illustrated in the plot, the difference in the SSAW wavenumbers for the two fin heights increases with frequency. This wavenumber discrepancy has a direct impact on the SSAW wavelength and effective sound speed across the grating. From relations of linear acoustics, we can equate any discrepancy in the sound speed or wavelength to a difference in the effective density of the gratings with $c_x = c/\sqrt{r_\rho}$ (where c and c_x are the sound speeds in the isotropic medium and along the *x’* axis in the

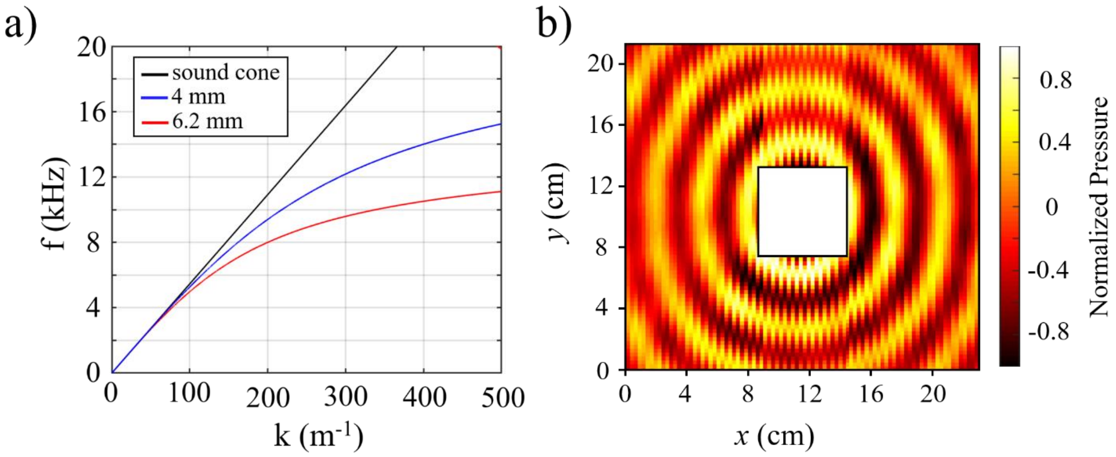

Figure 4.7: Selected grating dispersion with experimental validation. (a) Dispersion curves of SSAWs propagating across grating structures with a 4 mm fin height (blue) and 6.2 mm fin height (red) compared to the dispersion relation of air at audible frequencies (black). (b) Measured pressure field of an acoustic point source positioned directly on top of an effective two-dimensional anisotropic surface.

anisotropic medium, respectively). For a selected frequency of 9 kHz, we calculate the effective grating density with the dispersion relation in Fig. 4.7a to be 1.84 times larger when a source is propagating perpendicular to the 6.2 mm fins compared to the 4 mm fins. Therefore, if we design a two-dimensional grating with a 4 mm fin height perpendicular to the *y* axis and 6.2 mm fin height perpendicular to the *x* axis, we have an effective anisotropic surface with a density 1.84 times larger in the *x* than *y*. However, upon fabrication of the design, we place a single point source directly above the grating and output a 9 kHz acoustic wave to measure the resulted pressure field and observe an effective density ratio of 1.35 (Fig. 4.7b). While there seems to be a rather large discrepancy in the theoretical and experimental effective density ratio, a more accurate comparison of results is through the direct measurement of the effective wavelength. Using the dispersion relation and the selected grating fin heights, we calculate an effective wavelength ratio 1.35 times larger in *y* than *x* at 9 kHz and measure an average effective wavelength ratio of 1.16. Here, the difference in the theory and experiment is 14.0%, which

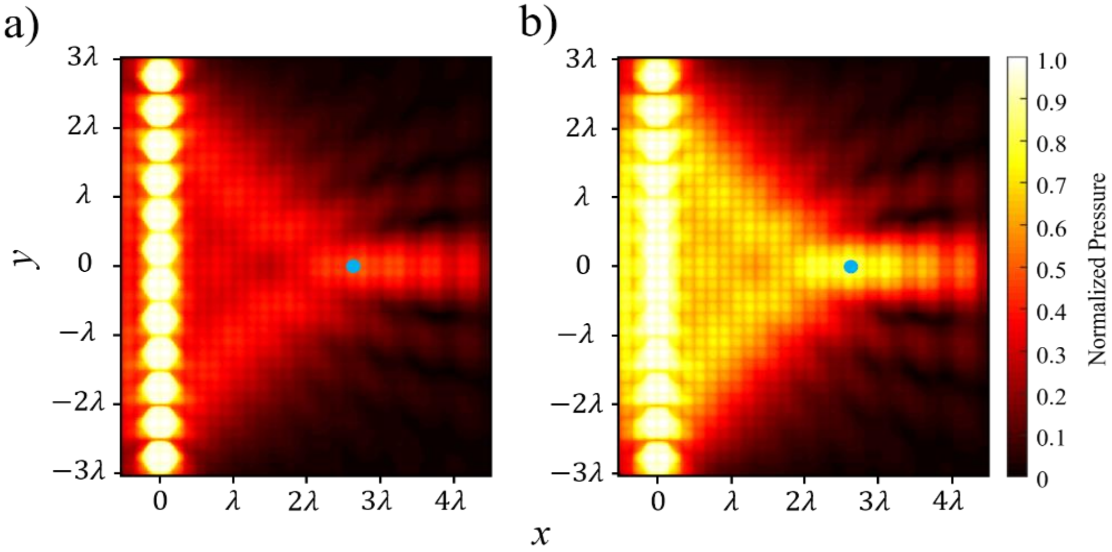

Figure 4.8: Simulations that consider viscothermal loss. (a) Full-wave simulation considering viscothermal loss results of a focused acoustic beam in a two-dimensional isotropic medium that focuses 100 mm to the right of the center of the transducer array. (b) Full-wave simulation of a of a focused acoustic beam across a lossless two-dimensional isotropic grating focusing 100 mm to the right of the center of the transducer array.

is a reasonable experimental error. For this transformation acoustics-based correction method, we use the experimentally determined density ratio of 1.35 in Sections 4.2 and 4.3 and find good agreement between the theory and experiment.

4.5.3 Full-wave simulations with and without viscothermal loss

We study how the viscothermal loss of the two-dimensional grating structures impacts the beamforming capabilities of SSAWs across the grating surface. For certain grating designs that support surface acoustic waves, viscothermal losses have a significant impact on the acoustic energy propagation across the surface [142]. To see if any unwanted lossy effects occur on our grating design, we perform full-wave simulations of a focused acoustic beam with a focal point 100 mm to the right of the center of the transducer array and evaluate its focusing performance. When considering the viscothermal loss of the

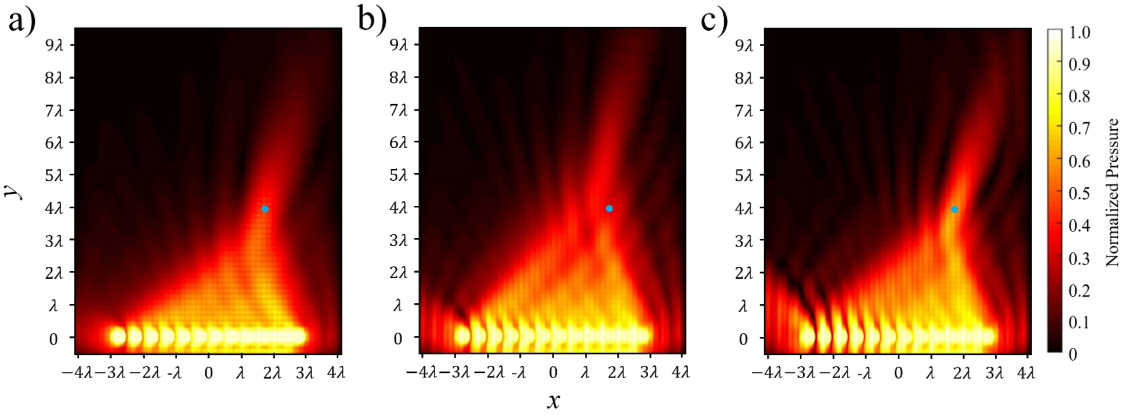

Figure 4.9: Simulation of an arbitrarily focused acoustic beam. (a) Full-wave simulation results of a focused acoustic beam in a two-dimensional isotropic medium that focuses 70 mm to the right and 150 mm above the center of the transducer array. (b) Full-wave simulation results of a focused acoustic beam in an effective two-dimensional anisotropic medium with the same phase profile as (a). Here, the resulted focal point shifts from the desired location due to the anisotropic effects of the medium. (c) Full-wave simulation results of a focused acoustic beam in an effective two-dimensional anisotropic medium with a corrected phase profile. Here, the focal point matches the desired focal point in (a).

grating, we note a rather large reduction in the acoustic intensity that propagates across the grating surface. However, the resulted focusing matches the desired focal point denoted by the blue dot in Fig. 4.8a without any apparent energy loss as the beamformed wave propagates across the grating surface. Without considering the viscothermal loss of the grating, the same focal point is achieved with a noticeably higher acoustic intensity (Fig. 4.8b). These results demonstrate that the viscothermal loss of the grating primarily impacts the acoustic energy coupling to the grating without altering the location of the focal point. Therefore, the viscothermal loss from our grating design does not impact the beamforming of the acoustic signal for the purposes of our study. In addition to the numerical simulations provided in the previous sections, we performed full-wave simulations of the focused and self-bending beams to further verify our transformation acoustics-based correction method.

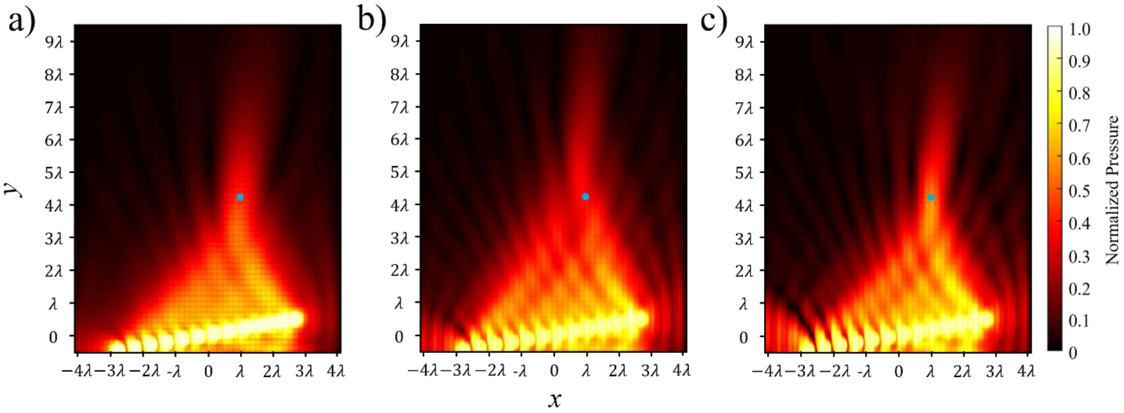

Figure 4.10: Simulation of an arbitrarily focused acoustic beam with a tilted source. (a) Full-wave simulation results of a focused acoustic beam in a two-dimensional isotropic medium that achieves the desired focal point with a ten-degree tilt. (b) Full-wave simulation results of a focused acoustic beam in an effective two-dimensional anisotropic medium with the same phase profile and tilt as the previous isotropic case. Here, the focal point of the phase profile shifts from the desired location that the isotropic case achieves. (c) Full-wave simulation results of a focused acoustic beam in an effective two-dimensional anisotropic medium with a corrected phase profile. Here, the focal point matches the desired focal point in the isotropic case.

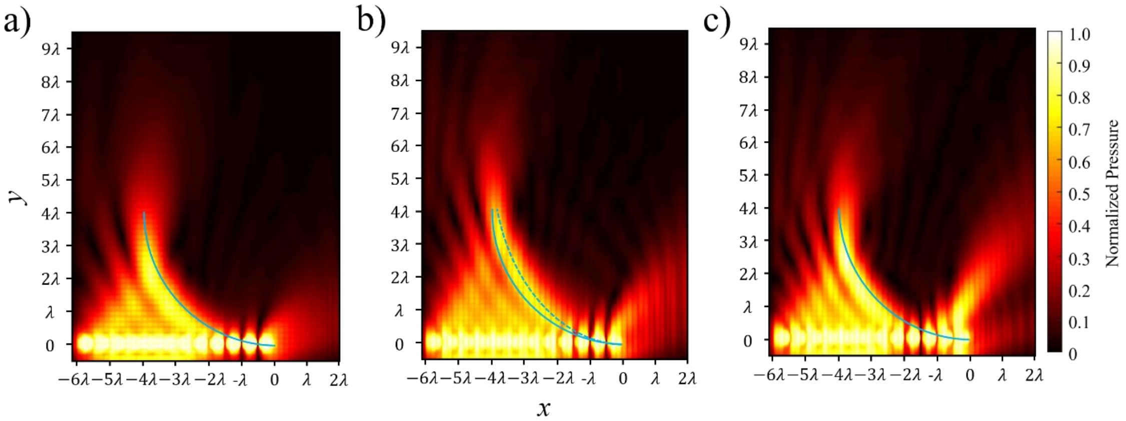

Figure 4.11: Simulation of a self-bending acoustic beam. (a) Full-wave simulation results of a self-bending acoustic beam in a two-dimensional isotropic medium that matches the desired beam pattern. (b) Full-wave simulation results of a self-bending acoustic beam in an effective two-dimensional anisotropic medium with the same phase profile as the previous isotropic case. Here, the interference pattern resulted from the phase profile shifts from the desired curve. (c) Simulation results of a self-bending acoustic beam in an effective two-dimensional anisotropic medium with a corrected phase profile. Here, the beam interference pattern matches the desired curve in the isotropic case.

CHAPTER 5

CONCLUSIONS

5.1 Non-Hermitian complementary acoustic metamaterials

In conclusion, we have obtained the values of the material parameters needed for the NHCMM to compensate a lossy skull barrier. The density and sound speed of the NHCMM are the direct opposite of those of the skull, which suppress the impedance mismatch of the skull barrier. The opposite imaginary parts of the material parameters indicate the use of an active gain element which compensates for the energy loss through the skull. The ultrasonic imaging of a brain tumor and the focusing through the complemented skull demonstrate an effective performance of the NHCMM. This NHCMM sets the foundation for noninvasive ultrasonic brain imaging and neuron disease treatments that require high frequency ultrasound. Additionally, we evaluated the performance of NHCMMs for imaging through the skull with near realistic conditions by modeling cases where the skull exhibited curving, sloping, and interior surface aberrations. In all cases, the acoustic pressure field revealed the presence of a tumor when NHCMMs with material parameters calibrated to each unique skull condition were applied to the skull surfaces, as determined by both qualitative observations as well as calculating the contrast to noise ratio of the pressure signal. In contrast, ultrasound imaging through the skull with no NHCMM present or with an improperly designed NHCMM, one that was not tailored to match the skull profile, failed to resolve the tumor regardless of the skull shape. Thus, tunable NHCMMs are shown to be a functional and novel tool for diagnostic ultrasound imaging and can be applied to detect tumor presence for any skull geometry.

Our future work aims to use a NHCMM comprised of active feedback loop circuits embedded in hydrogel to improve the acoustic transmission through a human skull sample in an experiment. This procedure begins with determining the density and sound speed of a human skull sample by measuring its acoustic reflection and transmission in a transmission line. The transmission line is comprised of a collimated ultrasound transducer and two calibrated needle hydrophones on both sides of the skull that send and receive ultrasound pulses, respectively. The collimated transducer sends an acoustic pulse towards the skull and the hydrophones to record the resulting reflection and transmission. The reflection and transmission coefficients are used to calculate the material properties of the skull with the parameter retrieval method in [56]. We can compare these experimental results with the reflection and transmission coefficients in the previous finite element simulations. Once the skull parameters are calculated, we finalize the unit cell design and determine the efficiency terms of the sending and sensing piezo elements within the metamaterial.

With the passive reflection and transmission coefficients and the efficiency terms, we calculate the gain values that realize the negative effective properties of the skull. However, due to potential errors in the experiment, we do not necessarily expect the calculated gain values to realize the exact negative effective density and bulk modulus of the skull. Instead, we optimize the NHCMM performance by varying the phase and amplitudes of G_1 and G_2 near their calculated values to maximize the acoustic transmission and minimize the acoustic reflection. While this one-dimensional experimental proof of concept is an achievement on its own, a two-dimensional unit cell array must be fabricated to realize non-invasive imaging through the skull. This array requires microfabrication to achieve a reasonable imaging resolution, as the final resolution depends on the size of the metamaterial unit cell. Transitioning this work from a one-dimensional proof of concept to a functioning two-dimensional material requires several non-trivial steps and additional considerations not discussed in this work. These considerations include overheating the skull, powering multiple unit cells simultaneously, independently controlling the active metamaterial outputs of each unit cell, designing a reliable microfabrication technique, and other unforeseen complications that occur during experiments. While the final goal of this work may be difficult to achieve, the ultimate outcome would have a significant impact on the biomedical community, as a multitude of potential applications could stem from this metamaterials-based approach to transmit ultrasound energy through the skull.

5.2 Willis coupling

In conclusion, we demonstrate a systematic approach to realize an arbitrarily given bianisotropic polarizability by a designed acoustic grating. This is achieved by optimizing the geometry of the grating element to realize maximum scattering efficiency and confirming the asymmetric wave scattering of the desired bianisotropic properties in the reciprocal space through spatial Fourier analysis. The resulted parity symmetry violation of the acoustic wave propagation indicates the necessity of inversion symmetry breaking for the realization of the bianisotropic properties. The experimentally measured acoustic wave interactions with the designed bianisotropic grating match the desired scattering patterns of the given polarizability tensor. Our method paves the road for systematic realization of bianisotropic properties and asymmetric wave propagation with unitary efficiency, which is important for one-way acoustic filtering, sensing, and lensing.

The active metamaterial with Willis coupling dramatically increases the accessible range of the effective density and bulk modulus by at least two orders of magnitude as compared to the accessibility of their non-Willis counterpart. In the most extreme cases, the complex effective density and bulk modulus for active metamaterials with Willis coupling extend the parameter range beyond the non-Willis case by three orders of magnitude. Similar range expansion is observed in the complex acoustic impedance. The parameter range expansion is dominated by the imaginary part of the asymmetry coefficient of the Willis coupling. The development of active metamaterials with extreme material parameters via Willis coupling will enable improved control over acoustic propagation and will yield valuable advancements in biomedical imaging, noise control, and invisibility cloaking technology.

5.3 Transformation Acoustics

We use transformation acoustics to modify phase profiles for arbitrarily focused and self-bending acoustic beams to correct for the distortive effects resulted from anisotropy. Experimental verifications are performed using two-dimensional grating structures that support SSAWs with density anisotropy in the *x* and *y* directions. This transformation acoustics enabled beamforming is crucial for biomedical ultrasound applications, such as HIFU, acoustic tweezers for non-invasive surgeries, cell trapping, and cell sorting.

REFERENCES

[1] F. Zangeneh-Nejad and R. Fleury, "Active times for acoustic metamaterials", *Reviews in Physics* **4**, 100031 (2019).

[2] S. A. Cummer, J. Christensen, and A. Alù, "Controlling sound with acoustic metamaterials", *Nature Reviews Materials* **1** (3), 1 (2016).

[3] G. Ma and P. Sheng, "Acoustic metamaterials: From local resonances to broad horizons", *Science advances* **2** (2), e1501595 (2016).

[4] Z. Liu, X. Zhang, Y. Mao, Y. Zhu, Z. Yang, C. T. Chan, and P. Sheng, "Locally resonant sonic materials", *science* **289** (5485), 1734 (2000).

[5] N. Fang, D. Xi, J. Xu, M. Ambati, W. Srituravanich, C. Sun, and X. Zhang, "Ultrasonic metamaterials with negative modulus", *Nature materials* **5** (6), 452 (2006).

[6] S. H. Lee, C. M. Park, Y. M. Seo, Z. G. Wang, and C. K. Kim, "Composite acoustic medium with simultaneously negative density and modulus", *Physical review letters* **104** (5), 054301 (2010).

[7] J. Zhu, J. Christensen, J. Jung, L. Martin-Moreno, X. Yin, L. Fok, X. Zhang, and F. Garcia-Vidal, "A holey-structured metamaterial for acoustic deep-subwavelength imaging", *Nature physics* **7** (1), 52 (2011).

[8] F. Lemoult, M. Fink, and G. Lerosey, "Acoustic resonators for far-field control of sound on a subwavelength scale", *Physical review letters* **107** (6), 064301 (2011).

[9] J. Li, L. Fok, X. Yin, G. Bartal, and X. Zhang, "Experimental demonstration of an acoustic magnifying hyperlens", *Nature materials* **8** (12), 931 (2009).

[10] T. Brunet, A. Merlin, B. Mascaro, K. Zimny, J. Leng, O. Poncelet, C. Aristégui, and O. Mondain-Monval, "Soft 3D acoustic metamaterial with negative index", *Nature materials* **14** (4), 384 (2015).

[11] R. Fleury, D. Sounas, and A. Alù, "An invisible acoustic sensor based on parity-time symmetry", *Nature communications* **6** (1), 1 (2015).

[12] S. Chen, Y. Fan, Q. Fu, H. Wu, Y. Jin, J. Zheng, and F. Zhang, "A review of tunable acoustic metamaterials", *Applied Sciences* **8** (9), 1480 (2018).

[13] B.-I. Popa, D. Shinde, A. Konneker, and S. A. Cummer, "Active acoustic metamaterials reconfigurable in real time", *Physical Review B* **91** (22), 220303 (2015).

[14] W. Akl and A. Baz, "Experimental characterization of active acoustic metamaterial cell with controllable dynamic density", *Journal of Applied Physics* **112** (8), 084912 (2012).

[15] L.-Y. Zheng, Y. Wu, X. Ni, Z.-G. Chen, M.-H. Lu, and Y.-F. Chen, "Acoustic cloaking by a near-zero-index phononic crystal", *Applied Physics Letters* **104** (16), 161904 (2014).

[16] L. Ning, Y.-Z. Wang, and Y.-S. Wang, "Active control of a black hole or concentrator for flexural waves in an elastic metamaterial plate", *Mechanics of Materials* **142**, 103300 (2020).

[17] G.-H. Li, T.-X. Ma, Y.-Z. Wang, and Y.-S. Wang, "Active control on topological immunity of elastic wave metamaterials", *Scientific reports* **10** (1), 1 (2020).

[18] B.-I. Popa, L. Zigoneanu, and S. A. Cummer, "Tunable active acoustic metamaterials", *Physical Review B* **88** (2), 024303 (2013).

[19] C. Cho, X. Wen, N. Park, and J. Li, "Digitally virtualized atoms for acoustic metamaterials", *Nature communications* **11** (1), 1 (2020).

[20] S. R. Craig, P. J. Welch, and C. Shi, "Non-Hermitian complementary acoustic metamaterials for lossy barriers", *Applied Physics Letters* **115** (5), 051903 (2019).

[21] S. R. Craig, P. J. Welch, and C. Shi, "Non-Hermitian Complementary Acoustic Metamaterials for Imaging Through Skull With Imperfections", *Frontiers in Mechanical Engineering* **6**, 55 (2020).

[22] J. T. Bushberg and J. M. Boone, *The essential physics of medical imaging*. (Lippincott Williams & Wilkins, 2011).

[23] A. Fenster, D. B. Downey, and H. N. Cardinal, "Three-dimensional ultrasound imaging", *Physics in medicine & biology* **46** (5), R67 (2001).

[24] J. E. Kennedy, G. Ter Haar, and D. Cranston, "High intensity focused ultrasound: surgery of the future?", *The British journal of radiology* **76** (909), 590 (2003).

[25] J. Kennedy, F. Wu, G. Ter Haar, F. Gleeson, R. Phillips, M. Middleton, and D. Cranston, "High-intensity focused ultrasound for the treatment of liver tumours", *Ultrasonics* **42** (1-9), 931 (2004).

[26] J. E. Kennedy, "High-intensity focused ultrasound in the treatment of solid tumours", *Nature reviews cancer* **5** (4), 321 (2005).

[27] F. Wu, Z.-B. Wang, W.-Z. Chen, J. Bai, H. Zhu, and T.-Y. Qiao, "Preliminary experience using high intensity focused ultrasound for the treatment of patients with advanced stage renal malignancy", *The Journal of urology* **170** (6), 2237 (2003).

[28] F. Wu, Z.-B. Wang, W.-Z. Chen, J.-Z. Zou, J. Bai, H. Zhu, K.-Q. Li, F.-L. Xie, C.-B. Jin, and H.-B. Su, "Extracorporeal focused ultrasound surgery for treatment of human solid carcinomas: early Chinese clinical experience", *Ultrasound in medicine & biology* **30** (2), 245 (2004).

[29] J. Ninet, X. Roques, R. Seitelberger, C. Deville, J. L. Pomar, J. Robin, O. Jegaden, F. Wellens, E. Wolner, and C. Vedrinne, "Surgical ablation of atrial fibrillation with off-pump, epicardial, high-intensity focused ultrasound: results of a multicenter trial", *The Journal of thoracic and cardiovascular surgery* **130** (3), 803. e1 (2005).

[30] O. A. Sapozhnikov, A. D. Maxwell, B. MacConaghy, and M. R. Bailey, "A mechanistic analysis of stone fracture in lithotripsy", *The Journal of the Acoustical Society of America* **121** (2), 1190 (2007).

[31] A. Neisius, N. B. Smith, G. Sankin, N. J. Kuntz, J. F. Madden, D. E. Fovargue, S. Mitran, M. E. Lipkin, W. N. Simmons, and G. M. Preminger, "Improving the lens design and performance of a contemporary electromagnetic shock wave lithotripter", *Proceedings of the National Academy of Sciences* **111** (13), E1167 (2014).

[32] M. Kinoshita, N. McDannold, F. A. Jolesz, and K. Hynynen, "Noninvasive localized delivery of Herceptin to the mouse brain by MRI-guided focused ultrasound-induced blood–brain barrier disruption", *Proceedings of the National Academy of Sciences* **103** (31), 11719 (2006).

[33] T. Nishida, H. Shimokawa, K. Oi, H. Tatewaki, T. Uwatoku, K. Abe, Y. Matsumoto, N. Kajihara, M. Eto, and T. Matsuda, "Extracorporeal cardiac shock

wave therapy markedly ameliorates ischemia-induced myocardial dysfunction in pigs in vivo", *Circulation* **110** (19), 3055 (2004).

[34] Y. Takakuwa, M. Sarai, H. Kawai, A. Yamada, K. Shiino, K. Takada, Y. Nagahara, M. Miyagi, S. Motoyama, and H. Toyama, "Extracorporeal shock wave therapy for coronary artery disease: relationship of symptom amelioration and ischemia improvement", *Asia Oceania Journal of Nuclear Medicine and Biology* **6** (1), 1 (2018).

[35] J. D. Heckman, J. Mccabe, and J. J. Rni, "By non-invasive, low-intensity pulsed ultrasound", *J Bone Joint Surg Am* **76**, 26 (1994).

[36] M. Hadjiargyrou, K. McLeod, J. P. Ryaby, and C. Rubin, "Enhancement of fracture healing by low intensity ultrasound", *Clinical Orthopaedics and Related Research®* **355**, S216 (1998).

[37] J. W. Busse, M. Bhandari, A. V. Kulkarni, and E. Tunks, "The effect of low-intensity pulsed ultrasound therapy on time to fracture healing: a meta-analysis", *Cmaj* **166** (4), 437 (2002).

[38] H. J. Kim, J. F. Greenleaf, R. R. Kinnick, J. T. Bronk, and M. E. Bolander, "Ultrasound-mediated transfection of mammalian cells", *Human gene therapy* **7** (11), 1339 (1996).

[39] M. D. Bednarski, J. W. Lee, M. R. Callstrom, and K. Li, "In vivo target-specific delivery of macromolecular agents with MR-guided focused ultrasound", *Radiology* **204** (1), 263 (1997).

[40] B. C. Tran, J. Seo, T. L. Hall, J. B. Fowlkes, and C. A. Cain, "Microbubble-enhanced cavitation for noninvasive ultrasound surgery", *IEEE transactions on ultrasonics, ferroelectrics, and frequency control* **50** (10), 1296 (2003).

[41] K. Hynynen, W. R. Freund, H. E. Cline, A. H. Chung, R. D. Watkins, J. P. Vetro, and F. A. Jolesz, "A clinical, noninvasive, MR imaging-monitored ultrasound surgery method", *Radiographics* **16** (1), 185 (1996).

[42] S. Wang, J. Lin, T. Wang, X. Chen, and P. Huang, "Recent advances in photoacoustic imaging for deep-tissue biomedical applications", *Theranostics* **6** (13), 2394 (2016).

[43] C. Errico, J. Pierre, S. Pezet, Y. Desailly, Z. Lenkei, O. Couture, and M. Tanter, "Ultrafast ultrasound localization microscopy for deep super-resolution vascular imaging", *Nature* **527** (7579), 499 (2015).

[44] M. Tanter and M. Fink, "Ultrafast imaging in biomedical ultrasound", *IEEE transactions on ultrasonics, ferroelectrics, and frequency control* **61** (1), 102 (2014).

[45] F. Yan, Y. Sun, Y. Mao, M. Wu, Z. Deng, S. Li, X. Liu, L. Xue, and H. Zheng, "Ultrasound molecular imaging of atherosclerosis for early diagnosis and therapeutic evaluation through leucocyte-like multiple targeted microbubbles", *Theranostics* **8** (7), 1879 (2018).

[46] M. M. Monti, C. Schnakers, A. S. Korb, A. Bystritsky, and P. M. Vespa, "Non-invasive ultrasonic thalamic stimulation in disorders of consciousness after severe brain injury: a first-in-man report", *Brain Stimul* **9** (6), 940 (2016).

[47] F. J. Fry and J. E. Barger, "Acoustical properties of the human skull", *The Journal of the Acoustical Society of America* **63** (5), 1576 (1978).

[48] S. Pichardo, V. W. Sin, and K. Hynynen, "Multi-frequency characterization of the speed of sound and attenuation coefficient for longitudinal transmission of freshly excised human skulls", *Physics in medicine & biology* **56** (1), 219 (2010).

[49] C. Shen, J. Xu, N. X. Fang, and Y. Jing, "Anisotropic complementary acoustic metamaterial for canceling out aberrating layers", *Physical Review X* **4** (4), 041033 (2014).

[50] C. Shi, M. Dubois, Y. Chen, L. Cheng, H. Ramezani, Y. Wang, and X. Zhang, "Accessing the exceptional points of parity-time symmetric acoustics", *Nature communications* **7** (1), 1 (2016).

[51] B.-I. Popa and S. A. Cummer, "Non-reciprocal and highly nonlinear active acoustic metamaterials", *Nature communications* **5** (1), 1 (2014).

[52] X. Zhu, H. Ramezani, C. Shi, J. Zhu, and X. Zhang, "P t-symmetric acoustics", *Physical Review X* **4** (3), 031042 (2014).

[53] H. Ramezani, M. Dubois, Y. Wang, Y. R. Shen, and X. Zhang, "Directional excitation without breaking reciprocity", *New Journal of Physics* **18** (9), 095001 (2016).

[54] Y. Aurégan and V. Pagneux, "P T-symmetric scattering in flow duct acoustics", *Physical review letters* **118** (17), 174301 (2017).

[55] T. Liu, X. Zhu, F. Chen, S. Liang, and J. Zhu, "Unidirectional wave vector manipulation in two-dimensional space with an all passive acoustic parity-time-

symmetric metamaterials crystal", *Physical review letters* **120** (12), 124502 (2018).

[56] V. Fokin, M. Ambati, C. Sun, and X. Zhang, "Method for retrieving effective properties of locally resonant acoustic metamaterials", *Physical Review B* **76** (14), 144302 (2007).

[57] N. Engheta, "Pursuing near-zero response", *science* **340** (6130), 286 (2013).

[58] M. Dubois, C. Shi, X. Zhu, Y. Wang, and X. Zhang, "Observation of acoustic Dirac-like cone and double zero refractive index", *Nature communications* **8** (1), 1 (2017).

[59] W. J. Elias, D. Huss, T. Voss, J. Loomba, M. Khaled, E. Zadicario, R. C. Frysinger, S. A. Sperling, S. Wylie, and S. J. Monteith, "A pilot study of focused ultrasound thalamotomy for essential tremor", *New England Journal of Medicine* **369** (7), 640 (2013).

[60] A. D. Maxwell, G. Owens, H. S. Gurm, K. Ives, D. D. Myers Jr, and Z. Xu, "Noninvasive treatment of deep venous thrombosis using pulsed ultrasound cavitation therapy (histotripsy) in a porcine model", *Journal of vascular and interventional radiology* **22** (3), 369 (2011).

[61] K. ll Lee, E. Hughes, V. Humphrey, T. Leighton, and M. J. Choi, "Empirical angle-dependent Biot and MBA models for acoustic anisotropy in cancellous bone", *Physics in medicine & biology* **52** (1), 59 (2006).

[62] T. H. Smit, J. M. Huyghe, and S. C. Cowin, "Estimation of the poroelastic parameters of cortical bone", *Journal of biomechanics* **35** (6), 829 (2002).

[63] A. Geissler, A. Gartus, T. Foki, A. R. Tahamtan, R. Beisteiner, and M. Barth, "Contrast-to-noise ratio (CNR) as a quality parameter in fMRI", *Journal of Magnetic Resonance Imaging: An Official Journal of the International Society for Magnetic Resonance in Medicine* **25** (6), 1263 (2007).

[64] J. J. Dahl, D. Hyun, M. Lediju, and G. E. Trahey, "Lesion detectability in diagnostic ultrasound with short-lag spatial coherence imaging", *Ultrasonic imaging* **33** (2), 119 (2011).

[65] Y. Deng, M. L. Palmeri, N. C. Rouze, G. E. Trahey, C. M. Haystead, and K. R. Nightingale, "Quantifying image quality improvement using elevated acoustic output in B-mode harmonic imaging", *Ultrasound in medicine & biology* **43** (10), 2416 (2017).

[66] M.-H. Lu, X.-K. Liu, L. Feng, J. Li, C.-P. Huang, Y.-F. Chen, Y.-Y. Zhu, S.-N. Zhu, and N.-B. Ming, "Extraordinary acoustic transmission through a 1D grating with very narrow apertures", *Physical review letters* **99** (17), 174301 (2007).

[67] A. Al-Refai, "Blood vessels that groove the skull", *Anat. Physiol. Curr. Res* **6**, 1000195 (2016).

[68] E. Epstein, A. Testa, A. Gaurilcikas, A. Di Legge, L. Ameye, V. Atstupenaite, A. L. Valentini, B. Gui, N.-O. Wallengren, and S. Pudaric, "Early-stage cervical cancer: tumor delineation by magnetic resonance imaging and ultrasound—a European multicenter trial", *Gynecologic oncology* **128** (3), 449 (2013).

[69] W. K. Moon, Y.-W. Shen, M. S. Bae, C.-S. Huang, J.-H. Chen, and R.-F. Chang, "Computer-aided tumor detection based on multi-scale blob detection algorithm

in automated breast ultrasound images", *IEEE transactions on medical imaging* **32** (7), 1191 (2012).

[70] T. L. Szabo, *Diagnostic ultrasound imaging: inside out*. (Academic press, 2004).

[71] M. F. Dempsey, B. R. Condon, and D. M. Hadley, "Measurement of tumor “size” in recurrent malignant glioma: 1D, 2D, or 3D?", *American journal of neuroradiology* **26** (4), 770 (2005).

[72] K. Chopra, D. Calva, M. Sosin, K. K. Tadisina, A. Banda, C. De La Cruz, M. R. Chaudhry, T. Legesse, C. B. Drachenberg, and P. N. Manson, "A comprehensive examination of topographic thickness of skin in the human face", *Aesthetic surgery journal* **35** (8), 1007 (2015).

[73] A. Moreira-Gonzalez, F. E. Papay, and J. E. Zins, "Calvarial thickness and its relation to cranial bone harvest", *Plastic and reconstructive surgery* **117** (6), 1964 (2006).

[74] S. R. Craig, X. Su, A. Norris, and C. Shi, "Experimental realization of acoustic bianisotropic gratings", *Physical Review Applied* **11** (6), 061002 (2019).

[75] S. R. Craig, B. Wang, X. Su, D. Banerjee, P. J. Welch, M. C. Yip, Y. Hu, and C. Shi, "Extreme material parameters accessible by active acoustic metamaterials with Willis coupling", *The Journal of the Acoustical Society of America* **151** (3), 1722 (2022).

[76] N. Gao, Z. Zhang, J. Deng, X. Guo, B. Cheng, and H. Hou, "Acoustic metamaterials for noise reduction: a review", *Advanced Materials Technologies*, 2100698 (2022).

[77] S. J. Elliott and P. A. Nelson, "Active noise control", *IEEE signal processing magazine* **10** (4), 12 (1993).

[78] R.-Q. Li, B. Liang, Y. Li, W.-W. Kan, X.-Y. Zou, and J.-C. Cheng, "Broadband asymmetric acoustic transmission in a gradient-index structure", *Applied Physics Letters* **101** (26), 263502 (2012).

[79] H.-x. Sun, S.-q. Yuan, and S.-y. Zhang, "Asymmetric acoustic transmission in multiple frequency bands", *Applied Physics Letters* **107** (21), 213505 (2015).

[80] B. Liang, X. Guo, J. Tu, D. Zhang, and J. Cheng, "An acoustic rectifier", *Nature materials* **9** (12), 989 (2010).

[81] R. Fleury, D. L. Sounas, C. F. Sieck, M. R. Haberman, and A. Alù, "Sound isolation and giant linear nonreciprocity in a compact acoustic circulator", *science* **343** (6170), 516 (2014).

[82] D. L. Sounas, C. Caloz, and A. Alu, "Giant non-reciprocity at the subwavelength scale using angular momentum-biased metamaterials", *Nature communications* **4** (1), 1 (2013).

[83] Z. Yang, F. Gao, X. Shi, X. Lin, Z. Gao, Y. Chong, and B. Zhang, "Topological acoustics", *Physical review letters* **114** (11), 114301 (2015).

[84] R. Fleury, A. B. Khanikaev, and A. Alu, "Floquet topological insulators for sound", *Nature communications* **7** (1), 1 (2016).

[85] C. He, X. Ni, H. Ge, X.-C. Sun, Y.-B. Chen, M.-H. Lu, X.-P. Liu, and Y.-F. Chen, "Acoustic topological insulator and robust one-way sound transport", *Nature physics* **12** (12), 1124 (2016).

[86] J. Lu, C. Qiu, L. Ye, X. Fan, M. Ke, F. Zhang, and Z. Liu, "Observation of topological valley transport of sound in sonic crystals", *Nature physics* **13** (4), 369 (2017).

[87] Z. Zhang, Q. Wei, Y. Cheng, T. Zhang, D. Wu, and X. Liu, "Topological creation of acoustic pseudospin multipoles in a flow-free symmetry-broken metamaterial lattice", *Physical review letters* **118** (8), 084303 (2017).

[88] M. Xiao, W.-J. Chen, W.-Y. He, and C. T. Chan, "Synthetic gauge flux and Weyl points in acoustic systems", *Nature physics* **11** (11), 920 (2015).

[89] J. Noh, S. Huang, D. Leykam, Y. D. Chong, K. P. Chen, and M. C. Rechtsman, "Experimental observation of optical Weyl points and Fermi arc-like surface states", *Nature physics* **13** (6), 611 (2017).

[90] F. Li, X. Huang, J. Lu, J. Ma, and Z. Liu, "Weyl points and Fermi arcs in a chiral phononic crystal", *Nature physics* **14** (1), 30 (2018).

[91] W. Zhu, X. Fang, D. Li, Y. Sun, Y. Li, Y. Jing, and H. Chen, "Simultaneous observation of a topological edge state and exceptional point in an open and non-Hermitian acoustic system", *Physical review letters* **121** (12), 124501 (2018).

[92] G. Castaldi, S. Savoia, V. Galdi, A. Alu, and N. Engheta, "P T metamaterials via complex-coordinate transformation optics", *Physical review letters* **110** (17), 173901 (2013).

[93] Y. Ra'di, D. L. Sounas, and A. Alù, "Metagratings: Beyond the limits of graded metasurfaces for wave front control", *Physical review letters* **119** (6), 067404 (2017).

[94] S. A. Tretyakov and A. A. Sochava, "Reflection and transmission of plane electromagnetic waves in uniaxial bianisotropic materials", *International journal of infrared and millimeter waves* **15** (5), 829 (1994).

[95] C. F. Sieck, A. Alù, and M. R. Haberman, "Origins of Willis coupling and acoustic bianisotropy in acoustic metamaterials through source-driven homogenization", *Physical Review B* **96** (10), 104303 (2017).

[96] M. B. Muhlestein, C. F. Sieck, P. S. Wilson, and M. R. Haberman, "Experimental evidence of Willis coupling in a one-dimensional effective material element", *Nature communications* **8** (1), 1 (2017).

[97] J. Li, C. Shen, A. Díaz-Rubio, S. A. Tretyakov, and S. A. Cummer, "Systematic design and experimental demonstration of bianisotropic metasurfaces for scattering-free manipulation of acoustic wavefronts", *Nature communications* **9** (1), 1 (2018).

[98] L. Quan, Y. Ra’di, D. L. Sounas, and A. Alù, "Maximum Willis coupling in acoustic scatterers", *Physical review letters* **120** (25), 254301 (2018).

[99] L. Quan, D. L. Sounas, and A. Alù, "Nonreciprocal Willis coupling in zero-index moving media", *Physical review letters* **123** (6), 064301 (2019).

[100] D. Torrent, "Acoustic anomalous reflectors based on diffraction grating engineering", *Physical Review B* **98** (6), 060101 (2018).

[101] S. Koo, C. Cho, J.-h. Jeong, and N. Park, "Acoustic omni meta-atom for decoupled access to all octants of a wave parameter space", *Nature communications* **7** (1), 1 (2016).

[102] B.-I. Popa, Y. Zhai, and H.-S. Kwon, "Broadband sound barriers with bianisotropic metasurfaces", *Nature communications* **9** (1), 1 (2018).

[103] X. Su and A. N. Norris, "Retrieval method for the bianisotropic polarizability tensor of Willis acoustic scatterers", *Physical Review B* **98** (17), 174305 (2018).

[104] G. Ma, M. Yang, S. Xiao, Z. Yang, and P. Sheng, "Acoustic metasurface with hybrid resonances", *Nature materials* **13** (9), 873 (2014).

[105] Y. Li and B. M. Assouar, "Acoustic metasurface-based perfect absorber with deep subwavelength thickness", *Applied Physics Letters* **108** (6), 063502 (2016).

[106] J. Mei, G. Ma, M. Yang, Z. Yang, W. Wen, and P. Sheng, "Dark acoustic metamaterials as super absorbers for low-frequency sound", *Nature communications* **3** (1), 1 (2012).

[107] M. Yang, S. Chen, C. Fu, and P. Sheng, "Optimal sound-absorbing structures", *Materials Horizons* **4** (4), 673 (2017).

[108] H. Chen and C. T. Chan, "Acoustic cloaking and transformation acoustics", *Journal of Physics D: Applied Physics* **43** (11), 113001 (2010).

[109] R. V. Craster and S. Guenneau, *Acoustic metamaterials: Negative refraction, imaging, lensing and cloaking*. (Springer Science & Business Media, 2012).

[110] J. Li and J. B. Pendry, "Hiding under the carpet: a new strategy for cloaking", *Physical review letters* **101** (20), 203901 (2008).

[111] B.-I. Popa, L. Zigoneanu, and S. A. Cummer, "Experimental acoustic ground cloak in air", *Physical review letters* **106** (25), 253901 (2011).

[112] M. Dubois, C. Shi, Y. Wang, and X. Zhang, "A thin and conformal metasurface for illusion acoustics of rapidly changing profiles", *Applied Physics Letters* **110** (15), 151902 (2017).

[113] J. Willis, (Springer New York, 1997).

[114] J. R. Willis, "Variational principles for dynamic problems for inhomogeneous elastic media", *Wave Motion* **3** (1), 1 (1981).

[115] J. R. Willis, "Effective constitutive relations for waves in composites and metamaterials", *Proceedings of the Royal Society A: Mathematical, Physical and Engineering Sciences* **467** (2131), 1865 (2011).

[116] G. W. Milton and J. R. Willis, "On modifications of Newton's second law and linear continuum elastodynamics", *Proceedings of the Royal Society A: Mathematical, Physical and Engineering Sciences* **463** (2079), 855 (2007).

[117] Y. Zhai, H.-S. Kwon, and B.-I. Popa, "Active Willis metamaterials for ultracompact nonreciprocal linear acoustic devices", *Physical Review B* **99** (22), 220301 (2019).

[118] Y. K. Chiang, S. Oberst, A. Melnikov, L. Quan, S. Marburg, A. Alù, and D. A. Powell, "Reconfigurable acoustic metagrating for high-efficiency anomalous reflection", *Physical Review Applied* **13** (6), 064067 (2020).

[119] J. Lau, S. T. Tang, M. Yang, and Z. Yang, "Coupled decorated membrane resonators with large Willis coupling", *Physical Review Applied* **12** (1), 014032 (2019).

[120] Y. Chen, X. Li, G. Hu, M. R. Haberman, and G. Huang, "An active mechanical Willis meta-layer with asymmetric polarizabilities", *Nature communications* **11** (1), 1 (2020).

[121] J. Schindler, A. Li, M. C. Zheng, F. M. Ellis, and T. Kottos, "Experimental study of active LRC circuits with PT symmetries", *Physical Review A* **84** (4), 040101 (2011).

[122] T. Liu, G. Ma, S. Liang, H. Gao, Z. Gu, S. An, and J. Zhu, "Single-sided acoustic beam splitting based on parity-time symmetry", *Physical Review B* **102** (1), 014306 (2020).

[123] C. Cho, X. Wen, N. Park, and J. Li, "Acoustic Willis meta-atom beyond the bounds of passivity and reciprocity", *Communications Physics* **4** (1), 1 (2021).

[124] X. Wen, X. Zhu, H. W. Wu, and J. Li, "Realizing spatiotemporal effective media for acoustic metamaterials", *Physical Review B* **104** (6), L060304 (2021).

[125] A. Merkel, V. Romero-García, J.-P. Groby, J. Li, and J. Christensen, "Unidirectional zero sonic reflection in passive PT-symmetric Willis media", *Physical Review B* **98** (20), 201102 (2018).

[126] J.-P. Groby, M. Mallejac, A. Merkel, V. Romero-García, V. Tournat, D. Torrent, and J. Li, "Analytical modeling of one-dimensional resonant asymmetric and reciprocal acoustic structures as Willis materials", *New Journal of Physics* **23** (5), 053020 (2021).

[127] S. R. Craig, J. H. Lee, and C. Shi, "Beamforming with transformation acoustics in anisotropic media", *Applied Physics Letters* **117** (1), 011907 (2020).

[128] F. Zhong, J. Li, H. Liu, and S. Zhu, "Controlling surface plasmons through covariant transformation of the spin-dependent geometric phase between curved metamaterials", *Physical review letters* **120** (24), 243901 (2018).

[129] J. B. Pendry, D. Schurig, and D. R. Smith, "Controlling electromagnetic fields", *science* **312** (5781), 1780 (2006).

[130] U. Leonhardt, "Optical conformal mapping", *science* **312** (5781), 1777 (2006).

[131] D. Schurig, J. Pendry, and D. R. Smith, "Calculation of material properties and ray tracing in transformation media", *Optics express* **14** (21), 9794 (2006).

[132] S. A. Cummer and D. Schurig, "One path to acoustic cloaking", *New Journal of Physics* **9** (3), 45 (2007).

[133] H. Chen and C. T. Chan, "Acoustic cloaking in three dimensions using acoustic metamaterials", *Applied Physics Letters* **91** (18), 183518 (2007).

[134] A. Climente, D. Torrent, and J. Sánchez-Dehesa, "Sound focusing by gradient index sonic lenses", *Applied Physics Letters* **97** (10), 104103 (2010).

[135] B.-I. Popa and S. A. Cummer, "Design and characterization of broadband acoustic composite metamaterials", *Physical Review B* **80** (17), 174303 (2009).

[136] L. Zigoneanu, B.-I. Popa, and S. A. Cummer, "Design and measurements of a broadband two-dimensional acoustic lens", *Physical Review B* **84** (2), 024305 (2011).

[137] S. Jiménez-Gambín, N. Jiménez, J. M. Benlloch, and F. Camarena, "Holograms to focus arbitrary ultrasonic fields through the skull", *Physical Review Applied* **12** (1), 014016 (2019).

[138] D. J. Collins, A. Neild, and Y. Ai, "Highly focused high-frequency travelling surface acoustic waves (SAW) for rapid single-particle sorting", *Lab on a Chip* **16** (3), 471 (2016).

[139] A. Riaud, J.-L. Thomas, M. Baudoin, and O. B. Matar, "Taming the degeneration of Bessel beams at an anisotropic-isotropic interface: Toward three-dimensional control of confined vortical waves", *Physical Review E* **92** (6), 063201 (2015).

[140] T. Liu, F. Chen, S. Liang, H. Gao, and J. Zhu, "Subwavelength sound focusing and imaging via gradient metasurface-enabled spoof surface acoustic wave modulation", *Physical Review Applied* **11** (3), 034061 (2019).

[141] H. Jia, M. Lu, X. Ni, M. Bao, and X. Li, "Spatial separation of spoof surface acoustic waves on the graded groove grating", *Journal of Applied Physics* **116** (12), 124504 (2014).

[142] J. Zhu, Y. Chen, X. Zhu, F. J. Garcia-Vidal, X. Yin, W. Zhang, and X. Zhang, "Acoustic rainbow trapping", *Scientific reports* **3** (1), 1 (2013).

[143] E. Greenfield, M. Segev, W. Walasik, and O. Raz, "Accelerating light beams along arbitrary convex trajectories", *Physical review letters* **106** (21), 213902 (2011).

[144] D.-C. Chen, X.-F. Zhu, Q. Wei, D.-J. Wu, and X.-J. Liu, "Dynamic generation and modulation of acoustic bottle-beams by metasurfaces", *Scientific reports* **8** (1), 1 (2018).

[145] S. Zhao, Y. Hu, J. Lu, X. Qiu, J. Cheng, and I. Burnett, "Delivering sound energy along an arbitrary convex trajectory", *Scientific reports* **4** (1), 1 (2014).

[146] J. Lan, X. Zhang, X. Liu, and Y. Li, "Wavefront manipulation based on transmissive acoustic metasurface with membrane-type hybrid structure", *Scientific reports* **8** (1), 1 (2018).

[147] Y. Li, X. Jiang, R.-q. Li, B. Liang, X.-y. Zou, L.-l. Yin, and J.-c. Cheng, "Experimental realization of full control of reflected waves with subwavelength acoustic metasurfaces", *Physical Review Applied* **2** (6), 064002 (2014).